Radiomics in radiology

Candidate
Eleonora Barcali

Supervisor
Prof. Leonardo Bocchi

PhD Coordinator
Prof. Fabio Schoen

Università degli Studi di Firenze, Dipartimento di Ingegneria dell'Informazione (DINFO).

A quel che é stato, a quel che é e a quel che sará...
If you can dream it, you can do it!

Acknowledgments

Summary

The assessment of bone mechanical properties is fundamental for improving diagnostic accuracy and fracture risk prediction. This thesis explores an integrated approach that combines radiomic analysis, mechanical testing, and finite element analysis (FEA) to characterize bone structure and stiffness. The overarching objective is to establish a quantitative framework capable of linking microstructural imaging features with mechanical behavior, thereby advancing non-invasive methods for bone quality evaluation. The study focuses on feline bone specimens, selected as a preclinical model to investigate the relationship between imaging-derived radiomic features and mechanical parameters. The research workflow begins with high-resolution CT image acquisition, followed by a semi-automatic segmentation process to isolate regions of interest. A dedicated Python-based radiomic feature extractor is employed to quantify microstructural properties, encompassing textural, morphological, and intensity-based descriptors. Given the high dimensionality of radiomic data, Principal Component Analysis (PCA) is applied to identify the dominant patterns underlying bone structure. The analysis reveals that the first three principal components (PC1, PC2, and PC3) collectively explain over 90% of the variance in the dataset:

- PC1 encapsulates large-scale structural variations, primarily reflecting bone size and shape.

- PC2 captures mid-scale textural patterns, related to trabecular distribution and anisotropy.

- PC3 highlights fine-scale microstructural heterogeneity, showing the strongest correlation with mechanical properties, particularly stiffness and elastic modulus.

These findings underscore the pivotal role of microstructural details in determining bone mechanical performance. To experimentally validate these relationships, mechanical testing is conducted, including three-point bending experiments, which provide force-displacement curves as a benchmark for computational modeling. From these curves, a recalibrated elastic modulus, E^*, is derived, ensuring standardization across different FEA models. This parameter allows for a more accurate mechanical characterization of the bone while maintaining consistency across numerical simulations. To further assess the reliability of the computational models, Dynamic Time

Warping (DTW) is applied to compare the simulated and experimental force-displacement curves. A randomization test is then employed to establish statistical significance thresholds for the DTW distances, ensuring that observed deviations between numerical predictions and experimental results remain within an acceptable range. The results of this study demonstrate a robust correlation between radiomic features and bone mechanical properties, paving the way for predictive models capable of estimating bone strength directly from imaging data. This novel approach enhances the potential of radiomics in non-invasive bone health assessment, with direct implications for both preclinical research and clinical applications. Future developments should focus on expanding the dataset to human bone samples, refining the segmentation methodology to improve feature extraction accuracy, and optimizing the integration of radiomic data into patient-specific FEA models. By addressing these aspects, this research lays the groundwork for a more comprehensive understanding of bone biomechanics, with significant potential for advancing diagnostic and therapeutic strategies in bone-related pathologies.

Contents

Chapter 1

Introduction

The capacity to evaluate bone quality is fundamental in multiple areas of biomedical research, especially for comprehending bones' mechanical behavior, enhancing clinical diagnostics, and refining orthopedic implant designs. Bones fulfill multiple essential functions; they act not only as rigid frameworks for mechanical support but also as dynamic, living tissues that are vital for maintaining the body's overall functionality. In addition to facilitating movement and safeguarding vital organs, bones play key roles in regulating minerals, producing blood cells, storing energy, and continuously remodeling to adapt to shifting mechanical and metabolic demands. This remodeling process is directed by the coordinated activities of osteoclasts, which resorb bone, and osteoblasts, which form new bone [36, 107]. This equilibrium ensures that bones retain their structural integrity while adapting to the mechanical stresses they encounter. The continuous cycle of replacing old or damaged bone with new tissue is regulated by hormonal signals, including parathyroid hormone (PTH), calcitonin, and sex hormones such as estrogen, which are crucial for maintaining bone mass. The balance between resorption and formation is essential in preventing conditions like osteoporosis, where excessive bone loss weakens the bone's structure and heightens fracture risk. At the macroscopic level, bones are composed of both compact and spongy tissues, each fulfilling distinct roles. Compact bone provides resilience and resistance to compressive forces, whereas spongy bone, with its trabecular arrangement, optimizes mechanical load distribution. This composition enables bones to combine strength and flexibility effectively. On a microscopic scale, bones consist of a matrix made of type I collagen and hydroxyapatite

crystals, a structure that grants them mechanical strength and elasticity. As key mineral reservoirs, particularly for calcium and phosphate, bones contribute to vital physiological functions like muscle contraction, nerve signaling, and energy metabolism. Through the regulation of calcium and phosphate release into the bloodstream, bones help maintain mineral homeostasis, essential for processes. Additionally, bones contain bone marrow, which is vital for hematopoiesis or blood cell formation. Red bone marrow, found in spongy bone, produces red blood cells for oxygen transport, white blood cells for immune defense, and platelets for blood clotting. Yellow marrow, located in long bone cavities, serves as an energy reserve and can revert to red marrow in response to increased physiological demands, such as in severe blood loss.

Traditional methods like Dual-Energy X-Ray Absorptiometry (DEXA), a technique that works by using two X-ray beams of different energy levels to measure the absorption of each beam by bone and soft tissue providing a precise assessment of bone mineral content and density, are widely used to measure Bone Mineral Density (BMD) and assess bone structural properties [37,66,68,135]. BMD quantifies mineral content within a given bone area and has long been the standard for diagnosing osteoporosis and estimating fracture risk. Although effective in specific cases, this technique is limited in capturing the intricate microarchitecture of bone, such as trabecular arrangements in spongy bone or osteon quality in cortical bone, thus restricting its capacity to fully elucidate the mechanical properties vital for predicting bone fragility and fracture susceptibility [37, 135]. Bones can exhibit normal BMD yet remain fragile if their microstructure is compromised. Additionally, BMD lacks insight into material composition aspects like collagen quality or mineralization levels, both of which significantly impact mechanical strength. Moreover, BMD is a static measurement that does not reflect the dynamic bone turnover process. Recently, the notion of bone quality has emerged as a valuable complement to BMD. Bone quality encompasses structural, compositional, and functional characteristics, providing a more holistic view of a bone's fracture resistance. The examination of bone quality offers a broader understanding by incorporating various factors beyond mineral density, such as the bone's microstructural, compositional, and mechanical characteristics. Microarchitecture significantly influences bone strength, as the structural organization of trabeculae in spongy bone and osteons in cortical bone aids effective load distribution. Loss of trabecular connectivity

or reduced thickness can severely impair bone strength even when BMD is adequate. Similarly, the integrity of the bone matrix, including collagen and mineralization quality, is essential for bones to withstand mechanical stress and resist fractures.

Mechanical properties such as fracture resistance, energy absorption, and hardness are also critical facets of bone quality. These attributes can be evaluated using laboratory methods like compression and bending tests or computational models such as finite element analysis (FEA), which leverages Computed Tomography (CT) images to estimate bone behavior under stress. Bone turnover, representing the dynamic balance between resorption and formation, provides a more nuanced perspective on bone quality. While BMD offers a static snapshot, turnover rates reveal changes that BMD may overlook. A high turnover rate can lead to bone loss and structural decline, weakening bones even with normal BMD values. Conversely, low turnover may result in microdamage accumulation, reducing the bone's ability to self-repair.

The focus on bone quality signals a paradigm shift in skeletal health assessment. While BMD remains valuable for understanding bone mass, bone quality provides a more comprehensive view of bone strength and fragility by considering factors beyond what BMD alone captures. This shift is pivotal in explaining why some individuals with normal BMD experience fractures, whereas others with low BMD do not.

Radiomics has recently emerged as a transformative approach to analyzing medical images, aligning with the evolving concepts of bone quality by enabling the extraction of quantitative information from imaging modalities [50,153]. Radiomics entails extracting a multitude of features related to shape, texture, and intensity from regions of interest within images, allowing for a more profound understanding of tissue characteristics beyond visual observation. Initially developed for oncology tumor analysis, radiomics shows potential but is still in its infancy in studying bone microstructure. In clinical settings, incorporating bone quality assessments alongside BMD measurements could enhance osteoporosis diagnostics and fracture risk evaluation. Advanced tools like high-resolution micro-CT, quantitative MRI, and FEA now permit more detailed bone quality evaluations, providing clinicians with a deeper understanding of bone resilience and fragility. By integrating both bone density and quality, healthcare providers can tailor treatment plans more effectively, improving patient outcomes and reducing fracture risks in

individuals with compromised bone health [34, 120].

1.1   The Objective

The primary objective of this study is to develop a novel and comprehensive methodology for the early detection of osteoporosis by analyzing radiomic features extracted from Computed Tomography (CT) images. Unlike traditional diagnostic approaches, which rely heavily on bone mineral density (BMD) measurements obtained via Dual-Energy X-ray Absorptiometry (DEXA), this research leverages advanced radiomic analysis to capture subtle variations in bone microarchitecture. DEXA provides a quantitative assessment of BMD by using two X-ray beams of different energy levels to calculate the absorption by bone and soft tissue. However, its limitation lies in its inability to assess bone quality beyond density. By contrast, radiomics offers a pathway to uncover imaging biomarkers that reflect bone microstructural integrity and heterogeneity, which are critical for predicting bone strength and fracture risk.

This study aims to address key gaps in osteoporosis diagnostics by integrating radiomic and biomechanical approaches, combining imaging data with finite element analysis (FEA) to simulate and validate the mechanical behavior of bones. The FEA method, a computational modeling technique, was employed to simulate the response of bone structures to mechanical loading, enabling the prediction of bone strength and mechanical properties. These simulations were validated and refined by comparing their outcomes with experimental mechanical tests conducted on bone specimens. By coupling these approaches, the study provides a framework for identifying imaging biomarkers with the potential to anticipate the early onset of osteoporosis.

1.2   Contributions

Dual-Energy X-ray Absorptiometry (DEXA) provides a two-dimensional (2D) assessment of bone mineral density (BMD), expressed as the amount of mineral content per unit area:

$$BMD = \frac{\text{grams of mineral}}{\text{area in cm}^2}.$$

This measurement has been extensively used in clinical practice and is considered the gold standard for diagnosing osteoporosis. However, DEXA has notable limitations, as it captures only planar information about the mineral content of a defined region, without providing volumetric data. Moreover, DEXA-derived measurements include posterior spinal elements, which can compromise accuracy in cases of severe spinal degeneration, scoliosis, or prior lumbar surgeries [68,135]. These issues may lead to inaccuracies in estimating BMD, potentially overestimating or underestimating bone density.

In contrast, Computed Tomography (CT) enables a three-dimensional (3D) assessment of bone mineral content, offering volumetric data and localized evaluations of specific regions of interest (ROIs). This capability is particularly valuable in studying bone microarchitecture, such as trabecular structures within the vertebral body, which are highly predictive of fracture risk [76]. While CT's Hounsfield Units (HU) provide a more comprehensive understanding of bone quality, the lack of clinical standardization and consensus for HU-based bone assessment remains a challenge [116].

Despite these challenges, HU values allow for precise localization of BMD across an entire structure or within specific ROIs. Numerous studies have attempted to correlate HU values with DEXA-derived T-scores, grouping patients based on DEXA results and calculating the average HU values for each group to identify potential correlations [81,133]. However, these studies often focus solely on BMD or HU values, without addressing the underlying mechanical characteristics of bone.

1.2.1 Study Plan and Methodology

This study follows a structured, multi-phase approach to explore the relationship between CT-derived radiomic features and bone mechanical properties. The methodology integrates radiomic analysis, experimental mechanical testing, and finite element analysis (FEA) to establish a quantitative framework for assessing bone quality.

1. **Image Acquisition and Preprocessing**: High-resolution CT scans of 11 bone samples (6 humeri and 5 femurs) were acquired to ensure high-quality data for radiomic analysis. Semi-automatic segmentation, combining global thresholding and manual refinement, was used to isolate regions of interest (ROIs) while ensuring reproducibility.

2. **Radiomic Feature Extraction**: A custom feature extraction tool de-

veloped in 3D Slicer identified critical radiomic features reflecting bone microarchitecture. Metrics derived from Grey-Level Co-occurrence Matrix (GLCM) and Grey-Level Size Zone Matrix (GLSZM) were extracted to capture texture, density variations, and trabecular organization.

3. **Experimental Mechanical Testing**: Bone specimens underwent mechanical tests, including three-point bending experiments, to quantify stiffness and strength. These measurements provided a direct benchmark for evaluating the performance of computational models.

4. **Finite Element Analysis (FEA)**: Computational simulations were performed to predict bone behavior under mechanical loading. The effective modulus (E^*) was derived from force-displacement curves to ensure a standardized comparison between models.

5. **Material Property Assignment via Bonemat**: The elastic modulus distribution was mapped to the finite element mesh using Bonemat [147], ensuring accurate biomechanical representation by linking CT density values to material properties.

6. **Dimensionality Reduction and Feature Selection**: Principal Component Analysis (PCA) was applied to reduce the complexity of radiomic data, isolating the most relevant features for correlation with mechanical properties. The first three components (PC1, PC2, and PC3) captured over 90% of the variance, with PC3 showing the strongest correlation with E^*.

7. **Correlation Analysis and Predictive Framework**: Pearson correlation analysis was conducted to assess relationships between selected radiomic features and mechanical properties. The study evaluates the potential of radiomic biomarkers as early indicators of bone strength and osteoporosis risk.

8. **Validation with Dynamic Time Warping (DTW)**: To compare experimental and simulated force-displacement curves, DTW was applied, followed by a randomization test to establish statistical significance thresholds. This step ensured that observed deviations remained within an acceptable range, validating the reliability of the computational models.

This multidisciplinary approach integrates advanced imaging, computational biomechanics, and statistical modeling, offering a more comprehensive and clinically relevant assessment of bone quality.

1.2.2 Novel Contributions and Rationale

This study bridges the gap between imaging biomarkers and bone mechanical properties by integrating radiomic feature extraction with computational modeling and experimental validation. The key contributions include:

- **Beyond HU and BMD**: Traditional bone assessments rely on Hounsfield Units (HU) and Bone Mineral Density (BMD), which may overlook microstructural details. By incorporating radiomic analysis, this study captures fine-scale bone features that influence mechanical behavior.

- **Linking Structure to Mechanics**: By combining radiomic analysis, mechanical testing, and FEA, this study establishes quantitative relationships between bone microarchitecture and mechanical properties such as stiffness and E^*, enhancing predictive capabilities.

- **Accurate Material Property Assignment**: The use of Bonemat for region-specific elastic modulus mapping improves the fidelity of FEA simulations, ensuring a closer alignment with experimental results.

- **Dimensionality Reduction and Feature Optimization**: The PCA-based feature selection refines the analysis by isolating the most influential radiomic descriptors, minimizing redundancy while preserving key structural information.

- **Early Detection Framework**: The integration of radiomic biomarkers, computational modeling, and mechanical validation supports the development of non-invasive tools for early osteoporosis detection and fracture risk assessment.

- **Validation through DTW and Statistical Analysis**: By incorporating DTW for force-displacement alignment and randomization tests for statistical validation, the study ensures that model predictions are statistically robust and clinically meaningful.

This research lays the groundwork for future clinical applications, where radiomics can be integrated into patient-specific biomechanical assessments to improve diagnostic precision and personalized treatment planning. By extending these methodologies to human bone models, the framework developed in this study could contribute to early detection strategies, optimized treatment pathways, and improved patient outcomes in the field of orthopedic and musculoskeletal research.

1.2.3   Conclusion

This study contributes to the field of bone health assessment by integrating advanced radiomic techniques with biomechanical modeling. Unlike previous research focused solely on BMD or HU values, our approach establishes a direct connection between bone microarchitecture and mechanical performance. This innovative framework enhances the accuracy of bone quality evaluations, providing a foundation for more effective diagnostic and therapeutic strategies in managing osteoporosis and related conditions.

Chapter 2

Literature Review

This chapter provides a detailed analysis of bone assessment techniques, focusing on the evolution of diagnostic methods from traditional approaches like DEXA, CT, and MRI to advanced techniques such as radiomics. By emphasizing the integration of radiomics with Artificial Intelligence (AI), the chapter highlights their potential in delivering personalized, predictive diagnostic solutions for conditions like osteoporosis. Additionally, this chapter aims to establish the significance of focusing on bone health due to its critical role in structural support, mineral balance, and overall well-being.

2.1 Imaging Techniques

Bone pathologies remain a significant area of clinical and research interest, with most issues linked to concerns about bone integrity, a critical factor in bone strength. Bone strength itself is a multifaceted property, resulting from the interplay between bone quantity (the amount of mineralized tissue) and bone quality (the structural and material properties of bone). Bone quantity contributes approximately 70% of overall bone strength, primarily through bone mineral density (BMD). Bone quality, which accounts for around 20%, encompasses aspects such as microarchitecture, mineralization, and collagen integrity, while the remaining 10% stems from other intrinsic factors. Despite the availability of established methods for measuring bone quantity, a standardized clinical method for evaluating bone quality remains elusive [118].

Osteoporosis, one of the most prevalent bone diseases, exemplifies the need for improved assessment techniques. This condition, characterized by decreased bone mass and deterioration of bone tissue, leads to a disruption in bone microarchitecture and a consequent reduction in strength, increasing the risk of fractures. Osteoporosis affects approximately 30% of women in the United States and Europe, with studies estimating that 40% of postmenopausal women and 30% of men will experience an osteoporosis-related fracture during their lifetime [69, 128, 142]. Moreover, the disease often remains asymptomatic until fractures occur, which can be particularly severe and life-threatening in men. These factors underline the importance of early detection and intervention to mitigate healthcare costs and improve patient outcomes [82, 118]. Beyond fracture risk, bone quality plays a pivotal role in the success of prosthetic surgeries. A reduction in bone quality can lead to increased implant failure rates and compromised prosthetic stability. Inflammation and the surrounding bone's capacity to maintain its integrity further exacerbate these risks [110]. Given the growing recognition of bone health as a cornerstone of overall well-being, researchers have turned their attention to a wide array of techniques for assessing bone strength. These methods range from in vivo imaging techniques to in vitro and indirect approaches. However, the sheer diversity of available techniques can be overwhelming for both researchers and clinicians. The scientific literature often lacks a cohesive framework for evaluating these methods in the context of both bone quality and quantity. Consequently, this chapter aims to provide a comprehensive overview of the most effective and promising techniques, focusing on their clinical applicability and ability to address the challenges posed by conditions like osteoporosis.

2.1.1 Considerations on Radiation Exposure

When discussing imaging techniques, particularly those involving ionizing radiation, it is crucial to consider the radiation dose absorbed by the patient. The Gray (Gy) measures the absorbed dose, representing the amount of radiation energy deposited in tissue (1 Gy = 1 Joule per kilogram of tissue). Meanwhile, the Sievert (Sv) accounts for both the type of radiation and the tissue's sensitivity, providing a measure of effective dose. For instance, in diagnostic radiology, 1 Gy of absorbed dose typically corresponds to 1 Sv of effective dose, although the actual risk may vary depending on the body part being scanned [41]. Radiation exposure from common imaging modal-

ities varies widely. A DEXA scan, for example, delivers a minimal dose of approximately 1 μSv, equivalent to just a few hours of natural background radiation. In contrast, a CT scan of the lumbar spine can deliver a dose of around 0.04 mSv, comparable to 10 hours of air travel at cruising altitude [98]. While these doses are generally considered low, minimizing exposure remains a priority, particularly for patients requiring repeated imaging. By analyzing these techniques within the broader context of bone pathologies, this chapter seeks to establish a clearer understanding of their role in addressing bone health challenges. Ultimately, the integration of traditional and advanced imaging approaches, such as radiomics, offers the potential to bridge existing gaps in bone quality assessment and contribute to more effective prevention and treatment strategies.

2.2 Classification of Imaging Techniques

Bone quality and quantity can be assessed using a variety of techniques. Bone quantity refers to the amount of mineralized tissue in a given area $(\frac{g}{cm^2})$, as determined by DEXA, or in a volume $(\frac{g}{cm^3})$, as assessed by quantitative computed tomography (QCT) [118]. Bone quality, on the other hand, describes the compositional and structural aspects of bone that contribute to its strength, independent of BMD. These aspects include bone turnover, microarchitecture, mineralization, micro-damage, and the composition of the bone matrix and mineral content [29]. Bone quality encompasses a wide range of properties, spanning from macroarchitecture to microarchitecture, as well as intrinsic biomechanical characteristics that confer strength and stiffness to bone tissue [42]. However, only a subset of these properties can be assessed using techniques routinely applicable in clinical practice. These methods are generally categorized into direct and indirect approaches:

- Direct techniques: These measure bone properties directly from acquired images, often utilizing ionizing or non-ionizing modalities.

- Indirect techniques: These rely on post-processing of images to calculate parameters such as bone strength or quality.

In this literature review, we focus on in vivo techniques applicable to human patients, excluding ex vivo and in vitro methods, as they fall outside the scope of this work. To provide clarity, the techniques are categorized into six main groups, summarized in Table 2.1:

1. Direct imaging techniques with ionizing radiation: X-ray and Computed Tomography (CT).

2. Direct imaging techniques without ionizing radiation: Ultrasonography (US) and Magnetic Resonance Imaging (MRI).

3. Direct non-imaging techniques: Quantitative Ultrasound (QUS), Neutron Activation Analysis, Gravimetric, and Chemical Analysis.

4. Indirect imaging techniques: Trabecular Bone Score (TBS), Bone Strength Index (BSI), and Quantitative Ultrasound Index (QUI).

5. Ionizing imaging techniques.

6. Emerging advanced modalities, such as high-resolution peripheral QCT (HR-pQCT) and Cone Beam CT (CBCT).

2.2.1 RX-Related Techniques

Among ionizing techniques, the commonly referenced DEXA is considered the gold standard for evaluating bone mineral content and BMD. DEXA is a cost-effective and widely available approach that involves low radiation exposure (about 1 μSv) and has high reproducibility. It measures areal BMD (aBMD), providing T-scores based on comparison with a reference population [75,97], as already described in the previous chapter. Other techniques include Single-energy X-ray Absorptiometry (SXA), a non-invasive and rapid method. However, SXA can be limited by fractures in the ROI, which may interfere with BMD measurements.

2.2.2 CT-Related Techniques

Different types of CT approaches are commonly used to study bone, each offering distinct benefits depending on the clinical or research objectives. Conventional Computed Tomography (CT) is extensively applied in clinical diagnostics to produce high-resolution, three-dimensional images of bone structures. Its primary value lies in the detection of fractures, tumors, and other bone abnormalities due to its excellent spatial resolution and capability to display complex anatomical structures across multiple planes [1]. Although conventional CT does not directly measure BMD like Quantitative CT (QCT), as already explained in the previous chapter, it can provide

Hounsfield Unit (HU) values that correlate with bone density. However, because HU values lack standardization for bone quality assessment, they offer less accuracy compared to specialized imaging methods [1,75]. Despite these limitations, conventional CT provides distinct advantages. It is widely available and commonly used in clinical settings, making it an accessible option for initial diagnostic assessments, particularly for patients who are unable to undergo more specialized imaging techniques. Furthermore, conventional CT's ability to create volumetric reconstructions supports indirect assessments of bone by enabling post-processing analyses, allowing researchers to approximate mechanical properties of bone structures through morphological evaluation. Among advanced techniques, Quantitative CT (QCT) stands out as one of the most widely adopted methods for analyzing bone parameters, both quantitatively and qualitatively. Unlike DEXA, QCT offers a three-dimensional evaluation of bone structure. This ability to differentiate between cortical and trabecular bone is crucial for understanding overall bone strength, as these two types of bone play different roles in load-bearing and resistance to fracture [16]. QCT calculates volumetric bone mineral density (vBMD), expressed in grams per cubic centimeter ($\frac{g}{cm^3}$). This measurement accounts for the actual bone volume rather than being dependent on bone size or surface area, as is the case with areal BMD from DEXA. One of QCT's main advantages is its size-independent measurement, which is especially important for evaluating bones with varying geometries, such as the vertebrae or femur. Additionally, it allows for the acquisition of larger portions of bone in seconds, reducing scan time. However, QCT's primary limitation is the relatively high radiation dose required (up to 100 mSv) compared to DEXA's 1 μSv [17]. This has led to the development of more advanced techniques, such as peripheral QCT (pQCT) and high-resolution pQCT (HR-pQCT). High-Resolution pQCT (HR-pQCT) represents the cutting edge of QCT technology, offering voxel sizes as small as 80 μm. This resolution enables detailed studies of bone microstructure at peripheral sites, such as the distal radius and tibia [62]. HR-pQCT provides a range of structural parameters, including:

- Bone volume fraction (BV/TV): the relative amount of bone volume within the total tissue volume.

- Trabecular thickness (Tb.Th): the average thickness of trabeculae.

- Trabecular separation (Tb.Sp): the spacing between trabeculae.

- Trabecular number (Tb.N): the number of trabeculae per unit length.

One of HR-pQCT's key advantages is its relatively low radiation dose (3-5 μSv), making it suitable for longitudinal studies where repeated measurements are necessary [7]. Emerging CT techniques, such as Cone Beam Computed Tomography (CBCT), are also gaining attention for their ability to provide highly accurate 3D representations of bone structure with sub-millimetric resolution. CBCT offers a significantly lower radiation dose than conventional CT, making it particularly useful for dental and maxillofacial applications. Additionally, Dual-Energy QCT (DE-QCT) enhances accuracy by using two different X-ray energy levels to better differentiate bone density from soft tissue, improving osteoporosis assessments.

2.2.3   Ultrasound-Related Techniques

Ultrasound (US)-based techniques are gaining popularity in bone health assessments due to their non-ionizing nature, portability, and relatively low cost. Unlike X-rays or CT, US techniques use sound waves to evaluate bone and surrounding tissues. The most promising of these methods is Radiofrequency US Multi-Spectrometry (REMS), a recent advancement in bone imaging. REMS assesses BMD and fracture risk by analyzing unfiltered raw US signals backscattered by bone structures. These raw signals are processed using proprietary algorithms, which compare their spectral representation with a reference database of healthy bone [117]. REMS is particularly effective at critical sites such as the lumbar vertebrae and femoral neck. The primary output is BMD(US), a diagnostic index for clinical use. Studies show that REMS results correlate well with DXA-derived BMD values, offering good agreement with DXA diagnoses, considered the gold standard in osteoporosis detection [30]. REMS's lack of radiation exposure makes it ideal for repeated measurements and long-term monitoring of bone health. Other US techniques, such as Quantitative Ultrasound (QUS), evaluate bone properties indirectly by analyzing how sound waves propagate through bone and surrounding tissues. Metrics such as Speed of Sound (SOS) and Broadband Ultrasound Attenuation (BUA) infer bone stiffness and density. Although less precise than CT or DEXA, QUS provides valuable insights into bone elasticity and strength at peripheral sites like the heel or wrist [1].

2.2.4 MRI-Related Techniques

One of MRI's primary advantages over other imaging techniques is its lack of radiation exposure, making it a safe option for evaluating both the central and peripheral skeleton. However, the high costs associated with MRI limit its widespread use for assessing bone structure, despite its availability in developed countries and frequent use in clinical practice. In MRI, cortical bone appears as a low-intensity signal, contrasting with the high-intensity signal from bone marrow. Post-processing techniques enable analyses such as soft tissue visualization, pore content characterization, and quantification of bone and marrow properties at a biochemical level [77, 109]. Structural indices derived from MRI include:

- Apparent trabecular number (app. Tb.N),

- Apparent trabecular thickness (app. Tb.Th),

- Apparent trabecular separation (app. Tb.Sp).

While conventional MRI (1.5T and 3T) lacks the resolution to capture trabecular dimensions (typically 100 μm), High-Resolution MRI (HR-MRI) achieves significantly enhanced resolution (50 x 50 x 200 μm ex vivo, and 156 x 156 x 300 μm in vivo), allowing detailed imaging of trabecular networks, particularly at peripheral sites [1, 22, 141].

2.2.5 RX-Related Techniques

Among ionizing techniques, the commonly referenced DEXA is considered the gold standard for evaluating bone mineral content and BMD. DEXA is a cost-effective and widely available approach that involves low radiation exposure (about 1 μSv) and has high reproducibility. It measures areal BMD (aBMD), providing T-scores based on comparison with a reference population [75, 97], as already described in the previous chapter. Other techniques include Single-energy X-ray Absorptiometry (SXA), a non-invasive and rapid method. However, SXA can be limited by fractures in the ROI, which may interfere with BMD measurements.

2.2.6 CT-Related Techniques

Different types of CT approaches are commonly used to study bone, each offering distinct benefits depending on the clinical or research objectives.

Conventional Computed Tomography (CT) is extensively applied in clinical diagnostics to produce high-resolution, three-dimensional images of bone structures. Its primary value lies in the detection of fractures, tumors, and other bone abnormalities due to its excellent spatial resolution and capability to display complex anatomical structures across multiple planes [1]. Although conventional CT does not directly measure BMD like Quantitative CT (QCT), as already explained in the previous chapter, it can provide Hounsfield Unit (HU) values that correlate with bone density. However, because HU values lack standardization for bone quality assessment, they offer less accuracy compared to specialized imaging methods [1]. Despite these limitations, conventional CT provides distinct advantages. It is widely available and commonly used in clinical settings, making it an accessible option for initial diagnostic assessments, particularly for patients who are unable to undergo more specialized imaging techniques. Furthermore, conventional CT's ability to create volumetric reconstructions supports indirect assessments of bone by enabling post-processing analyses, allowing researchers to approximate mechanical properties of bone structures through morphological evaluation [1]. Among advanced techniques, Quantitative CT (QCT) stands out as one of the most widely adopted methods for analyzing bone parameters, both quantitatively and qualitatively. Unlike DEXA, QCT offers a three-dimensional evaluation of bone structure. This ability to differentiate between cortical and trabecular bone is crucial for understanding overall bone strength, as these two types of bone play different roles in load-bearing and resistance to fracture [16]. QCT calculates volumetric bone mineral density (vBMD), expressed in grams per cubic centimeter ($\frac{g}{cm^3}$). This measurement accounts for the actual bone volume rather than being dependent on bone size or surface area, as is the case with areal BMD from DEXA. One of QCT's main advantages is its size-independent measurement, which is especially important for evaluating bones with varying geometries, such as the vertebrae or femur. Additionally, it allows for the acquisition of larger portions of bone in seconds, reducing scan time. However, QCT's primary limitation is the relatively high radiation dose required (up to 100 mSv) compared to DEXA's 1 μSv [17]. This has led to the development of more advanced techniques, such as peripheral QCT (pQCT) and high-resolution pQCT (HR-pQCT). High-Resolution pQCT (HR-pQCT) represents the cutting edge of QCT technology, offering voxel sizes as small as 80 μm. This resolution enables detailed studies of bone microstructure at peripheral sites,

such as the distal radius and tibia [62]. HR-pQCT provides a range of structural parameters, including:

- Bone volume fraction (BV/TV): the relative amount of bone volume within the total tissue volume.

- Trabecular thickness (Tb.Th): the average thickness of trabeculae.

- Trabecular separation (Tb.Sp): the spacing between trabeculae.

- Trabecular number (Tb.N): the number of trabeculae per unit length.

One of HR-pQCT's key advantages is its relatively low radiation dose (3-5 μSv), making it suitable for longitudinal studies where repeated measurements are necessary [7]. Emerging CT techniques, such as Cone Beam Computed Tomography (CBCT), are also gaining attention for their ability to provide highly accurate 3D representations of bone structure with sub-millimetric resolution. CBCT offers a significantly lower radiation dose than conventional CT, making it particularly useful for dental and maxillofacial applications. Additionally, Dual-Energy QCT (DE-QCT) enhances accuracy by using two different X-ray energy levels to better differentiate bone density from soft tissue, improving osteoporosis assessments.

2.2.7 Ultrasound-Related Techniques

Ultrasound (US)-based techniques are gaining popularity in bone health assessments due to their non-ionizing nature, portability, and relatively low cost. Unlike X-rays or CT, US techniques use sound waves to evaluate bone and surrounding tissues. The most promising of these methods is Radiofrequency US Multi-Spectrometry (REMS), a recent advancement in bone imaging. REMS assesses BMD and fracture risk by analyzing unfiltered raw US signals backscattered by bone structures. These raw signals are processed using proprietary algorithms, which compare their spectral representation with a reference database of healthy bone [117]. REMS is particularly effective at critical sites such as the lumbar vertebrae and femoral neck. The primary output is BMD(US), a diagnostic index for clinical use. Studies show that REMS results correlate well with DXA-derived BMD values, offering good agreement with DXA diagnoses, considered the gold standard in osteoporosis detection [30]. REMS's lack of radiation exposure makes it ideal for repeated measurements and long-term monitoring of bone health. Other

US techniques, such as Quantitative Ultrasound (QUS), evaluate bone properties indirectly by analyzing how sound waves propagate through bone and surrounding tissues. Metrics such as Speed of Sound (SOS) and Broadband Ultrasound Attenuation (BUA) infer bone stiffness and density. Although less precise than CT or DEXA, QUS provides valuable insights into bone elasticity and strength at peripheral sites like the heel or wrist [1].

2.2.8   MRI-Related Techniques

One of MRI's primary advantages over other imaging techniques is its lack of radiation exposure, making it a safe option for evaluating both the central and peripheral skeleton. However, the high costs associated with MRI limit its widespread use for assessing bone structure, despite its availability in developed countries and frequent use in clinical practice. In MRI, cortical bone appears as a low-intensity signal, contrasting with the high-intensity signal from bone marrow. Post-processing techniques enable analyses such as soft tissue visualization, pore content characterization, and quantification of bone and marrow properties at a biochemical level [77, 109]. Structural indices derived from MRI include:

- Apparent trabecular number (app. Tb.N),

- Apparent trabecular thickness (app. Tb.Th),

- Apparent trabecular separation (app. Tb.Sp).

While conventional MRI (1.5T and 3T) lacks the resolution to capture trabecular dimensions (typically 100 μm), High-Resolution MRI (HR-MRI) achieves significantly enhanced resolution (50 x 50 x 200 μm ex vivo, and 156 x 156 x 300 μm in vivo), allowing detailed imaging of trabecular networks, particularly at peripheral sites [1, 22, 141].

2.3   Non-Imaging Techniques

In addition to imaging techniques, several non-imaging methods are used to assess bone quality and strength. These techniques rely on the analysis of bone composition or biomechanical properties, offering valuable insights without producing visual images of bone. However, their indirect nature highlights key limitations in capturing the complexity of bone microarchitecture, emphasizing the need for advanced methodologies. Trabecular Bone

Score (TBS) is one of the most well-known non-imaging methods. TBS is a textural index that quantifies variations in the gray levels of DEXA images, providing an indirect assessment of bone microarchitecture. High TBS values indicate a dense, well-connected trabecular network, while low TBS values suggest fragile, porous bone [54]. TBS is particularly effective for predicting fracture risk by evaluating trabecular structure and connectivity. Although currently applied primarily to DEXA scans of the lumbar spine, ongoing research explores its applicability to other sites, such as the femoral neck. Despite its utility, TBS remains limited in its ability to assess deeper aspects of bone heterogeneity and biomechanical performance. Another emerging technique is the Bone Strength Index (BSI), which combines DEXA measurements with finite element models to estimate bone strength. BSI incorporates bone geometry and material properties to evaluate resistance to mechanical stress. This index is especially valuable for understanding how bones respond to load-bearing activities, providing insights into fracture risk that extend beyond BMD alone [154]. However, like TBS, BSI does not directly assess bone microarchitecture and remains constrained by its reliance on DEXA-derived inputs. Neutron Activation Analysis (NAA) is another non-imaging technique that evaluates bone composition by activating calcium isotopes in the bone and quantifying the resulting gamma radiation. While highly accurate, NAA is primarily confined to research settings due to the complexity and cost of the equipment required. Similarly, chemical analysis methods, such as collagen crosslinking analysis, offer insights into the biomechanical properties of bone tissue. These methods assess the quantity and quality of collagen in the bone matrix, which significantly contributes to bone elasticity and fracture resistance [166]. However, their applicability in clinical practice remains limited by their invasive nature and the need for specialized facilities.

2.4   Traditional Bone Imaging limits and the Evolution to Radiomics

DEXA is a technique that provides the most useful quantitative data on bone mineral density (BMD). However, it is limited in its ability to evaluate other crucial factors, such as bone microstructure, which plays a significant role in bone strength and fracture risk. High-resolution techniques like micro-computed tomography (micro-CT) offer detailed insights into tra-

becular and cortical bone architecture, but their high cost and significant radiation exposure restrict their use to research environments [15, 77]. Non-imaging techniques, while valuable, also exhibit notable limitations in their ability to fully capture the complex interplay between bone composition, microarchitecture, and biomechanical properties. Methods like Trabecular Bone Score (TBS) and Bone Strength Index (BSI) provide indirect assessments that are constrained by their reliance on DEXA imaging. Techniques such as Neutron Activation Analysis (NAA) and chemical analysis are highly accurate but are largely restricted to research environments due to their complexity and specialized requirements. These gaps underscore the need for advanced approaches that can bridge the divide between indirect evaluations and the intricate structural and material properties of bone. These limitations, shared by both traditional imaging and non-imaging methods, highlight a growing need for more sophisticated techniques capable of capturing the complex microarchitecture of bone. This is where radiomics becomes essential. Radiomics extends beyond the capabilities of traditional and non-imaging methods by enabling the extraction of high-dimensional quantitative features from medical images. These features provide detailed information on tissue heterogeneity, texture, and structural organization. Unlike conventional techniques that focus primarily on BMD, radiomics can reveal deeper insights into bone quality by analyzing subtle image patterns that correlate with mechanical properties and fracture risk [153]. As the central focus of this thesis, radiomics presents an opportunity to address the shortcomings of traditional bone imaging methods and non-imaging approaches. By leveraging advanced image analysis, radiomics integrates imaging and computational analysis to provide a comprehensive assessment of bone quality and strength. It offers the potential to revolutionize bone health evaluation, paving the way for predictive and personalized approaches to diagnosing and managing bone diseases such as osteoporosis [165].

2.4.1   Radiomics

Radiomics represents a substantial advancement in medical imaging, enabling the high-throughput extraction of quantitative features from medical images [1]. This approach examines variations in shape, texture, and intensity within bone tissue, facilitating the quantification of structural characteristics that are often overlooked by traditional imaging techniques. By analyzing these features, radiomics offers deeper insights into bone strength, par-

ticularly in predicting mechanical properties and fracture susceptibility [54].

Radiomics Workflow

The radiomics workflow consists of several essential stages, each contributing to the extraction of meaningful data and the development of predictive models:

1). Image Acquisition: High-quality imaging is the cornerstone of reliable radiomic analysis. In the context of bone assessments, CT imaging is frequently used due to its ability to capture detailed representations of trabecular and cortical bone. Ensuring standardized imaging protocols is essential to maintain consistency across different datasets.

2). Preprocessing: Preprocessing steps are critical to minimizing variability and ensuring comparability across studies. These steps include normalization, resampling, and noise reduction, which help standardize images and improve the reliability of extracted features [62].

3). Segmentation: Segmentation involves delineating regions of interest (ROIs) to isolate specific areas of the bone for analysis. While manual segmentation is common in research, semi-automated tools like 3D Slicer are increasingly used to improve reproducibility and efficiency. Effective segmentation ensures that radiomic features accurately reflect bone structures without interference from surrounding tissues.

4). Feature Extraction: Radiomic features are categorized into the following types, each offering unique insights into bone structure and mechanics:

- **First-order statistics**: These features describe the intensity distribution of voxels within the ROI, including mean intensity, standard deviation, and skewness.

- **Texture features**: These quantify spatial relationships between voxels, which are particularly valuable for analyzing trabecular bone. For instance, the Gray-Level Co-occurrence Matrix (GLCM) provides metrics such as contrast, correlation, and entropy, capturing heterogeneity and organization within the bone microarchitecture.

- **Higher-order features**: These involve complex transformations, such as wavelet decompositions, which reveal intricate patterns and structures not apparent through traditional analysis.

5). Dimensionality Reduction: Radiomic datasets are often high-dimensional, requiring techniques such as Principal Component Analysis (PCA) to isolate the most informative features. This step reduces computational demands while preserving crucial structural information [141].

6). Model Development: The extracted features are used to develop predictive models, such as support vector machines (SVMs) or random forests. These models correlate radiomic features with clinical outcomes, including fracture risk and bone stiffness, enabling the prediction of mechanical properties from imaging data [17].

Advantages of Radiomics in Bone Imaging

Radiomics offers significant advantages over traditional imaging and non-imaging methods. By quantifying subtle image patterns and heterogeneity, radiomics provides a comprehensive understanding of bone quality. Its ability to predict fracture susceptibility and mechanical properties makes it a powerful tool in both research and clinical settings. Furthermore, radiomics bridges the gap between imaging and computational analysis, paving the way for personalized approaches to diagnosing and managing bone diseases, such as osteoporosis. This subsection emphasizes the transformative potential of radiomics in advancing bone imaging, highlighting its role in extracting actionable insights from complex image data and improving patient outcomes.

2.4.2   Radiomics in Bone Health

Radiomics is an advanced imaging analysis technique that facilitates the extraction of quantitative features from medical images [1]. By examining characteristics such as shape, texture, and intensity within bone tissue, radiomics provides a deeper understanding of bone structure and quality beyond what traditional imaging methods can achieve. This approach is particularly valuable for assessing bone microarchitecture and predicting mechanical properties, which are crucial determinants of bone strength and fracture risk [16].

Applications of Radiomics in Bone Health

Radiomics offers a broad range of applications in bone research and clinical practice, enabling a more comprehensive evaluation of bone health:

1. Enhanced Microarchitectural Assessment: Traditional imaging methods, such as DEXA, focus primarily on bone mineral density (BMD) and pro-

vide limited insights into bone quality. Radiomics bridges this gap by quantifying microstructural features, such as the spatial arrangement of trabecular and cortical bone, which play a key role in determining bone strength [75]. These insights allow for a more detailed evaluation of bone health.

2. Prediction of Mechanical Properties: By correlating radiomic features with mechanical testing data, radiomics can predict properties such as bone stiffness and fracture resistance [82]. This capability enhances the assessment of fracture risk, providing a more accurate and non-invasive alternative to traditional methods.

3. Early Detection of Bone Diseases: Radiomics excels in identifying subtle structural changes in bone that may precede the onset of conditions such as osteoporosis. These changes are often missed by conventional imaging techniques. Early detection allows clinicians to initiate treatment sooner, potentially preventing severe bone loss and reducing fracture risk [117].

Advantages of Radiomics

Radiomics provides several advantages over traditional imaging and non-imaging techniques:

- Comprehensive Assessment: Radiomics integrates multiple quantitative features to offer a holistic evaluation of bone health, considering both structural and mechanical attributes.

- Non-Invasive Approach: Unlike invasive or research-specific techniques, radiomics uses existing imaging data, making it accessible for routine clinical use.

- Predictive and Personalized: Radiomics facilitates the development of predictive models that correlate imaging features with clinical outcomes, enabling personalized treatment plans.

Challenges and Future Directions

Despite its potential, radiomics in bone health faces several challenges:

- Standardization: Variability in imaging protocols, preprocessing methods, and feature extraction can reduce reproducibility and limit its clinical adoption. Standardized workflows are essential to ensure consistency across studies and institutions.

- Integration with Advanced Analytics: The high-dimensional nature of radiomic data requires advanced machine learning and artificial intelligence (AI) algorithms to process and interpret complex patterns. Future research should focus on creating validated models that integrate seamlessly into clinical workflows.

Radiomics represents a significant advancement in bone health assessment, providing insights into microarchitectural and mechanical properties that were previously inaccessible through traditional imaging techniques. By offering a comprehensive and non-invasive approach to bone evaluation, radiomics has the potential to transform the early detection, prediction, and management of bone diseases such as osteoporosis. Addressing current challenges, such as standardization and integration with AI, will be crucial to fully realizing its clinical and research potential.

2.4.3   Attempts of Using Radiomics for Studying Bone Density and Osteoporosis

Radiomics has emerged as a transformative approach for studying bone density and osteoporosis, leveraging its ability to extract a wide range of quantitative features from medical images. These features provide insights into the microarchitecture, heterogeneity, and mechanical properties of bone, enabling a deeper understanding of bone quality and its role in conditions like osteoporosis. While traditional methods such as Dual-Energy X-ray Absorptiometry (DEXA) focus primarily on bone mineral density (BMD), radiomics extends the scope of bone evaluation by capturing subtle structural details that conventional techniques often overlook. Numerous studies have explored the application of radiomics in improving diagnostic accuracy, predicting fracture risk, and identifying early signs of osteoporosis. These efforts have collectively demonstrated the potential of radiomics to address the limitations of existing imaging methods and to pave the way for personalized and predictive approaches to bone health assessment. One of the key areas of research has been the application of radiomics to computed tomography (CT) scans for osteoporosis detection. Jiang et al. (2022) developed a radiomic signature model based on features extracted from lumbar vertebrae CT scans. Using tools such as 3D Slicer, the study extracted 1040 radiomic features, including first-order statistics and texture features derived from the Gray-Level Co-occurrence Matrix (GLCM) and Gray-Level Run Length

Matrix (GLRLM). The radiomics-based model demonstrated an area under the curve (AUC) of 0.92, significantly outperforming traditional Hounsfield Unit (HU)-based assessments in detecting lumbar spine osteoporosis. The findings highlight the utility of radiomics as a non-invasive and cost-effective tool for osteoporosis screening, utilizing existing clinical imaging data without the need for additional radiation exposure [64]. Beyond CT imaging, radiomics has been integrated with machine learning algorithms to further enhance its diagnostic and predictive capabilities. Rastegar et al. (2020) analyzed DEXA images, extracting 54 radiomic features from lumbar and femoral regions to classify bone health states into osteoporosis, osteopenia, and normal conditions. The study employed advanced classifiers, including Random Forest and Logit-Boost algorithms, achieving AUC values up to 0.78. These results demonstrate the potential of radiomics combined with machine learning to uncover complex patterns in imaging data that are not discernible through conventional methods [123]. Dental imaging, particularly dental panoramic radiographs (DPRs), has also been explored as a radiomic application for osteoporosis detection. Alzubaidi and Otoom (2020) utilized texture-based radiomic features, such as those derived from Gabor filters and wavelet transforms, in conjunction with machine learning techniques like Self-Organizing Maps and Learning Vector Quantization. The study achieved an impressive sensitivity of 97.1%, demonstrating that DPRs could serve as an accessible alternative to traditional imaging for early detection, particularly in resource-limited settings [4]. These findings suggest that radiomics could expand the applicability of dental imaging beyond its traditional diagnostic scope. Another innovative approach has been the integration of radiomics with finite element analysis (FEA) to improve fracture risk prediction. Villamor et al. (2020) developed hybrid models that combined radiomic texture features with mechanical attributes derived from FEA. By analyzing patient-specific models generated from DEXA data, the study demonstrated improved predictive accuracy for osteoporotic hip fractures. This integration of radiomic features with biomechanical modeling provides a comprehensive assessment of bone behavior under stress, addressing a critical gap in fracture susceptibility evaluation [163]. Texture analysis has consistently emerged as a cornerstone of radiomics research in bone health. Metrics such as contrast, correlation, and entropy, derived from GLCM and other texture matrices, have been identified as key predictors of bone stiffness and fracture risk. Studies have shown that these features

capture subtle variations in trabecular bone organization and heterogeneity, which are often early indicators of osteoporosis and other degenerative bone conditions [21, 54]. Wavelet-based higher-order features have further enhanced the ability of radiomics to detect fine structural details that traditional imaging methods may miss. Despite these advancements, several challenges remain in the application of radiomics for bone health assessment. A significant issue is the lack of standardization in imaging protocols and radiomic workflows. Variability in image acquisition, preprocessing, and feature extraction methods across institutions and studies can lead to inconsistencies in results, limiting the reproducibility and generalizability of radiomics-based models. Efforts to establish standardized guidelines and benchmarks for radiomics in bone research are critical to overcoming this barrier. Feature selection and dimensionality reduction also pose challenges due to the high-dimensional nature of radiomics data. Techniques such as Principal Component Analysis (PCA) and machine learning-based feature selection are often employed to isolate the most informative features while avoiding overfitting. However, ensuring that these selected features retain clinical relevance remains an ongoing area of research. Another significant challenge is the integration of radiomics into clinical workflows. While research studies have demonstrated the potential of radiomics in enhancing bone health assessment, translating these findings into practical diagnostic tools requires validated predictive models and streamlined processes. The integration of radiomics with artificial intelligence (AI) and machine learning offers a promising pathway to address this challenge. AI-based algorithms can process large radiomics datasets, identify complex patterns, and develop robust models that align with clinical needs. In conclusion, radiomics represents a paradigm shift in the study of bone density and osteoporosis. By providing a comprehensive analysis of bone microarchitecture and mechanical properties, it addresses critical gaps left by traditional imaging methods. The numerous studies conducted to date highlight the potential of radiomics in improving diagnostic accuracy, fracture risk prediction, and early detection of bone diseases. However, addressing challenges related to standardization, feature selection, and clinical integration is essential to fully realize the benefits of radiomics in bone health research and practice.

2.5   Conclusion

This chapter aimed to provide a comprehensive review of the advancements in radiomics for studying bone density and osteoporosis. The focus on bone is justified by its critical role in overall health and its susceptibility to debilitating diseases such as osteoporosis, which significantly impact the quality of life and increase healthcare burdens. The chapter highlights the limitations of traditional imaging methods, such as DEXA and CT, in capturing the intricate microarchitecture and mechanical properties of bone. It emphasizes the potential of radiomics to bridge these gaps by offering a non-invasive, high-dimensional analysis of bone structure and quality.

The review explored a range of studies demonstrating the application of radiomics in bone health, including the use of CT-based models, integration with machine learning algorithms, and innovative approaches like combining radiomics with finite element analysis. These studies illustrate how radiomics not only enhances diagnostic accuracy but also contributes to early detection of osteoporosis, fracture risk prediction, and personalized treatment planning. The inclusion of diverse imaging modalities, such as dental panoramic radiographs and DEXA, showcases the versatility of radiomics across different clinical and research settings.

However, the chapter also identified several challenges that must be addressed to fully realize the potential of radiomics in bone health. Variability in imaging protocols, feature extraction methods, and preprocessing techniques poses significant barriers to reproducibility and generalizability. Additionally, the integration of radiomics into clinical workflows requires validated models and streamlined processes to ensure practical implementation without increasing the burden on healthcare providers.

By synthesizing the literature, this chapter has shown that radiomics offers a transformative approach to understanding and managing bone health. Its ability to provide a detailed, quantitative analysis of bone microarchitecture and mechanical properties represents a paradigm shift in osteoporosis research and diagnosis. The literature reviewed supports the central thesis that radiomics holds the potential to overcome the limitations of traditional imaging and non-imaging methods.

Moving forward, future research should prioritize the standardization of radiomics workflows, the development of robust predictive models, and the integration of artificial intelligence to enhance the clinical applicability of radiomics. By addressing these challenges, radiomics can become an indis-

pensable tool for advancing bone health assessments and improving patient outcomes.

This chapter's detailed review of the literature underscores the significance of radiomics in bone health research while providing a foundation for the subsequent chapters that will delve deeper into its methodologies, applications, and clinical implications. The focus on bone is not only warranted but essential, given its importance in advancing personalized and predictive medicine.

Direct Techniques		
Imaging		Non Imaging
Ionizing		
X-Ray	SXA DXA	QUS GA NA CACC
CT	QCT HRpQCT pQCT Dual Energy pQCT CBCT	
Non-Ionizing		
US	US REMS	
MR	MRI HR-MRI NMR	
Indirect Techniques		
TBS		
BSI		
QUI		

Figure 2.1: Summary of the Six Principal Categories of Direct and Indirect Techniques for Assessing Bone Quality and Quantity.

RX = X-ray; GA = Gravimetric Analysis; SXA = Single-energy X-ray Absorptiometry; CACC = Chemical Analysis of Crosslink Collagen; DXA = Dual-energy X-ray Absorptiometry; MRI = Magnetic Resonance Imaging; CT = Computed Tomography; HR-MRI = High-resolution MRI; QCT = Quantitative CT; NMR = Nuclear Magnetic Resonance Imaging; HR-pQCT = High-resolution peripheral QCT; REMS = Radiofrequency US Multi-Spectrometry; CBCT = Cone Beam CT; QUS = Quantitative Ultrasound; pQCT = Peripheral QCT; TBS = Trabecular Bone Score; NA = Neutron Activation; BSI = Bone Strength Index; QUI = Quantitative Ultrasound Index.

Chapter 3

Preclinical Studies

This chapter investigates the potential of radiomic analysis in bone health assessment through two preclinical studies that we conducted. The first study aimed to establish a correlation between radiomic features extracted from a phantom and actual bone tissue, validating the use of bone as a reliable model for human applications. Building on this, the second study explored the relationship between radiomic features derived from CBCT images and the mechanical properties of bone, such as stiffness and ultimate load. Together, these preclinical investigations have provided crucial insights that guided the subsequent direction of our work, emphasizing the potential of radiomics to advance bone strength assessment and clinical applications.

3.1 Introduction

The structural integrity and mechanical properties of bones are critical parameters in the investigation of bone pathologies, including osteoporosis and other degenerative diseases [12]. Traditionally, assessments of bone health have been heavily reliant on BMD measurements obtained through DEXA. However, the limitations of BMD as a singular metric have become increasingly evident, especially with the growing understanding that bone strength is not solely determined by mineral content but also by its microarchitectural complexity. Recent advancements in imaging technologies and computational analysis, such as radiomics, have prompted a paradigm shift towards

more comprehensive evaluations of bone quality and strength. Radiomics, as previously discussed, facilitates the extraction of quantitative imaging features that go beyond conventional assessments, providing a deeper understanding of the structural organization, heterogeneity, and mechanical behavior of bone. The preclinical studies presented in this chapter significantly contribute to the burgeoning field of radiomics in bone health research. These studies were designed as investigative explorations to evaluate the feasibility of applying radiomics to this domain and lay the groundwork for a deeper exploration of this area of research. The first study focuses on the extraction and correlation of radiomic features between a bone-like phantom and actual bone tissue, not merely to validate the utility of the phantom but to demonstrate that these techniques, though still in a primordial stage, offer the potential to bridge the gap from bone research to human applications. The second study delves deeper into linking structural parameters derived from CBCT images with mechanical properties obtained through physical testing on porcine bone samples. While the use of porcine bones may initially raise questions about the applicability of the findings to human bone research, these samples were chosen for their well-documented structural and compositional similarities to human bone [62]. Porcine bones offer a practical and ethical model for preclinical investigations, enabling the controlled testing of hypotheses and the validation of methodologies before transitioning to human studies. Despite the inherent limitations of using porcine models, the results obtained from these studies provide valuable insights into the feasibility of applying radiomic techniques to the analysis of bone microarchitecture and mechanical properties. One key limitation lies in the anatomical and compositional differences between porcine and human bones, such as variations in trabecular structure, mineral content, and overall size, which may impact the direct translatability of findings to human applications. Additionally, the smaller dimensions of porcine bones compared to human femurs could influence the accuracy of certain radiomic features or biomechanical measurements, particularly when scaled to human-sized structures. Nevertheless, radiomic features extracted from porcine bones demonstrated consistent correlations with mechanical properties, such as stiffness and elastic modulus, aligning with known biomechanical behaviors observed in human bone. These findings suggest that, while not a perfect substitute, porcine models offer a practical and ethical alternative for preclinical research. The use of such models ensures a standardized approach to

testing, minimizing variability that is often challenging to control with human specimens due to differences in age, pathology, and other confounding factors. To address these limitations, future studies should consider validating the findings on human samples or employing advanced scaling techniques to better extrapolate results from porcine to human bone. These efforts will enhance the translatability of radiomic techniques and further establish their potential as a bridge between imaging-derived data and biomechanical outcomes, even in the context of preclinical research. This chapter will provide a detailed examination of the methodologies employed in both studies, along with a critical analysis of their findings and contributions to the evolving landscape of bone health assessment. These investigations not only represent essential steps toward the integration of radiomics in both preclinical research and clinical practice but also lay the groundwork for the continued development of this project [119]. By building on these initial findings, this research will push forward the application of radiomics in bone health, advancing our understanding of bone pathology beyond the confines of traditional imaging metrics and paving the way for future innovations [60].

3.2 Radiomic Feature Extraction: Bone vs. Phantom

The first preclinical study centers on the development of a phantom specifically designed to simulate the attenuation that would be observed in a human leg under CBCT imaging. Phantoms are essential tools in medical research, providing a controlled environment for experiments and allowing researchers to validate imaging techniques before applying them to human subjects. In this case, the phantom was created to mimic human conditions, with the goal of determining whether the radiomic features extracted from bone tissue could be correlated with those obtained from the phantom. If such a correlation exists, it would validate the relevance of studying bone, as the findings could be extrapolated to human applications. This would support the use of bone as a proxy for human bone quality assessment, providing a foundation for further investigation. The phantom shown in Fig.3.1 was designed with high fidelity to simulate both bone and soft tissue attenuation, Its development was based on a meticulous process aimed at achieving a model that closely mimics the structural and radiological characteristics of a human thigh. Porcine femurs were chosen as the central component due to

their structural and dimensional similarities to human bones, despite their overall smaller size. The average length of the porcine femur used was approximately 250 mm, with a neck diameter ranging between 35 mm and 45 mm. To recreate a phantom representative of a human thigh, the diameter of the phantom was calculated to be approximately 140 mm, incorporating multiple layers to simulate the attenuation properties of soft tissues, muscle, and skin. The process began with the careful selection and preparation of porcine femurs, which were then wrapped with layers of pork meat to simulate the attenuation effects of muscle and adipose tissue. This wrapping process required precision to ensure uniformity and compactness, minimizing the presence of air bubbles, which could otherwise distort the imaging results. The meat was arranged in a compact layer, using a plane to flatten it before wrapping it around the femur. The wrapped femur was then covered with a layer of pork rind (cotenna), cut precisely to match the desired circumference of the phantom without overlapping. To proportionally replicate a human thigh with a Body Mass Index (BMI) between 18.5 kg/m^2 and 24.99 kg/m^2 (indicative of a normoweight individual), a specific ratio was used. The calculation was based on the circumference of a human thigh (approximately 55 cm) and the diameter of a human femoral neck (5 cm), compared to the dimensions of the porcine femur (4 cm). Using the ratio:

$$\frac{55\,\mathrm{cm}}{5\,\mathrm{cm}} = \frac{x}{4\,\mathrm{cm}} \implies x = \frac{4 \times 55}{5} = 44\,\mathrm{cm},$$

the calculated circumference of the phantom was 44 cm, corresponding to a diameter of 14 cm when divided by π.

The phantom design also accounted for the radiological attenuation characteristics of the components. According to the Lambert-Beer law, the attenuation of radiation through a material depends on the material's density and thickness. The low-density polyethylene (LDPE) wrap, with an attenuation coefficient $\mu = 0.2\,\mathrm{cm}^{-1}$ at an energy of 95 keV, was used to ensure a uniform outer layer and to provide the desired attenuation properties. The preparation was completed within 3 to 24 hours post-mortem, during the rigor mortis phase, to maintain realistic muscle rigidity and prevent decomposition-related changes. The overall length of the phantom was approximately 300 mm, with an additional 50 mm distributed across the epiphyses to simulate the natural proportions of a human thigh. This detailed process ensured that the phantom closely approximated the dimensions and radiological characteristics of a human thigh, providing a reliable and repro-

ducible model for the study of radiomic feature extraction and bone quality assessment. By incorporating realistic attenuation properties and structural considerations, this phantom design lays the foundation for the validation of radiomics techniques in preclinical studies and their future application to human research. Once realized underwent CBCT scanning at Imaginalis Srl to generate a set of images from which radiomic features could be extracted.

The same process was applied to the bone itself, as shown in Fig. 3.2:

The analysis utilized well-established radiomic feature matrices, including:

- Grey Level Co-occurrence Matrix (GLCM): Used to capture textural features such as contrast, energy, homogeneity, and correlation, which reflect the spatial relationships between pixels of different intensities [56].

The following table 3.1 summarizes the 24 descriptors derived from the Gray-Level Co-occurrence Matrix (GLCM). Below are the definitions of the key indices used in the equations:

- i, j: Gray-level intensities of pixel pairs. - $p(i, j)$: Normalized value of the GLCM at position (i, j), representing the probability of co-occurrence of intensity i with j. - N_g: Number of gray levels in the image. - μ_i, μ_j: Mean gray-level intensities for rows and columns, respectively. - σ_i, σ_j: Standard deviations of gray-level intensities for rows and columns, respectively. - Î≫ max : The largest eigenvalue of the normalized GLCM-derived matrices.

Feature Name	Definition	Equation
Auto correlation	A measure of the magnitude of the fineness or coarseness of the texture.	$\sum_{i=1}^{N_g} \sum_{j=1}^{N_g} i \cdot j \cdot p(i, j)$
Joint Average	Returns the mean intensity of the gray-level distribution of pixels.	$\sum_{i=1}^{N_g} \sum_{j=1}^{N_g} i \cdot p(i, j)$
Cluster Prominence	A measure of the asymmetry of the GLCM. Higher values imply greater asymmetry.	$\sum_{i=1}^{N_g} \sum_{j=1}^{N_g} (i + j - \mu_x - \mu_y)^4 \cdot p(i, j)$

Cluster Shade	A measure of the asymmetry and uniformity of the GLCM.	$\sum_{i=1}^{N_g} \sum_{j=1}^{N_g} (i + j - \mu_x - \mu_y)^3 \cdot p(i,j)$
Cluster Tendency	A measure of voxel clustering with similar gray-level values.	$\sum_{i=1}^{N_g} \sum_{j=1}^{N_g} (i + j - \mu_x - \mu_y)^2 \cdot p(i,j)$
Contrast	A measure of local intensity variation, emphasizing values far from the diagonal.	$\sum_{i=1}^{N_g} \sum_{j=1}^{N_g} (i-j)^2 \cdot p(i,j)$
Correlation	Shows the linear dependence of gray-level values on their respective voxel in the GLCM.	$\frac{\sum_{i=1}^{N_g} \sum_{j=1}^{N_g} (i-\mu_i)(j-\mu_j) \cdot p(i,j)}{\sigma_i \cdot \sigma_j}$
Difference Average	Measures the relationship between similar and different intensity pairs.	$\sum_{k=0}^{N_g-1} k \cdot p_d(k)$
Difference Entropy	A measure of randomness in intensity differences.	$-\sum_{k=0}^{N_g-1} p_d(k) \cdot \log p_d(k)$
Difference Variance	A measure of heterogeneity, weighting pairs with higher differences.	$\sum_{k=0}^{N_g-1} (k - \mu_d)^2 \cdot p_d(k)$
Joint Energy	A measure of homogeneous patterns in the image.	$\sum_{i=1}^{N_g} \sum_{j=1}^{N_g} p(i,j)^2$
Joint Entropy	A measure of randomness in neighboring pixel intensities.	$-\sum_{i=1}^{N_g} \sum_{j=1}^{N_g} p(i,j) \cdot \log p(i,j)$
IMC 1	Correlation between the probability distributions of i and j.	$\frac{HXY - HXY1}{\max(HX, HY)}$
IMC 2	Another measure of correlation between i and j.	$\sqrt{1 - \exp(-2(HXY2 - HXY))}$

IDM (Inverse Difference Moment)	A measure of local homogeneity.	$\sum_{i=1}^{N_g} \sum_{j=1}^{N_g} \frac{p(i,j)}{1+(i-j)^2}$
MCC (Maximal Correlation Coefficient)	A measure of texture complexity.	$\sqrt{\lambda_{\max}}$
IDMN (Normalized IDM)	Normalized version of IDM.	[Add specific formula if available]
Inverse Difference	Another measure of local homogeneity.	$\sum_{i=1}^{N_g} \sum_{j=1}^{N_g} \frac{p(i,j)}{1+|i-j|}$
IDN (Normalized Inverse Difference)	Normalized local homogeneity measure.	$\frac{\sum_{j=1}^{N_d}\left(\sum_{i=1}^{N_g} p(i,j)\right)^2}{N_p^2}$
Inverse Variance	Emphasizes pairs with low variance (more homogeneity).	$\sum_{i=1}^{N_g} \sum_{j=1}^{N_g} \frac{p(i,j)}{(i-j)^2}$
Maximum Probability	Occurrence of the most predominant intensity pair.	$\max(p(i,j))$
Sum Average	Relationship between pairs with low and high intensities.	$\sum_{k=2}^{2N_g} k \cdot p_s(k)$
Sum Entropy	Sum of neighborhood intensity differences.	$-\sum_{k=2}^{2N_g} p_s(k) \cdot \log p_s(k)$
Sum of Squares	Distribution of neighboring intensity pairs relative to the mean.	$\sum_{i=1}^{N_g} \sum_{j=1}^{N_g} (i-\mu)^2 \cdot p(i,j)$

Table 3.1: GLCM Features: Definitions and Equations

- Grey-Level Run Length Matrix (GLRLM): Measures the length of consecutive pixels with the same gray-level value in a particular direction,

providing insight into the homogeneity and variability within the bone microarchitecture [46].

The following table 3.2 summarizes the 16 descriptors derived from the Gray-Level Run Length Matrix (GLRLM). Below are the definitions of the key indices used in the equations:

- i, j: Gray-level intensity and run length, respectively. - $p(i, j)$: Value of the GLRLM at position (i, j), representing the number of occurrences of run length j for gray level i. - N_g: Number of gray levels in the image. - N_r: Maximum run length in the image. - N_p: Total number of voxels in the region of interest (ROI).

Feature Name	Definition	Equation
Short Run Emphasis (SRE)	A measure of the distribution of short runs, with higher values indicating finer textures.	$\frac{1}{N_p} \sum_{i=1}^{N_g} \sum_{j=1}^{N_r} \frac{p(i,j)}{j^2}$
Long Run Emphasis (LRE)	A measure of the distribution of long runs, with higher values indicating coarser textures.	$\frac{1}{N_p} \sum_{i=1}^{N_g} \sum_{j=1}^{N_r} p(i,j) \cdot j^2$
Gray Level Non-Uniformity (GLN)	Measures the similarity of gray-level intensities, with lower values indicating higher similarity.	$\frac{1}{N_p} \sum_{i=1}^{N_g} \left(\sum_{j=1}^{N_r} p(i,j) \right)^2$
Gray Level Non-Uniformity Normalized (GLNN)	Normalized version of GLN, measuring gray-level similarity.	$\frac{\sum_{i=1}^{N_g} \left(\sum_{j=1}^{N_r} p(i,j) \right)^2}{N_p^2}$
Run Length Non-Uniformity (RLN)	Measures the similarity of run lengths, with lower values indicating higher similarity.	$\frac{1}{N_p} \sum_{j=1}^{N_r} \left(\sum_{i=1}^{N_g} p(i,j) \right)^2$

Run Length Non-Uniformity Normalized (RLNN)	Normalized version of RLN, measuring run length similarity.	$\frac{\sum_{j=1}^{N_r}\left(\sum_{i=1}^{N_g} p(i,j)\right)^2}{N_p^2}$
Run Percentage (RP)	Measures the coarseness of texture as the ratio of the number of runs to the total number of voxels.	$\frac{N_r}{N_p}$
Gray Level Variance (GLV)	Measures the variance of gray-level intensities across runs.	$\frac{1}{N_p}\sum_{i=1}^{N_g}\sum_{j=1}^{N_r}(i-\mu_g)^2 \cdot p(i,j)$
Run Variance (RV)	Measures the variance of run lengths.	$\frac{1}{N_p}\sum_{i=1}^{N_g}\sum_{j=1}^{N_r}(j-\mu_r)^2 \cdot p(i,j)$
Run Entropy (RE)	Measures the uncertainty or randomness in the distribution of runs and gray levels.	$-\sum_{i=1}^{N_g}\sum_{j=1}^{N_r} p(i,j) \cdot \log(p(i,j))$
Low Gray Level Run Emphasis (LGLRE)	Measures the distribution of low gray-level values, with higher values indicating greater concentration of low-intensity values.	$\frac{1}{N_p}\sum_{i=1}^{N_g}\sum_{j=1}^{N_r}\frac{p(i,j)}{i^2}$
High Gray Level Run Emphasis (HGLRE)	Measures the distribution of high gray-level values, with higher values indicating greater concentration of high-intensity values.	$\frac{1}{N_p}\sum_{i=1}^{N_g}\sum_{j=1}^{N_r} p(i,j)\cdot i^2$
Short Run Low Gray Level Emphasis (SRLGLE)	Measures the joint distribution of short runs with low gray-level values.	$\frac{1}{N_p}\sum_{i=1}^{N_g}\sum_{j=1}^{N_r}\frac{p(i,j)}{i^2\cdot j^2}$

Short Run High Gray Level Emphasis (SRHGLE)	Measures the joint distribution of short runs with high gray-level values.	$\frac{1}{N_p} \sum_{i=1}^{N_g} \sum_{j=1}^{N_r} \frac{i^2 \cdot p(i,j)}{j^2}$
Long Run Low Gray Level Emphasis (LRLGLE)	Measures the joint distribution of long runs with low gray-level values.	$\frac{1}{N_p} \sum_{i=1}^{N_g} \sum_{j=1}^{N_r} \frac{p(i,j) \cdot j^2}{i^2}$
Long Run High Gray Level Emphasis (LRHGLE)	Measures the joint distribution of long runs with high gray-level values.	$\frac{1}{N_p} \sum_{i=1}^{N_g} \sum_{j=1}^{N_r} p(i,j) \cdot i^2 \cdot j^2$

Table 3.2: GLRLM Features: Definitions and Equations

- Grey-Level Size Zone Matrix (GLSZM): Quantifies the size of homogeneous zones of pixels that share the same gray-level value, offering information about structural uniformity and potential heterogeneity in bone density [149].

The following table 3.3 summarizes the 16 descriptors derived from the Gray Level Size Zone Matrix (GLSZM). Below are the definitions of the key indices used in the equations:

- i, j: Gray-level intensity and zone size, respectively. - $p(i,j)$: Value of the GLSZM at position (i,j), representing the number of zones of size j for gray level i. - N_g: Number of gray levels in the image. - N_z: Maximum zone size in the image. - N_p: Total number of voxels in the region of interest (ROI). - N_s: Total number of zones in the image.

Feature Name	Definition	Equation

Small Area Emphasis (SAE)	A measure of the distribution of small zones, with higher values indicating finer textures.	$\frac{1}{N_s} \sum_{i=1}^{N_g} \sum_{j=1}^{N_z} \frac{p(i,j)}{j^2}$
Large Area Emphasis (LAE)	A measure of the distribution of large zones, with higher values indicating coarser textures.	$\frac{1}{N_s} \sum_{i=1}^{N_g} \sum_{j=1}^{N_z} p(i,j) \cdot j^2$
Gray Level Non-Uniformity (GLN)	Measures the variability of gray-level intensities, with lower values indicating greater homogeneity.	$\frac{1}{N_s} \sum_{i=1}^{N_g} \left(\sum_{j=1}^{N_z} p(i,j) \right)^2$
Gray Level Non-Uniformity Normalized (GLNN)	Normalized version of GLN, measuring gray-level similarity.	$\frac{\sum_{i=1}^{N_g} \left(\sum_{j=1}^{N_z} p(i,j) \right)^2}{N_s^2}$
Size-Zone Non-Uniformity (SZN)	Measures the variability of zone sizes, with lower values indicating greater homogeneity.	$\frac{1}{N_s} \sum_{j=1}^{N_z} \left(\sum_{i=1}^{N_g} p(i,j) \right)^2$
Size-Zone Non-Uniformity Normalized (SZNN)	Normalized version of SZN, measuring zone size similarity.	$\frac{\sum_{j=1}^{N_z} \left(\sum_{i=1}^{N_g} p(i,j) \right)^2}{N_s^2}$
Zone Percentage (ZP)	Measures the coarseness of the texture as the ratio of the number of zones to the total number of voxels.	$\frac{N_s}{N_p}$
Gray Level Variance (GLV)	Measures the variance of gray-level intensities across zones.	$\frac{1}{N_s} \sum_{i=1}^{N_g} \sum_{j=1}^{N_z} (i - \mu_g)^2 \cdot p(i,j)$

Zone Variance (ZV)	Measures the variance of zone sizes.	$\frac{1}{N_s} \sum_{i=1}^{N_g} \sum_{j=1}^{N_z} (j - \mu_z)^2 \cdot p(i,j)$
Zone Entropy (ZE)	Measures the uncertainty or randomness in the distribution of zone sizes and gray levels.	$- \sum_{i=1}^{N_g} \sum_{j=1}^{N_z} p(i,j) \cdot \log(p(i,j))$
Low Gray Level Zone Emphasis (LGLZE)	Measures the distribution of low gray-level zones, with higher values indicating a greater proportion of lower intensity levels.	$\frac{1}{N_s} \sum_{i=1}^{N_g} \sum_{j=1}^{N_z} \frac{p(i,j)}{i^2}$
High Gray Level Zone Emphasis (HGLZE)	Measures the distribution of high gray-level zones, with higher values indicating a greater proportion of higher intensity levels.	$\frac{1}{N_s} \sum_{i=1}^{N_g} \sum_{j=1}^{N_z} p(i,j) \cdot i^2$
Small Area Low Gray Level Emphasis (SALGLE)	Measures the joint distribution of small zones with low gray-level values.	$\frac{1}{N_s} \sum_{i=1}^{N_g} \sum_{j=1}^{N_z} \frac{p(i,j)}{i^2 \cdot j^2}$
Small Area High Gray Level Emphasis (SAHGLE)	Measures the joint distribution of small zones with high gray-level values.	$\frac{1}{N_s} \sum_{i=1}^{N_g} \sum_{j=1}^{N_z} \frac{i^2 \cdot p(i,j)}{j^2}$
Large Area Low Gray Level Emphasis (LALGLE)	Measures the joint distribution of large zones with low gray-level values.	$\frac{1}{N_s} \sum_{i=1}^{N_g} \sum_{j=1}^{N_z} \frac{p(i,j) \cdot j^2}{i^2}$
Large Area High Gray Level Emphasis (LAHGLE)	Measures the joint distribution of large zones with high gray-level values.	$\frac{1}{N_s} \sum_{i=1}^{N_g} \sum_{j=1}^{N_z} p(i,j) \cdot i^2 \cdot j^2$

Table 3.3: GLSZM Features: Definitions and Equations

- Grey-Level Dependence Matrix (GLDM): Describes the dependence between pixels at varying distances, providing data on the complexity and integrity of the bone structure [149].

The following table 3.4 summarizes the 14 descriptors derived from the Gray Level Dependence Matrix (GLDM). Below are the definitions of the key indices used in the equations:

- i, j: Gray-level intensity and dependence size, respectively. - $p(i, j)$: Value of the GLDM at position (i, j), representing the number of occurrences of dependence size j for gray level i. - N_g: Number of gray levels in the image. - N_d: Maximum dependence size in the image. - N_p: Total number of voxels in the region of interest (ROI). - μ_g, μ_d: Mean gray level and dependence size, respectively.

Feature Name	Definition	Equation
Small Dependence Emphasis (SDE)	A measure of the distribution of small dependencies, with higher values indicating less homogeneous textures.	$\frac{1}{N_p} \sum_{i=1}^{N_g} \sum_{j=1}^{N_d} \frac{p(i,j)}{j^2}$
Large Dependence Emphasis (LDE)	A measure of the distribution of large dependencies, with higher values indicating more homogeneous textures.	$\frac{1}{N_p} \sum_{i=1}^{N_g} \sum_{j=1}^{N_d} p(i,j) \cdot j^2$
Gray Level Non-Uniformity (GLN)	Measures the similarity of gray-level intensities, with lower values indicating greater similarity.	$\frac{1}{N_p} \sum_{i=1}^{N_g} \left(\sum_{j=1}^{N_d} p(i,j) \right)^2$

Dependence Non-Uniformity (DN)	Measures the similarity of dependencies across the image, with lower values indicating greater homogeneity.	$\frac{1}{N_p} \sum_{j=1}^{N_d} \left(\sum_{i=1}^{N_g} p(i,j) \right)^2$
Dependence Non-Uniformity Normalized (DNN)	Normalized version of DN, measuring dependency similarity.	$\frac{\sum_{j=1}^{N_d} \left(\sum_{i=1}^{N_g} p(i,j) \right)^2}{N_p^2}$
Gray Level Variance (GLV)	Measures the variance of gray-level intensities across dependencies.	$\frac{1}{N_p} \sum_{i=1}^{N_g} \sum_{j=1}^{N_d} (i - \mu_g)^2 \cdot p(i,j)$
Dependence Variance (DV)	Measures the variance of dependence sizes.	$\frac{1}{N_p} \sum_{i=1}^{N_g} \sum_{j=1}^{N_d} (j - \mu_d)^2 \cdot p(i,j)$
Dependence Entropy (DE)	Measures randomness or uncertainty in the spatial dependencies of pixels with the same gray level.	$- \sum_{i=1}^{N_g} \sum_{j=1}^{N_d} p(i,j) \cdot \log(p(i,j))$
Low Gray Level Emphasis (LGLE)	Measures the distribution of low gray-level values, with higher values indicating a greater concentration of low-intensity values.	$\frac{1}{N_p} \sum_{i=1}^{N_g} \sum_{j=1}^{N_d} \frac{p(i,j)}{i^2}$
High Gray Level Emphasis (HGLE)	Measures the distribution of high gray-level values, with higher values indicating a greater concentration of high-intensity values.	$\frac{1}{N_p} \sum_{i=1}^{N_g} \sum_{j=1}^{N_d} p(i,j) \cdot i^2$

Small Dependence Low Gray Level Emphasis (SDL-GLE)	Measures the joint distribution of small dependencies with low gray-level values.	$\frac{1}{N_p} \sum_{i=1}^{N_g} \sum_{j=1}^{N_d} \frac{p(i,j)}{i^2 \cdot j^2}$
Small Dependence High Gray Level Emphasis (SD-HGLE)	Measures the joint distribution of small dependencies with high gray-level values.	$\frac{1}{N_p} \sum_{i=1}^{N_g} \sum_{j=1}^{N_d} \frac{i^2 \cdot p(i,j)}{j^2}$
Large Dependence Low Gray Level Emphasis (LDL-GLE)	Measures the joint distribution of large dependencies with low gray-level values.	$\frac{1}{N_p} \sum_{i=1}^{N_g} \sum_{j=1}^{N_d} \frac{p(i,j) \cdot j^2}{i^2}$
Large Dependence High Gray Level Emphasis (LD-HGLE)	Measures the joint distribution of large dependencies with high gray-level values.	$\frac{1}{N_p} \sum_{i=1}^{N_g} \sum_{j=1}^{N_d} p(i,j) \cdot i^2 \cdot j^2$

Table 3.4: GLDM Features: Definitions and Equations

3.2.1   Radiomic Feature Extraction and Correlation

After extracting radiomic features from the phantom, a comparative analysis with features extracted from actual bare bone images was performed. The Spearman correlation analysis revealed that among the 65 parameters analyzed, 12 showed strong positive correlations between the features extracted from the phantom and those from the bare bone with a Spearman correlation coefficient above 0.70 (Fig(3.3). These parameters, derived from different radiomic matrices (GLCM, GLDM, GLSZM, and GLRLM), captured similarities in structural patterns between the two conditions. Features are

reported in 3.5

Feature Name	First Pair Correlation	Second Pair Correlation
Auto-correlation (GLCM)	0.9689180404717375	0.9868642100312484
Joint Average (GLCM)	0.9676207009277318	0.982438539306047
Sum Average (GLCM)	0.9676305009299318	0.982447538306057
High Gray Level Emphasis (GLDM)	0.9699385422103012	0.987030228819814
Large Dependence High Gray Level Emphasis (GLDM)	0.9670246973647906	0.9835756086528626
High Gray Level Run Emphasis (GLRLM)	0.969972664551691	0.9870548563887984
Short Run High Gray Level Emphasis (GLRLM)	0.9700344503627074	0.9872084165248189
High Gray Level Zone Emphasis (GLSZM)	0.9700700757119916	0.9871185983320522

Large Area High Gray Level Emphasis (GLSZM)	0.9683818728717332	0.984917183400951
Small Area High Gray Level Emphasis (GLSZM)	0.9703839606309426	0.9876677448310538

Table 3.5: Correlation values for features between the first and second bone-phantom pairs.

The positive correlations suggest that, despite the presence of surrounding soft tissue in the phantom, key radiomic features remain consistent with those observed in the bare bone. For example, parameters emphasizing high gray-level regions reveal how both the phantom and the bare bone share common structural elements, even if their absolute values differ due to the presence or absence of soft tissue. These correlations highlight areas where the phantom effectively mimicked the mineral density and microstructural heterogeneity of bone. However, no additional validation of the extracted data was conducted, and the sample size remained relatively small. These initial findings suggest that radiomic features extracted from bone tissue can be meaningfully extrapolated to human conditions, making it possible to use bare bone directly in studies, as it shows a strong correlation with the results obtained from the phantom. While the phantom effectively simulates human tissue attenuation, the bare bone offers a closer approximation to actual human bone. This strong correlation justifies the use of bare bone as a valuable tool for radiomic studies, as it provides insights consistent with those derived from the phantom. However, the study also highlighted limitations in the phantom's ability to replicate more intricate trabecular structures, where subtle variations in texture were not as well captured. This reinforces the importance of using bone as the primary model in future studies, with the phantom serving primarily as a supplemental tool rather than the main focus. Although refinements in phantom design could enhance its role in preliminary investigations, bone tissue remains the preferable medium for

advancing radiomic research in bone quality assessment.

3.2.2   Implications for Bone Quality Assessment

The findings from the study have important implications for the field of bone radiomics. The use of phantoms for non-invasive bone quality assessments could reduce the need for human specimens in early-stage research, simplifying experimental setups and allowing for better standardization. It is important to acknowledge the limitations inherent in this study, particularly with regard to the phantom used. The primary goal of this research was to correlate the radiomic features extracted from bone tissue with those extracted from a phantom designed to mimic human tissue attenuation. However, the phantom itself was constructed based on proportional scaling from porcine measurements and human data found in the literature ([8]), without undergoing formal validation. This introduces a level of uncertainty, as the accuracy of this model in fully replicating human tissue properties has not been rigorously tested. Nevertheless, this study served as an essential first step in exploring the potential for radiomics in bone research. The construction of a phantom that approximates human tissue, while imperfect, allowed us to investigate whether the radiomic features derived from bone can be meaningfully correlated with those from a human-like model. If a strong correlation is established, it would provide a solid basis for pursuing more advanced models and eventually transitioning to human applications. While we recognize the limitations of using a phantom that has not been empirically validated, this approach is necessary for initiating the research and testing the feasibility of radiomics in this context. The results of this preliminary study will guide future research, which will aim to validate these findings with human samples and refine the models to ensure their clinical relevance.

3.3   Structural Parameters and Mechanical Testing: Bone Integrity and Strength

The second study took a complementary approach to the first by focusing on the correlation between radiomic features and the mechanical properties of bone. Like the previous study, this one used porcine femurs as bone models and applied CBCT imaging to extract structural parameters that reflect the

bone's morphology and architecture.

The structural parameters extracted from CBCT images included:

- Cortical Bone Thickness: A critical factor in determining the bone's
  resistance to bending and torsional forces. Greater cortical thickness
  is associated with enhanced load-bearing capacity.

- Trabecular Bone Density and Thickness: Trabecular bone plays a cru-
  cial role in distributing mechanical loads, and variations in its thickness
  and density can greatly affect overall bone strength.

- Moment of Inertia (MOI): A measure of an object's resistance to rota-
  tional forces, MOI is directly related to the bone's ability to withstand
  mechanical loads without fracturing. In this study, MOI was calcu-
  lated along the antero-posterior (vertical) and medio-lateral (horizon-
  tal) axes of the cross-sectional area of the cortical bone. These axes
  represent the principal directions relevant for assessing resistance to
  bending forces and overall structural integrity under mechanical load-
  ing.

These structural parameters were extracted using custom Python-based al-
gorithms that automated the processing of CBCT images, allowing for effi-
cient and consistent data extraction. The efficiency of the extraction process
was demonstrated by significantly reducing the processing time: each CBCT
dataset, containing multiple slices, was processed in under 10 minutes using
the algorithm, compared to approximately 2-3 hours required for manual seg-
mentation and analysis. Consistency was ensured through validation steps,
including repeated trials on multiple CBCT datasets. The extracted param-
eters, such as moments of inertia (MOI) along the horizontal (medio-lateral)
and vertical (antero-posterior) axes, exhibited a standard deviation of less
than 5% for repeated measurements, ensuring reproducibility. Additionally,
the algorithm's outputs were cross-validated against manual measurements
performed on a subset of the data, showing a high degree of agreement, with
Pearson correlation coefficients exceeding 0.95. These results underscore the
reliability and robustness of the automated process for extracting structural
parameters efficiently and consistently from CBCT imaging data.

3.3.1   Mechanical Testing and Correlation

Mechanical tests were conducted on six porcine femurs to derive key mechanical parameters, including stiffness, ultimate load, and yield strength. The setup used for these tests is illustrated in Fig. 3.7. The femurs were subjected to controlled mechanical loading until fracture, generating force-displacement curves for each specimen. These curves reported in Fig. 3.4,3.5 and 3.6 provided essential data on how the bones behaved under stress, offering a direct measurement of their mechanical properties. Statistical analyses were conducted to ensure the reliability of the results. The Bravais-Pearson correlation coefficient was calculated to analyze the relationships between mechanical properties and structural features extracted from CBCT images. The correlations were validated for normality using the Shapiro-Wilk test, confirming that all variables followed a normal distribution (p ¿ 0.05). Significant correlations were identified between the moments of inertia and the ultimate load, with Pearson correlation coefficients of 0.94 for both the horizontal and vertical moments of inertia ($p < 0.005$). Additionally, the cortical bone area demonstrated a positive correlation with ultimate load ($r = 0.88$, $p = 0.02$), underscoring the importance of cortical thickness in mechanical resistance. In contrast, no significant correlations were found between the trabecular bone area and ultimate load. A power analysis was performed prior to the study to ensure sufficient sample size for detecting meaningful correlations between structural and mechanical properties. Based on an expected effect size of 0.8 and a significance level of $\alpha = 0.05$, a minimum of six specimens was determined to achieve a statistical power of 0.8.

3.3.2   Integration of Radiomic Features and Mechanical Parameters

The ultimate goal of this study was to develop a system capable of predicting the mechanical properties of bone based on features extracted from CBCT images. After establishing relationships between fracture parameters using Pearson correlation (a statistical inference method used to analyze the association between quantitative variables) [111] we explored a linear regression approach. Linear regression extends correlation analysis by not only studying relationships between variables but also quantifying the effect of independent variables on a dependent variable. With regression, a model

can be defined to predict the values of a quantitative dependent variable
based on one or more independent variables [102]. In this study, the linear
regression model aimed to predict the fracture load of a bone using indepen-
dent variables as input. The regression model, specifically using moments
of inertia, demonstrated strong performance in predicting the fracture loads
of the tested bones. The model's quality for both the X and Y moments
of inertia is supported by the linear distribution of the samples (shown in
Graphs 3.8 and 3.9) and the determination coefficients, which were 0.86 for
the X moment and 0.85 for the Y moment. This correlation can be explained
by the direct proportionality between moments of inertia and the bending
force applied to the bones. Both the X and Y moments of inertia showed
strong determination coefficients, indicating that the bending moment was
distributed across both axes, making the fracture load dependent on both
moments. Another regression model was developed using the radiomic pa-
rameters of each bone, extracted with 3D Slicer, as independent variables,
with the fracture load as the dependent variable. This model, leveraging the
numerous parameters acquired through bone segmentation, showed a good
ability to predict the fracture load of the bones in the test set with reason-
able accuracy. In this case, the R^2 determination coefficient was 0.62. This
predictive model represents a significant advancement in the field, offering
clinicians the ability to assess bone quality and fracture risk without invasive
mechanical testing. Instead, radiomic features extracted from routine CBCT
scans could provide a comprehensive evaluation of a patient's bone health,
enabling earlier interventions and more personalized treatment strategies for
conditions such as osteoporosis.

3.3.3   Implications on Radiomic approach

The study demonstrated a strong correlation between mechanical properties
such as the ultimate load and structural features like the moments of inertia
(X, Y) and cortical bone area extracted from images. These correlations
suggest that bone characteristics related to strength can be effectively ex-
tracted and used for AI models. However, several aspects need optimization,
including improving the mechanical testing system to ensure repeatable con-
ditions, adjusting the bone's positioning, and eliminating torsional moments
to focus solely on bending resistance. Additionally, the segmentation tech-
nique used for feature extraction needs improvement, as thresholding led to
variability in results. Standardizing the bone's alignment with the image

axes and calculating the principal moments of inertia using Mohr's circle would provide more accurate insights into failure points. Moreover, transitioning from force to stress could allow for the evaluation of bone material strength under different conditions using finite element models. Lastly, volumetric features were not suitable for a linear regression model, likely due to the bone's shape influencing its failure under bending forces. Increasing the number of samples and tests would help refine the model by reducing the impact of outliers.

3.4   Conclusion

These studies provided a comprehensive framework for integrating radiomic feature extraction and mechanical testing in the assessment of bone quality and strength. By validating the use of a phantom in radiomic studies, the first study paved the way for more standardized and reproducible research in bone radiomics. The second study complemented this by demonstrating that radiomic features derived from CBCT can serve as reliable predictors of mechanical properties, offering new possibilities for non-invasive methods of assessing bone strength. Together, these works have significantly contributed to the foundation of this research. They encouraged us to move forward with the belief that radiomic features can be effectively integrated with mechanical testing to provide a more holistic view of bone health, extending beyond traditional BMD measurements. This framework has become the starting point of this work, guiding the direction of the research and providing clear objectives to explore. The implications of these findings for early diagnosis, fracture risk assessment, and personalized treatment plans are profound, and they offer a solid scientific basis for advancing the field of radiomics in bone health assessment. In conclusion, these studies have been instrumental in providing the insights necessary to begin the work presented in the following chapters. The potential for non-invasive, predictive models of bone strength is vast, and this research has the potential to make a significant contribution to the evolving field of radiomics in bone health diagnostics and personalized treatment strategies.
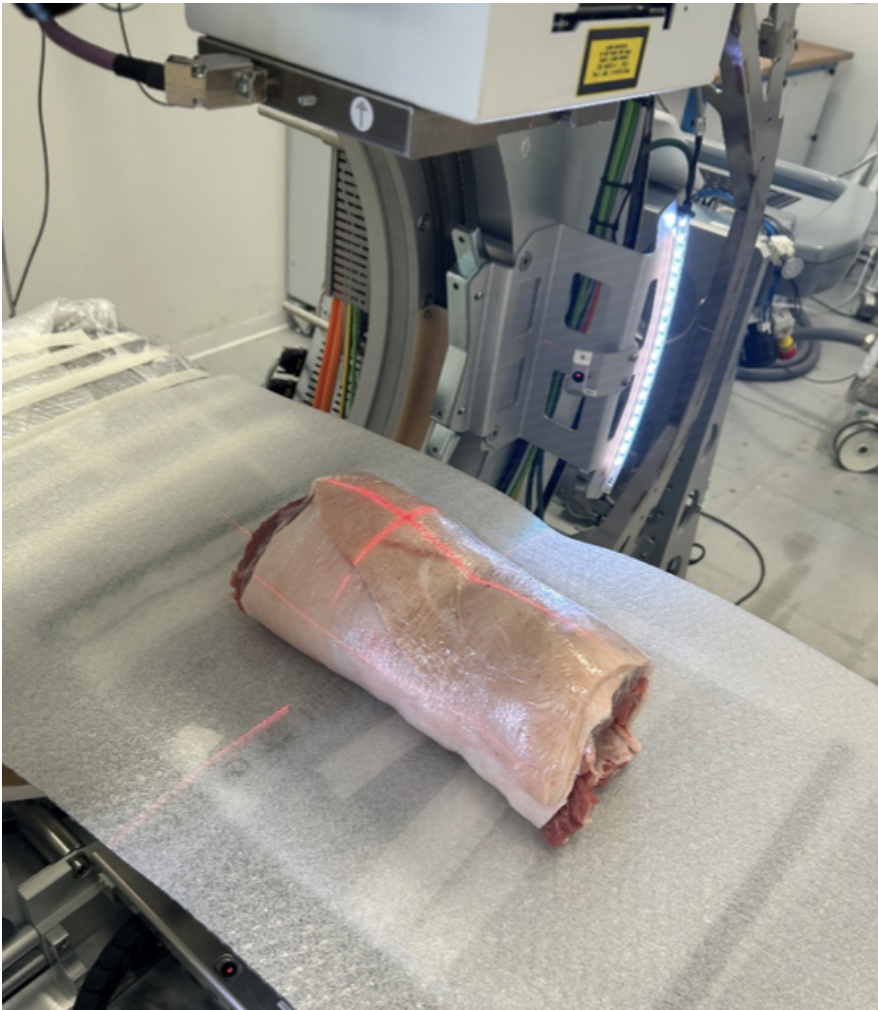
Figure 3.1: CBCT scan of the custom phantom

Figure 3.2: BCT scan of the bare bone
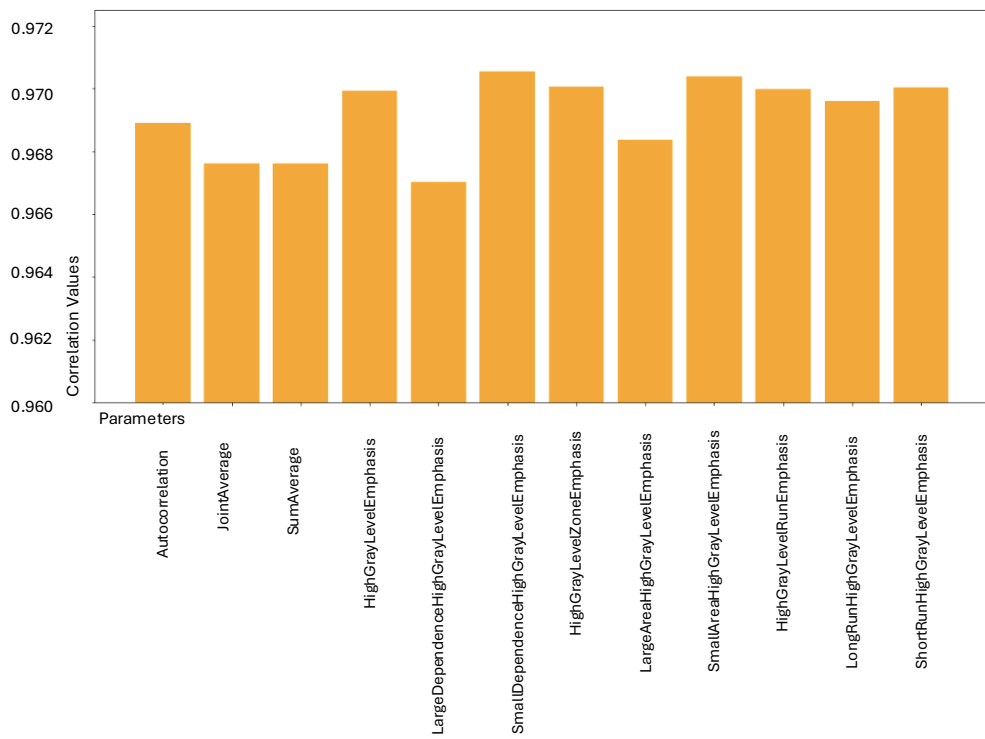
Figure 3.3: Results of Spearman Correlation Analysis

Force-Displacement Curve for Bone 1

Force-Displacement Curve for Bone 2
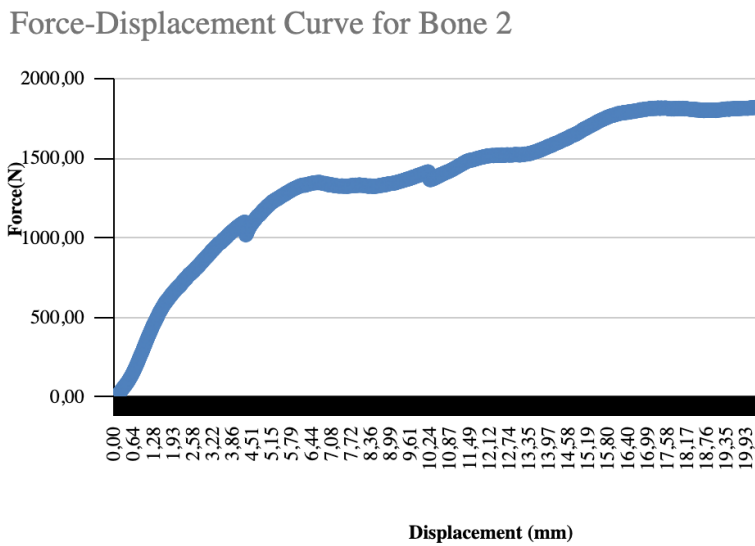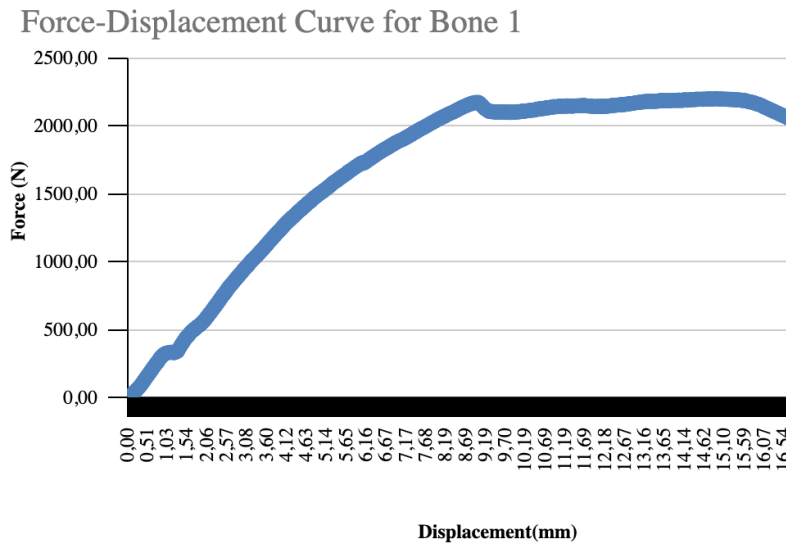
Figure 3.4: Mechanical Testing curves of Bone 1 and Bone 2

Force-Displacement Curve for Bone 3

Force-Displacement Curve for Bone 4
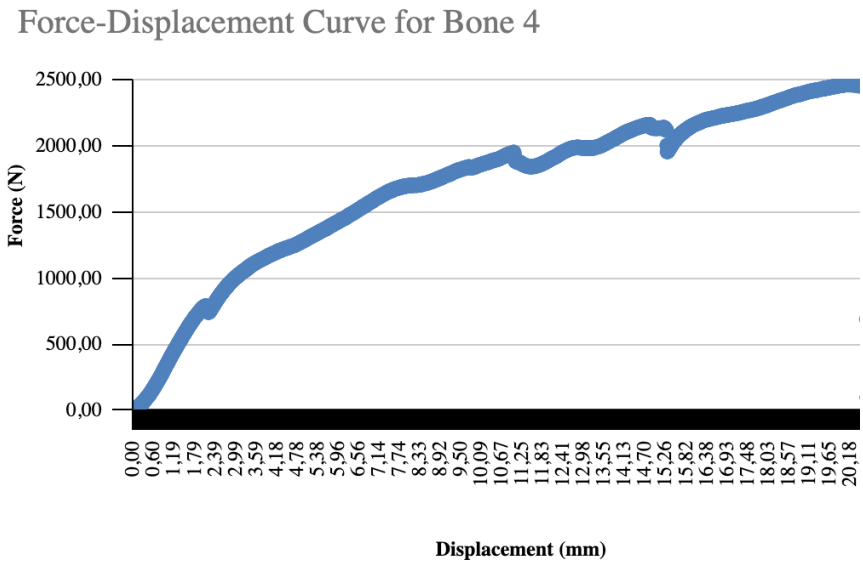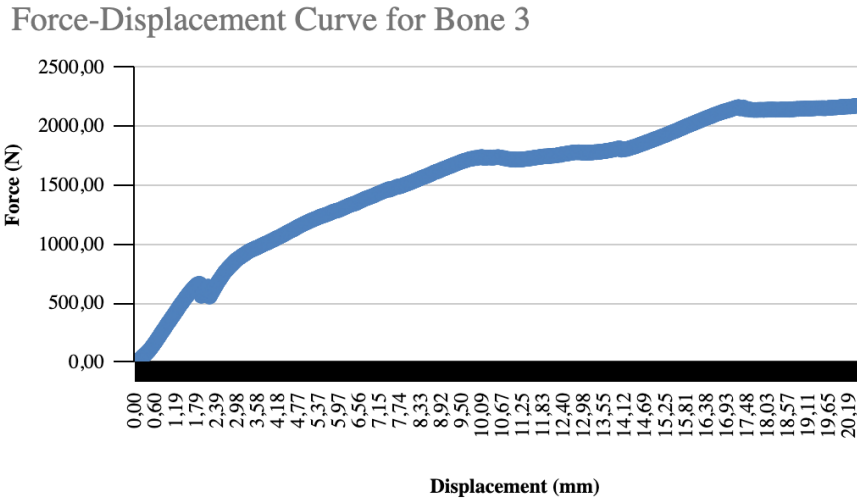
Figure 3.5: Mechanical Testing curves of Bone 3 and Bone 4

Force-Displacement Curve for Bone 5
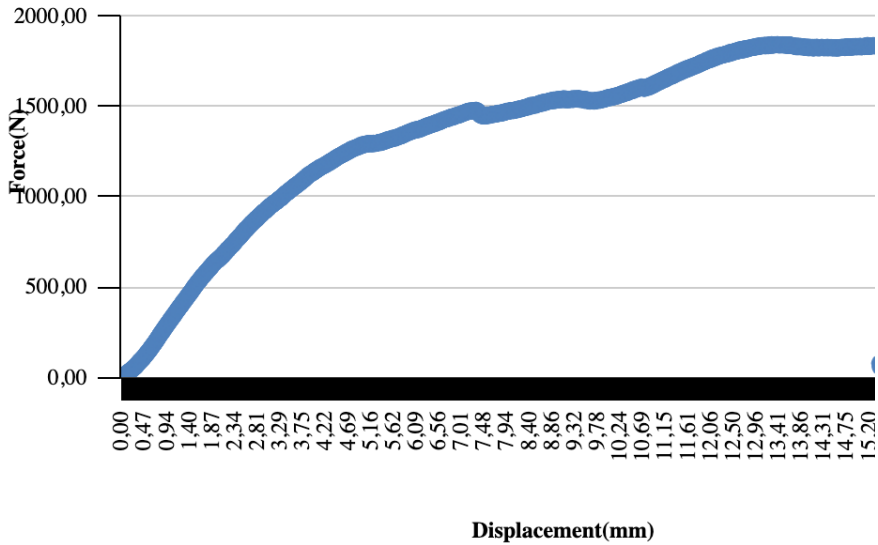
Force-Displacement Curve for Bone 6
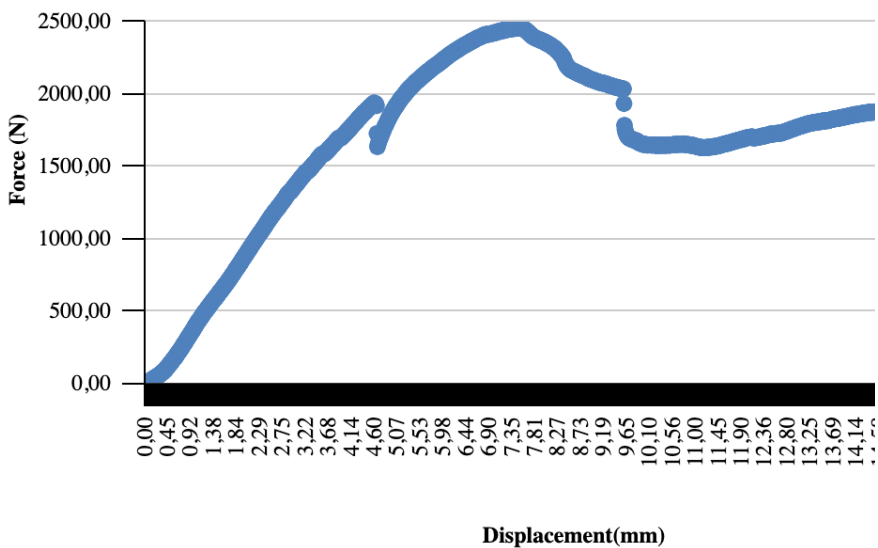
Figure 3.6: Mechanical Testing curves of Bone 5 and Bone 6

Figure 3.7: Mechanical Testing Setup
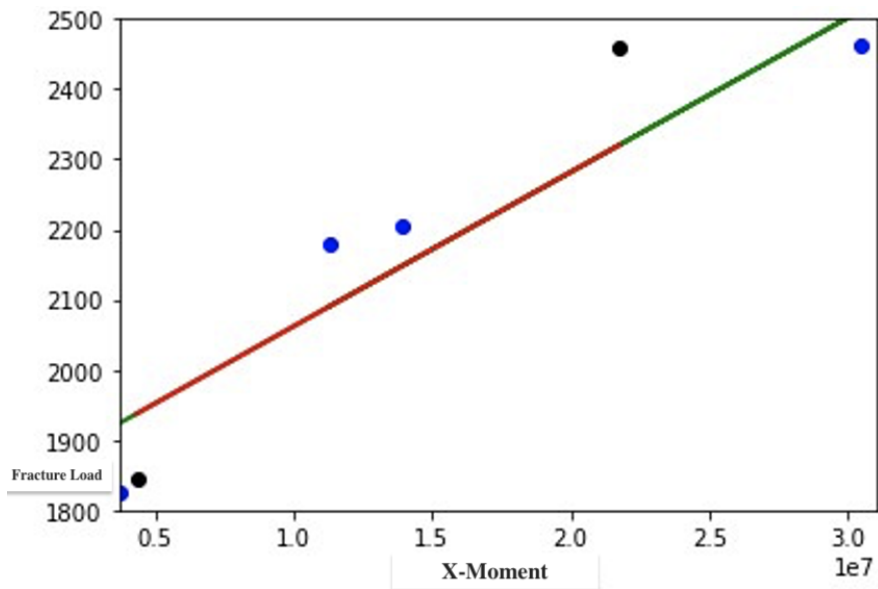
Figure 3.8: Regression line graphs displaying the relationship between Fracture Load (y-axis) and Moment along X. This graphs illustrates the trends and correlations between fracture load and the applied moment.
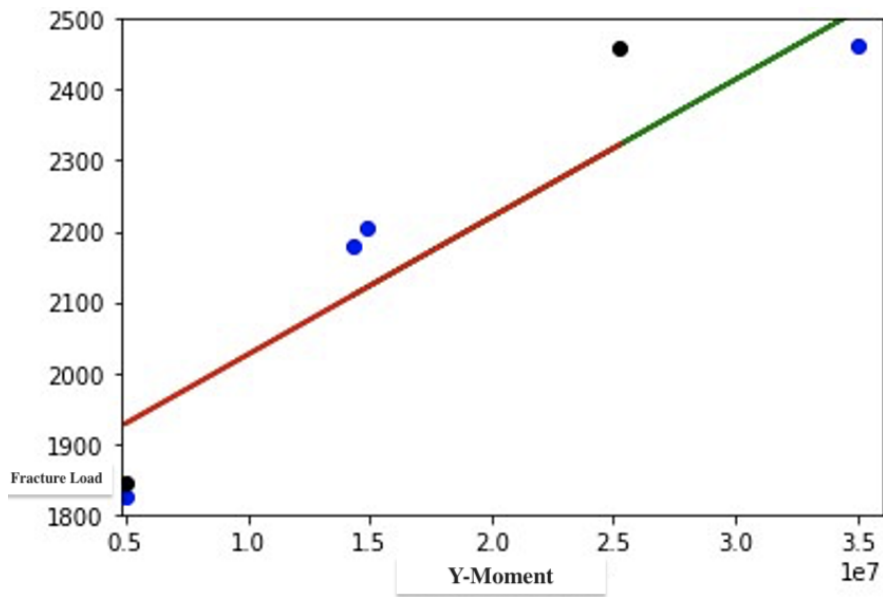
Figure 3.9: Regression line graphs displaying the relationship between Fracture Load (y-axis) and Moment along Y. This graphs illustrates the trends and correlations between fracture load and the applied moment.

Chapter 4

Image Acquisition

This chapter presents the imaging and analysis methods used to assess bone structure and quality in detail. Following image acquisition, various segmentation techniques were explored to isolate regions of interest, with a focus on selecting the most effective approach for this study. In addition to the chosen methods, an overview of alternative acquisition and segmentation techniques is provided, highlighting their respective strengths and limitations. Together, these methods lay a comprehensive foundation for radiomic analysis aimed at understanding bone mechanical properties.

4.1 Introduction

Computed Tomography (CT) provides numerous advantages, making it indispensable in both clinical and research settings for evaluating bone health. Known for its high spatial resolution, CT offers detailed cross-sectional imaging that allows for precise visualization of cortical and trabecular bone, capturing key elements of bone density and structural integrity [14, 23]. This capability is essential for assessing fracture risk and diagnosing conditions such as osteoporosis, where both bone density and the quality of bone microarchitecture are critical factors [99]. Unlike traditional imaging methods like DEXA, which only provides planar measurements, CT enables three-dimensional reconstructions that reveal the complex architecture of bone, offering a more complete view of bone health [81]. Recent advances in imag-

ing technology, such as super-resolution algorithms and micro-CT, have extended CT's utility by enabling high-resolution visualization of bone microarchitecture without added radiation exposure [43]. These advanced techniques are particularly useful for examining the porous, lattice-like structure of trabecular bone, which is central to bone's mechanical performance and fracture resistance [140]. Super-resolution methods applied to standard clinical CT scans enhance image quality, allowing researchers to derive microstructural information from routine imaging that would otherwise require specialized equipment like HR-pQCT or micro-CT [43, 90]. Additionally, CT's compatibility with finite element analysis (FEA) supports biomechanical modeling, where stress and strain simulations can be performed on 3D bone models. Integrating CT data with FEA enables detailed insights into bone strength, stiffness, and fracture susceptibility, thereby enhancing understanding of how changes in bone architecture influence biomechanical properties [157]. This approach is particularly beneficial for studying long bones, such as the femur, where the interplay between cortical and trabecular bone contributes to overall mechanical performance [101]. Furthermore, CT-derived data facilitate predictive modeling in orthopedic care, enabling personalized assessments and treatment planning for conditions such as osteoporosis and post-surgical recovery [13, 112]. The accessibility and versatility of CT imaging, alongside established protocols for bone imaging, position CT as a key modality for comprehensive bone health evaluation. This technology enables both in-depth analysis and data-driven insights into bone health, establishing a solid foundation for understanding fracture risk, diagnosing degenerative conditions, and advancing patient-specific treatment approaches.

4.2 CT Acquisition

In our study, CT scans were performed on three feline specimens at the Hospital of Namur, Belgium, using a Philips Ingenuity Core 64-slice CT scanner as shown in Fig. 4.1. We used feline specimens as they were suitable for the mechanical testing machines we had available. The scanner was selected for its advanced capabilities in both clinical and research applications, allowing for detailed radiomic feature extraction essential for analyzing bone quality and structure. Specific imaging parameters were carefully tailored to balance radiation dose with image clarity, capturing high-resolution data across various bone regions with different densities and structural characteristics.

- Tube current (mA): A variable tube current, ranging from 132 mA to
  156 mA, was applied, utilizing the scanner's dose modulation features
  to ensure optimal radiation balance. Adjusting the current based on
  bone density was crucial for achieving clear imaging, particularly when
  scanning between trabecular-rich epiphyseal regions and denser cortical
  areas of the diaphysis.

- Tube voltage (kV): Tube voltage was adjusted between 79.2 kV and
  126.9 kV, with lower voltages applied to regions with higher trabecular
  bone content, such as the epiphysis, and higher voltages for denser cor-
  tical bone. This setting allowed for optimal X-ray penetration, reduc-
  ing unnecessary radiation exposure in line with the IDose 4 protocol's
  efficient dose management.

- Slice thickness: A slice thickness of 1.25 mm was applied consistently
  across each scan, allowing for high-resolution imaging through both
  trabecular and cortical bone. This thickness was ideal for capturing
  the small structural details necessary for radiomic feature extraction,
  facilitating in-depth mechanical and structural analysis of bone archi-
  tecture.

- Pixel spacing: With a pixel spacing of 0.976 mm x 0.976 mm, the scans
  provided high-resolution data critical for both qualitative and quanti-
  tative assessments of bone properties. This level of detail is essential
  for analyzing microstructural changes in the bone, as even small varia-
  tions in texture or density can significantly impact assessments of bone
  health, especially in conditions such as osteoporosis.

- Rotation time: The gantry rotation time was set to 500 ms, providing
  an optimal balance between rapid scanning and high-quality imaging.
  This fast rotation minimized the potential for movement artifacts, en-
  suring the clarity required for accurate radiomic feature extraction.

- Scan range: Each scan encompassed the entire length of the bones,
  specifically targeting the femur and humerus, and covering both the
  epiphysis and diaphysis. Scanning the full range of these regions al-
  lowed for a comprehensive analysis of structural and biomechanical
  variations across different bone areas, critical for assessing fracture
  risk and informing prosthetic planning.

- IDose 4 Technology: The IDose 4 algorithm, integrated into the Philips Ingenuity Core system, provided real-time dose modulation, significantly reducing radiation exposure while preserving diagnostic image quality. This feature was particularly beneficial in our study, as it enabled high-resolution imaging with a dose-efficient approach suitable for capturing detailed bone structure. By utilizing advanced iterative reconstruction, iDose 4 optimized the signal-to-noise ratio and enhanced spatial resolution, ensuring that even at low radiation doses, the images retained the necessary detail for thorough bone analysis.

4.2.1 Importance for Osteoporosis and Prosthetic Implantation

The selected imaging parameters were tailored to distinguish between the epiphysis and diaphysis, as these regions are impacted differently by conditions like osteoporosis. The epiphysis, which consists primarily of trabecular bone, is particularly vulnerable to bone loss and structural deterioration. In contrast, the diaphysis, composed mostly of cortical bone, generally preserves structural integrity but is more susceptible to fractures when subjected to stress [15]. By capturing these regional differences with high precision, the study aims to enhance the understanding of bone quality and mechanical properties, which is critical in both diagnosing osteoporosis and in the planning of prosthetic implants. Understanding these regional variances allows for more personalized treatment strategies and more accurately designed implants that consider the specific mechanical properties of the target bone region.

4.3 Segmentation

Following image acquisition, the next step involved isolating specific regions within the bone structures for in-depth analysis. This required precise segmentation to accurately define the ROIs or Volumes of Interest (VOIs), laying the groundwork for targeted assessment and radiomic feature extraction.

4.3.1 What is it?

Medical image segmentation is a crucial process in clinical diagnostics, treatment planning, and biomedical research [47]. Segmentation involves dividing

Figure 4.1: CT acquisition

an image into distinct regions that represent various anatomical structures, such as bones, organs, or tissues, allowing for a detailed analysis of the target areas [137]. This process plays an essential role across fields including radiology, oncology, orthopedics, and neurology, enabling clinicians to extract quantitative data that supports disease diagnosis, surgical planning, and personalized treatment decisions. The development of segmentation techniques has paralleled advancements in medical imaging, computational capacity, and the emergence of machine learning [86]. Traditional approaches, such as manual segmentation, where experts delineate structures slice by slice, have evolved toward more sophisticated automated and semi-automated methods, which improve both efficiency and accuracy [57]. This chapter provides an in-depth overview of the most prevalent segmentation techniques in medical imaging, covering manual, fully automated, and semi-automated approaches, with particular focus on the contributions of machine learning and artificial intelligence (AI) to this field [126].

4.3.2   Manual Segmentation

Manual segmentation is one of the most foundational approaches, involving a clinician or radiologist manually outlining the structure of interest in each image slice ([57,85,144]. While this method is both labor-intensive and time-consuming, it remains highly accurate for complex anatomical structures, allowing for the precise delineation of intricate regions. This approach is particularly valuable when automated methods may encounter challenges, such as when anomalies, noise, or low contrast between structures are present. Manual segmentation is often considered the "gold standard" against which automated and semi-automated segmentation techniques are validated [113]. It is also commonly employed in research as a reference standard for training machine learning models [40]. Despite its accuracy, manual segmentation has two primary limitations:

- Time inefficiency: Manually segmenting large image datasets is impractical in high-throughput clinical settings, particularly when rapid decision-making is required [94].

- Inter- and intra-observer variability: The segmentation results can vary between different experts (inter-observer variability) or even when the same expert performs segmentation multiple times (intra-observer variability), leading to inconsistencies in outcomes [38, 139].

4.3.3   Fully Automated Segmentation

Fully automated segmentation techniques seek to eliminate the need for human intervention by employing algorithms to identify and delineate anatomical structures in medical images. These methods frequently leverage computer vision and machine learning algorithms, with Convolutional Neural Networks (CNNs) having notably transformed the field of medical imaging in recent years. Automated segmentation is highly valued in clinical workflows as it allows for rapid, consistent, and scalable analysis of large datasets [86]. CNN-based models can be trained on extensive annotated datasets, enabling them to recognize underlying features of anatomical structures across various imaging modalities such as CT, MRI, and ultrasound. Some prominent automated segmentation approaches include:

- U-Net architecture: A CNN model that has become a standard in medical image segmentation due to its effectiveness with small datasets

while achieving high accuracy [126]. U-Net comprises a contracting path that captures contextual information and a symmetrical expanding path that supports precise localization.

- DeepLab: This CNN-based model employs atrous convolutions to capture multi-scale context and improve boundary detection in medical images [26].

- Fully Convolutional Networks (FCNs): An extension of CNNs, FCNs classify each pixel within an image, making them well-suited for segmentation tasks. They are especially effective in segmenting well-defined structures such as bones or organs in CT or MRI images [87].

Despite the remarkable performance of these models, fully automated segmentation techniques are still challenged by variability in image quality, presence of noise, artifacts, and the need for large annotated datasets to train the models effectively [100]. Consequently, fully automated methods are often supplemented by manual or semi-automated approaches to achieve the highest levels of accuracy in clinical practice.

4.3.4   Semi-Automatic Segmentation

Semi-automatic segmentation techniques integrate user input with automated processes to enhance both the efficiency and accuracy of segmentation tasks [96,170]. In these approaches, the user typically provides initial guidance, such as placing seed points or sketching rough contours around the region of interest (ROI), and the algorithm completes the segmentation based on specified criteria [83]. Semi-automatic techniques are especially advantageous in situations where fully automated methods may face challenges, such as in the presence of image noise, artifacts, or complex anatomical structures. The user's input ensures that segmentation is informed by clinical expertise, while automated algorithms manage repetitive tasks and large datasets, significantly accelerating the process [52].

4.3.5   In-Depth into Semiautomatic Segmentation

Fully manual segmentation of bones in CT images can achieve highly accurate results; however, it is labor-intensive and time-consuming, particularly when dealing with large datasets. While fully automated methods offer

speed, they often fall short in capturing the complexity of bone structures or may struggle with inconsistencies in image quality [89]. For this reason, a semi-automatic segmentation technique was selected, as it provides an optimal balance between user control and automation, enabling precise and efficient segmentation of bone structures with minimal user intervention. This approach combines the precision of manual segmentation with the efficiency of automation, allowing for rapid segmentation of bone structures while preserving the option for manual refinement when necessary. In CT-based bone imaging, the high contrast between bone and surrounding soft tissue typically facilitates segmentation compared to other tissue types. Nevertheless, the complex geometry and internal microarchitecture of bones, especially in regions such as joints, vertebrae, or trabecular bone, demand more sophisticated segmentation methods. The following are some of the most widely used semi-automatic techniques in CT-based bone segmentation:

Thresholding and Refinement

Thresholding is typically the initial step in semi-automatic bone segmentation for CT images. This process involves defining an intensity range to distinguish bone from surrounding soft tissues. In CT images, bone tissue generally displays higher Hounsfield Unit (HU) values, usually between 200 and 3000 HU, depending on factors such as bone type (cortical or trabecular) and imaging settings. By selecting an appropriate threshold range that isolates high-intensity bone pixels, a preliminary segmentation of the bone structure can be achieved [72, 115]. However, basic thresholding can result in over-segmentation or under-segmentation in areas where bone intensity overlaps with other structures, such as metal implants, calcifications, or dense soft tissues. Consequently, manual refinement is often necessary. This may include removing extraneous regions or smoothing irregular boundaries through post-processing techniques, such as morphological operations (e.g., dilation, erosion, closing), to enhance the accuracy of the segmented bone surface [55, 168].

Region Growing Algorithms

Region-growing algorithms are commonly applied in semi-automatic bone segmentation for CT images. In these methods, the user selects one or more seed points within the bone structure, and the algorithm expands the seg-

mented area by iteratively including neighboring voxels with similar intensity values. Region growing is particularly effective in areas where bone intensity is relatively homogeneous, such as in long bones (e.g., femur or tibia) or vertebrae [2, 19]. However, in regions with complex trabecular architecture or low contrast (e.g., joints), this approach may inadvertently segment adjacent tissues or leave gaps within the bone structure. To address these challenges, the user can manually adjust seed points or impose constraints that restrict the region-growing process to a specific anatomical area [48, 95].

Active Contours (Snakes)

Active contour models, or "snakes", are frequently used in semi-automatic segmentation, especially for bones with irregular or complex shapes [52]. This method begins with an initial contour that the user places around the approximate boundary of the bone structure. The contour then iteratively evolves based on image gradients, moving toward areas of high intensity (edges) while avoiding low-gradient regions (soft tissues). The user can adjust the contour at any point in the process to ensure accurate boundary delineation. Active contours are particularly advantageous when segmenting bones with curved or jagged surfaces, such as the scapula, pelvis, or joint surfaces. The iterative nature of the algorithm ensures that the contour closely adheres to the bone's surface, even in areas where bone boundaries are indistinct or obscured by artifacts.

Watershed Segmentation

The watershed algorithm is a region-based segmentation method that interprets intensity values in a CT image as topographical elevations. Beginning from user-defined markers (representing local intensity minima), the watershed algorithm "floods" the image, dividing it into basins that correspond to distinct anatomical structures. In bone segmentation, watershed segmentation is particularly useful for separating closely positioned or overlapping bones, such as in the hand or foot, where multiple small bones are located in proximity [144]. Watershed segmentation is effective in delineating bones within complex anatomical regions but is sensitive to noise. Therefore, preprocessing techniques, such as Gaussian smoothing or edge-preserving filters, are often applied before running the watershed algorithm to reduce noise and enhance the accuracy of the segmented bone surfaces [10, 164].

4.3.6   Applications of Semi-Automatic Segmentation in Bone Health and Surgery

As already mentioned, precise segmentation of bones is crucial in several fields including:

Osteoporosis Assessment

In osteoporosis, semi-automatic segmentation of CT images is used to isolate regions of interest (e.g., femoral neck, lumbar vertebrae) for assessing BMD and trabecular bone microarchitecture. Quantitative measurements of bone mass, such as volumetric BMD, are computed by segmenting the trabecular and cortical bone separately, allowing clinicians to detect early signs of bone fragility and monitor disease progression. This is particularly important for assessing fracture risk in patients with osteoporosis.

4.3.7   Fracture Detection and Pre-Surgical Planning

Accurate bone segmentation is essential for diagnosing fractures and planning surgical interventions. Semi-automatic techniques, such as active contours and region-growing algorithms, are frequently employed to segment bone fragments, enabling the creation of detailed 3D reconstructions of fractured bones. These reconstructions allow surgeons to visualize the extent of the injury and plan corrective procedures, such as fixation or bone grafting, with a high level of precision [13, 106].

Orthopedic Implant Design and Prosthetic Placement

Semi-automatic segmentation is widely utilized in preoperative planning for joint replacement surgeries, including hip or knee arthroplasty. By segmenting the patient's bone structures in CT images, surgeons can develop patient-specific 3D models of the joint anatomy. These models are then used to design custom implants that conform to the patient's bone geometry, improving surgical outcomes and reducing the risk of complications, such as implant loosening or misalignment [106].

Biomechanical Analysis and Finite Element Modeling

Precise bone segmentation is crucial in biomechanical research for creating 3D models appropriate for finite element analysis (FEA). FEA allows for the

simulation of mechanical stresses and strains on bones under various loading conditions, yielding valuable insights into biomechanical properties such as stiffness, strength, and fracture risk. Semi-automatic segmentation techniques provide accurate representation of bone geometry, thereby improving the fidelity of biomechanical models [89, 171].

Challenges and Future Directions in Semi-Automatic Segmentation for Bone Imaging

Despite significant improvements in the accuracy and efficiency of semi-automatic segmentation for bone imaging in CT, several challenges remain. A primary issue is variability in image quality, which can arise from differences in CT acquisition protocols, patient movement, or artifacts such as metal implants. These factors can impact the performance of segmentation algorithms, often requiring additional manual refinement [27]. Another challenge is the integration of machine learning and deep learning algorithms within semi-automatic segmentation workflows. Although AI-based methods show great potential in automating segmentation tasks, they typically require large annotated datasets for effective training and may face difficulties in generalizing across diverse patient populations and imaging modalities. Future research should focus on developing hybrid models that blend the precision of AI-driven segmentation with the flexibility of semi-automatic approaches, creating more robust and adaptable segmentation solutions. Moreover, advancements in 3D visualization and virtual reality are anticipated to enhance the user interface of semi-automatic segmentation tools, making them more intuitive and interactive for clinicians. As these technologies evolve, they are expected to further improve the precision and efficiency of bone segmentation, ultimately contributing to better clinical outcomes for patients [86, 126].

4.4 Implemented Segmentation

The segmentation process began with an initial check to ensure the CT scans were correctly calibrated, with Hounsfield Unit (HU) values already standardized as is typical for modern CT datasets. No additional calibration steps were performed, as the scans were ready for segmentation. The first step in the segmentation workflow was adjusting the CT window to enhance the visibility of bone structures. This adjustment ensured that both cortical and cancellous bone could be visualized more clearly, distinguishing

them from the surrounding soft tissues. Next, a global thresholding technique was applied to isolate the bone tissue from the surrounding tissues. The threshold range for all cases was set between 150 HU and 2000 HU, a typical range for including all bone types, from low-density cancellous bone to high-density cortical bone. The thresholding was performed by selecting the appropriate HU range within the 3D Slicer software. This step was crucial for isolating the bone structures based on their elevated HU values, which correspond to the high-density mineral composition of bone. Once the threshold range was selected, the software automatically segmented the bone regions by assigning voxels within the specified range as bone tissue. However, the segmentation was not immediately perfect, and manual refinement was necessary to address areas where boundary ambiguities or image noise had caused inaccuracies. To achieve this, the Editor module in 3D Slicer was used for manual adjustments. Tools such as Paint and Erase were employed to add or remove voxels as needed, particularly in regions where the algorithm had difficulty with complex anatomy, such as in joint areas (e.g., knee, shoulder). In cases where segmentation boundaries were rough or incomplete due to imaging artifacts or low contrast between bone and adjacent tissues, post-processing tools were applied. The Smooth tool was used to refine the irregular edges that often arose after the initial thresholding step. This created smoother transitions along the bone surfaces, improving the anatomical accuracy of the segmented bone. Additionally, the Clean tool was utilized to eliminate noise and small, disconnected segments that may have been erroneously included during the region-growing process. With the segmented regions adjusted and refined, the 3D Slicer visualization tools allowed for the rendered 3D model to be reviewed. By rotating and zooming into the 3D model, real-time feedback ensured that any gaps or inconsistencies in the segmentation could be promptly corrected. This was particularly important for complex regions, such as the pelvis and vertebrae, where precise segmentation is critical for further analyses. Once the bone structures were accurately segmented, the final models were exported into standard file formats, such as STL or OBJ, using 3D Slicer's Export function. These files were then ready for downstream applications, such as finite element analysis (FEA) or 3D printing for surgical planning. This semi-automatic segmentation approach, combining automated thresholding with manual refinement, allowed for a more accurate and efficient process compared to fully manual segmentation methods. The workflow provided precise bone delineation,

enabling further quantitative analysis and clinical applications.
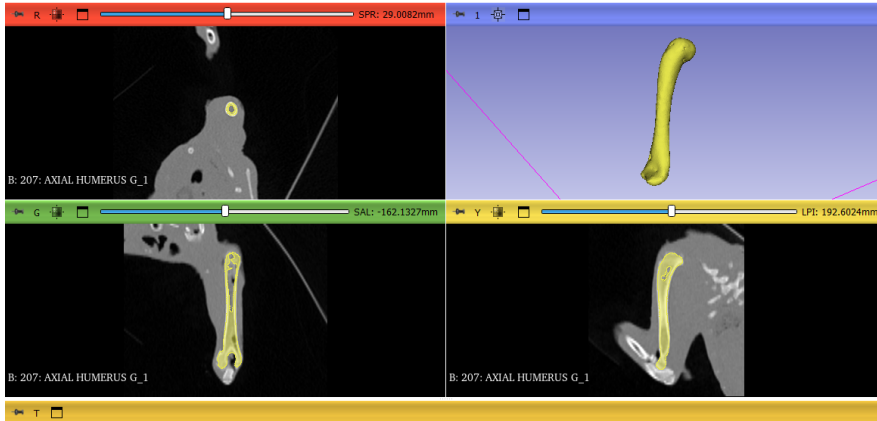
Figure 4.2: Medical Imaging Processing in 3DSlicer

4.5 Conclusion

The use of semi-automatic segmentation with 3D Slicer version 5.6.2 proved to be an effective balance between accuracy and efficiency in segmenting bone structures from CT images. The combination of thresholding, region-growing algorithms, and manual refinement tools ensured precise delineation of bone surfaces, even in complex areas such as joints or regions with intricate morphologies. Post-processing tools like Smoothing and Cleaning further enhanced the quality of the segmentation, making it suitable for downstream applications such as biomechanical analysis and surgical planning. This approach optimized processing time while maintaining anatomical fidelity, making semi-automatic segmentation an ideal solution for detailed studies of bone morphology.

Chapter 5

Radiomics Application

This chapter outlines the development of a custom Python-based radiomic feature extraction system that mimics the capabilities of tools like 3D Slicer, with added flexibility and customization options. Additionally,it explores the Principal Component Analysis (PCA) and its application to reduce the dimensionality of radiomic data, and statistical methods such as t-tests to evaluate differences between femur and humerus bones in feline specimens.

5.1 Introduction

Capturing the complete complexity of bone microarchitecture is essential for understanding bone strength and fracture resistance. Radiomics provides a more comprehensive approach by facilitating the extraction of quantitative imaging features that represent tissue heterogeneity, texture, and structural organization [78, 80, 108]. This type of analysis has the potential to reveal subtle patterns in bone images that may be useful for diagnosing conditions such as osteoporosis and predicting mechanical properties.

5.2 Dataset Overview

The dataset for this study included DICOM images and STL models from three feline subjects. The DICOM images were captured via CT providing detailed cross-sectional views of the entire body of each subject. These

images were acquired in three anatomical planes (axial, sagittal, and coronal) to offer a comprehensive, three-dimensional representation of the bone structures. The STL models, generated through the segmentation processes, consisted in the isolated femurs and humeri of each subject. These models served as a basis for the extraction of radiomic features and enabled precise geometric and shape analysis. Both the DICOM images and STL models were visualized and processed using 3D Slicer. The primary aim of this preparatory phase was to establish a clear and consistent workflow for importing, processing, and segmenting the data, ensuring that the bones of interest could be isolated and analyzed for radiomic feature extraction. Once obtained the STL models, they were imported and converted into segmentation nodes for the segemntation phase ensuring that the radiomic features extracted would exclusively represent the bone structures of interest. Segmentation plays a crucial role in radiomic analysis, as it defines the boundaries of the anatomical regions being studied, and errors in segmentation can introduce noise or irrelevant data into the feature extraction process. Using the segmentation nodes created from the STL models, the DICOM images were aligned with the segmented bones to ensure accurate feature extraction. 3D Slicer's Radiomics module was then used to extract a broad range of radiomic features from the DICOM images [155], including:

- Shape features, which, as already seen, describe the geometric properties of the bone (e.g., volume, surface area, compactness).

- First-order statistics, which, as already emntioned, quantify the distribution of voxel intensities within the bone.

- Second-order features, derived from texture matrices, which, as alreadye xplained, capture the spatial relationships between voxel intensities, offering insights into bone microarchitecture [3, 174].

5.3   Feature Extraction

5.3.1   Development of the Custom Python Workflow

While 3D Slicer offers a robust platform for radiomic analysis, we have developed a custom feature extraction tool within a Python environment. Python was chosen because of its versatility, rich ecosystem of libraries (e.g., SimpleITK, PyRadiomics, and matplotlib), and ease of integration with machine

learning and statistical analysis tools. This environment allows us to obtain the necessary characteristics while offering full control over the feature extraction process. Additionally, Python enables better adaptability, particularly for handling complex or varying anatomical structures. The modular nature of Python makes it easy to modify or extend the workflow as needed, providing a highly customizable solution for radiomic analysis. By developing this custom workflow, we retain the flexibility to fine-tune the feature extraction process, making it especially useful when dealing with different species or anatomical regions. This customization is not always achievable with more rigid platforms like 3D Slicer, which, while powerful, might not offer the same degree of flexibility for unique or highly specific analysis requirements. The custom system was developed using the Spyder integrated development environment, part of the Anaconda distribution. The custom code was designed to extract radiomic features from DICOM images of bones, mirroring and extending the functionality of 3D Slicer's Radiomics module.

Several Python libraries were critical to the development of this custom system:

- SimpleITK: A library designed for medical image processing, essential for loading and manipulating DICOM images.

- PyRadiomics: An open-source Python library specifically tailored for radiomic feature extraction. PyRadiomics follows standardized workflows for calculating first-order, second-order, and shape features from medical images.

- matplotlib.pyplot: A popular Python library used for visualizing images in different anatomical planes, including axial, sagittal, and coronal views.

The workflow for the code followed a structured series of steps shown in Fig. 5.1 designed to ensure accurate feature extraction and easy adaptation for future studies. The steps are outlined below:

- Loading DICOM Images and Segmentation Masks: The first step involved loading the DICOM images of the bone samples along with the segmentation masks, which were saved in .NRRD format. This ensured that only the regions corresponding to the femur and humerus were analyzed, excluding any surrounding tissue or background noise.

- Image Verification and Alignment: To ensure that the DICOM images and segmentation masks were properly aligned, the origins and voxel spacings were checked. This step was crucial for preventing misalignment between the images and the masks, which could lead to inaccurate feature extraction. The results of these first two steps are reported in Fig. 5.2.

- Radiomic Feature Extraction: Using the PyRadiomics library, the code extracted a comprehensive set of radiomic features from the images. The radiomic features extracted from the bone regions fell into three broad categories:

    First-order statistics: These features describe the intensity distribution within the bone region. Key metrics included mean intensity, standard deviation, skewness, and kurtosis. These features are crucial for quantifying the overall density and distribution of mineralized tissue in the bone.

    Shape features: Shape features such as volume, surface area, sphericity, and compactness provided insights into the bone's geometric properties. These features are especially important for understanding how the cortical and trabecular bone structures contribute to the bone's overall mechanical stability.

    Texture features: Texture features, derived from matrices such as the Gray-Level Co-occurrence Matrix (GLCM), Gray-Level Run Length Matrix (GLRLM), and Gray-Level Size Zone Matrix (GLSZM), captured spatial relationships between voxel intensities.

        GLCM contrast measures the difference in intensity between neighboring voxels, offering insights into the trabecular microarchitecture.

        GLRLM short run emphasis highlights uniformity in bone texture, which is useful for analyzing trabecular thickness.

        GLSZM large zone emphasis identifies larger, homogeneous zones within the bone, which is indicative of regions with uniform mineralization.

By extracting these features, the system provided a detailed analysis of the bone's structural properties, revealing critical information about trabecular

and cortical organization [56, 63, 88, 156].
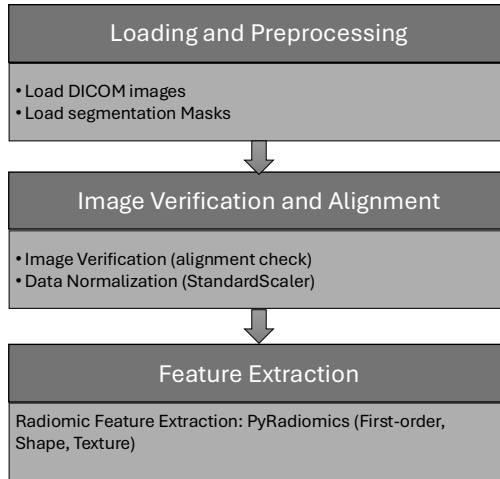
Figure 5.1:   Workflow of the custom-built feature extractor o replicate
3DSlicer performance

5.3.2   Radiomics Features Related to Bone Structures

The radiomic features extracted from the CT images provides critical insights
into the bone structure and quality.

- First-order features: including metrics such as mean intensity and en-
  tropy, reflect the overall density and complexity of the trabecular net-
  work. High entropy values indicate heterogeneous and complex trabec-
  ular patterns, often associated with healthy bone, whereas lower values
  point to more homogeneous bone tissue, characteristic of osteoporotic
  bones [122, 156].

- Second-order features: derived from the previous mentioned texture
  matrices, provide a more nuanced analysis of bone microarchitecture.
  For example, GLCM contrast and correlation capture the intricacy of
  trabecular organization, where elevated values typically correlate with
  a more interconnected and robust bone structure, indicative of greater
  bone health [56, 67].
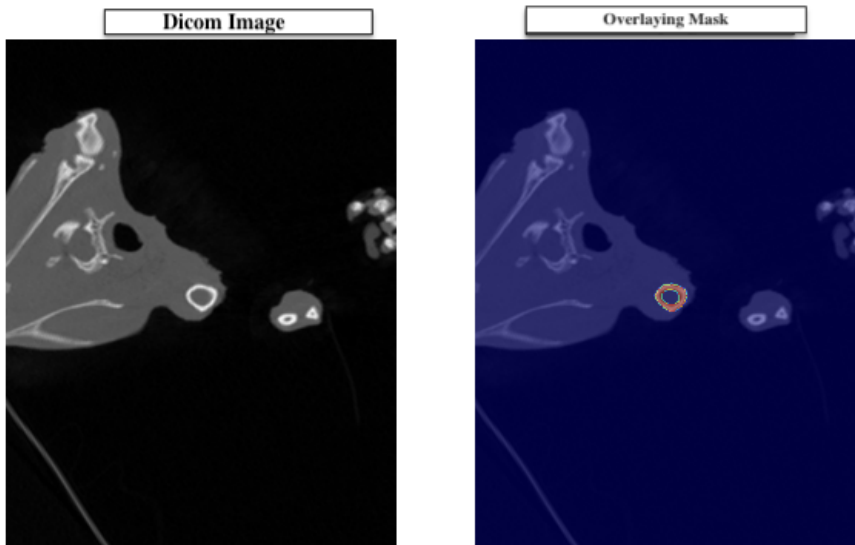
Figure 5.2: Images from the custom-built feature extractor.

5.4   Comparison with 3D Slicer

The radiomic features extracted using the custom Python code were compared with those obtained from 3D Slicer's Radiomics module. The reason for comparing with 3D Slicer is that it is widely regarded as the gold standard in medical image processing and radiomics analysis. 3D Slicer has been extensively validated in the scientific community and is trusted for its accuracy and reliability in extracting medical imaging features from a variety of modalities, including CT and MRI scans. It offers a comprehensive suite of tools for segmentation, feature extraction, and visualization, which is why it is considered the gold standard for radiomic analysis. The comparison showed high consistency between the results of the custom Python system and those obtained from 3D Slicer, with only minor discrepancies observed in shape-based features. This demonstrates that the custom Python workflow can serve as a flexible and reliable alternative to 3D Slicer for large-scale radiomic studies. The custom system's flexibility allows for fine-tuning the feature extraction process, making it adaptable to a wide range of anatomical regions and imaging modalities. The custom Python feature extraction system was validated by comparing its results with those obtained from 3D

Slicer's Radiomics module. The comparison showed high consistency, with only minor discrepancies in shape-based features. This demonstrated that the custom workflow could serve as a flexible and reliable alternative for large-scale radiomic studies. Further validation can be achieved through external benchmarking and comparisons with real-world clinical data, ensuring its robustness and applicability in diverse research settings.

5.5   Principal Component Analysis

Radiomic feature extraction often results in large, high-dimensional datasets that include redundant or irrelevant features. To reduce the dimensionality of the dataset and focus on the most significant features, Principal Component Analysis (PCA) was applied. PCA is a statistical technique that transforms the original set of features into a smaller set of uncorrelated variables called principal components. These components capture the maximum variance in the dataset, allowing for more straightforward interpretation of the data. PCA effectively addresses issues like multicollinearity, which is common in radiomic datasets where many features are highly correlated. Before applying PCA, the data were normalized using the Python function "StandardScaler", which standardized each feature to have a mean of zero and a variance of one. This step is essential because it ensures that all features, regardless of their original scale (e.g., intensity vs. volume), are treated equally during the analysis. Normalization makes sure that the PCA is not biased by the scale differences among features. PCA was performed on the normalized dataset, resulting in a set of principal components that represent linear combinations of the original features. The first principal component (PC1) captures the direction of maximum variance in the data, while subsequent components capture progressively smaller amounts of variance. This allows us to identify the most important features for distinguishing between different bone structures. The variance explained by each principal component was evaluated, revealing that PC1 explained 51.78% of the total variance, followed by PC2 with 21.71%, and PC3 with 17.61%. Together, these three components accounted for over 91% of the total variance, indicating that the majority of important information in the dataset was captured by these components. PCA also enabled the identification of features that contributed most significantly to each principal component. For example, PC1 was strongly influenced by intensity-based features such

as mean intensity and entropy, while PC2 was dominated by shape features like sphericity and compactness. These components can be further analyzed to link specific characteristics to bone health and structural integrity.

5.6   PCA Patterns

We decided to examine the features that characterize the first two PC component to investigate the presence of specific patterns.

- PC1: The first principal component was largely driven by intensity-based and texture features, capturing the overall variance in bone density and trabecular complexity. High PC1 values indicated bones with a more regular, dense structure, while lower values were associated with bones that exhibited a more heterogeneous and disorganized trabecular network.

- PC2: The second principal component was dominated by shape-based features, such as sphericity and surface area, reflecting the geometric differences between femur and humerus bones. PC2 highlighted the biomechanical role of these bones, as the femur typically has a more compact, load-bearing structure, while the humerus is longer and more flexible, accommodating a wider range of motion.

- PC3: The third principal component was mainly shaped by advanced texture features, including gray-level co-occurrence and size-zone matrices, which offer in-depth insights into the fine structural characteristics within the bone. PC3 captured delicate differences in trabecular connectivity and porosity, differentiating bones with intricate, networked structures from those with more sparse and isolated frameworks. High PC3 values indicated bones with detailed trabecular patterns and potentially enhanced mechanical adaptability, while lower values corresponded to a simpler, less interconnected trabecular structure.

5.7   T-test for Femur and Humerus Comparison

After performing PCA, a t-test was conducted to compare the features associated with PC1 and PC2 between the femur and humerus bones. The t-test is a statistical method used to evaluate whether the means of two groups (in this case, femurs and humeri) are significantly different [53, 158]. The t-test for PC1 features revealed no statistically significant difference between femurs and humeri, suggesting that intensity-based and texture-based features did not differ significantly between these bone types [132]. The t-test for PC2, however,The t-test for PC2 yielded a p-value of 0.06, indicating a near-significant difference between the femurs and humeri in terms of shape and geometric features associated with PC2. This result aligns with known biomechanical differences between these bones, as the femur typically exhibits a more compact, spherical structure, while the humerus is more elongated. The p-value of 0.06 may be attributable to the small sample size [158]. The complete workflow is reported in Fig. 5.3

5.8   Conclusion

This chapter presents a detailed account of the development of a custom Python-based radiomic feature extraction system, the application of PCA, and the statistical analysis of radiomic data from feline bone samples. The custom Python code provided an efficient and flexible solution for extracting radiomic features, with results that were consistent with those obtained using 3D Slicer. The application of PCA enabled the reduction of high-dimensional data into a few meaningful principal components, with PC1 capturing variations in bone density and texture, and PC2 reflecting geometric differences between femur and humerus bones. The t-test results confirmed that while intensity and texture features were not significantly different between femur and humerus bones, shape-based features showed a near-significant difference, aligning with the distinct mechanical roles of these bones. Overall, this study demonstrates the potential of custom radiomic analysis tools in providing a deeper understanding of bone health, offering a foundation for future research in predicting mechanical properties and assessing fracture risk. The flexibility of the Python-based system makes it a valuable asset for future studies, particularly those focusing on the biomechanical proper-

ties of bones and the early detection of bone diseases such as osteoporosis.
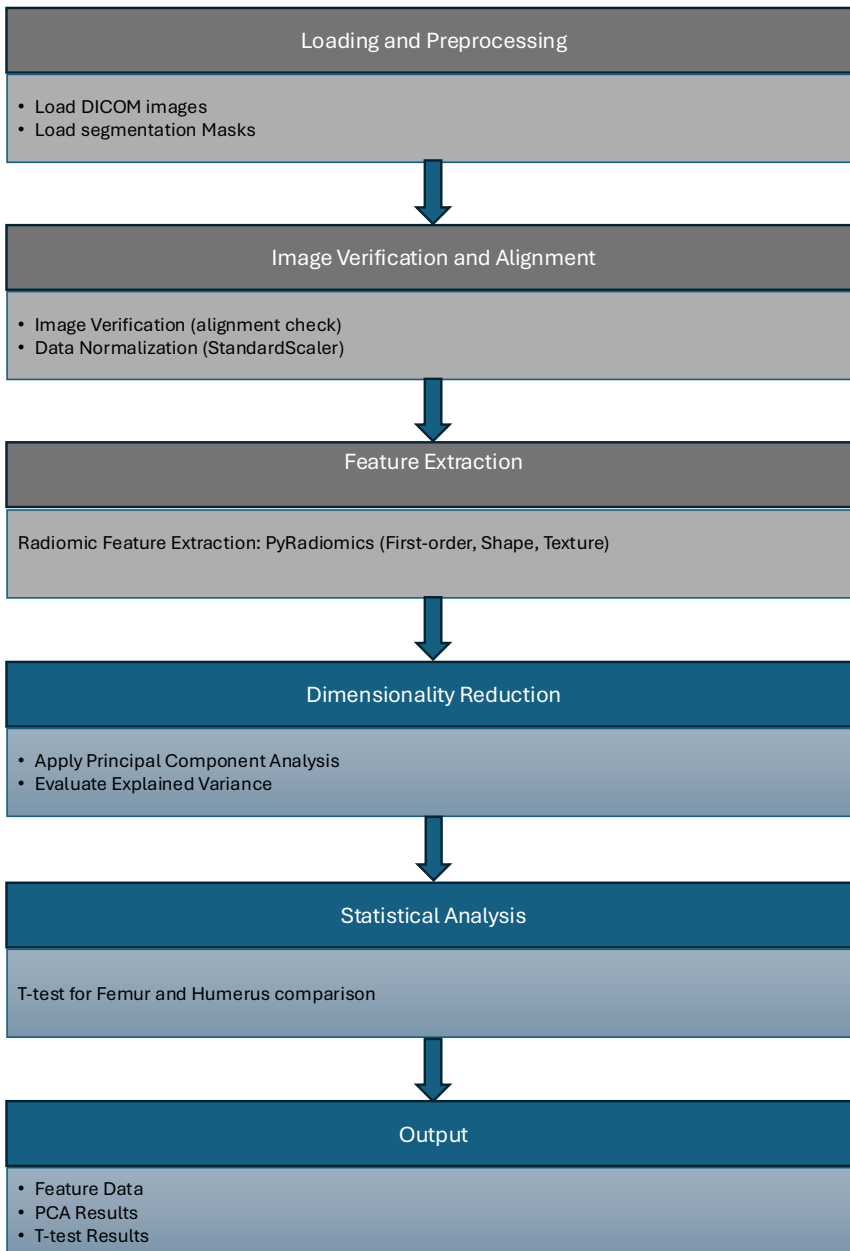
Figure 5.3:   Workflow of the code implemented.

Chapter 6

Mechanical Tests

This chapter explores bone mechanics, starting from tests conducted on PLA bone samples to determine the most suitable testing methods for actual bone specimens. The preliminary tests on PLA guided the selection of optimal procedures for assessing real bone samples. Subsequently, the chapter discusses the tests implemented on extracted bones, highlighting the methods and techniques used to evaluate the mechanical and structural properties of bone tissue.

6.1 Introduction

Bone is a complex, hierarchical tissue with distinct mechanical properties that vary according to its microstructure, composition, and the direction and magnitude of applied forces. These properties, along with bone's remodeling processes and biological responses, enable it to endure a wide range of mechanical loads, including tension, compression, and shear. To accurately model bone behavior and predict its response to stress, researchers have developed various material models that account for directional variations in its properties. Understanding the mechanical properties of bone is crucial for various applications in biomechanics, particularly in the design of orthopedic implants and the assessment of fracture risk. To accurately model bone behavior, different mechanical models are used, including isotropic, anisotropic, transversely isotropic, and orthotropic models. Each of these models captures unique aspects of bone's mechanical complexity, making

them essential for finite element analysis (FEA). FEA plays a key role in simulating bone behavior under different conditions, which is vital for developing effective treatments for bone diseases such as osteoporosis and for designing prostheses that meet the biomechanical needs of patients. [31].

6.2   Mechanical Properties of Bones

Bone's mechanical strength is dynamic, continuously adapting to mechanical demands through the process of bone remodeling. This process ensures that bones maintain both structural integrity and mechanical competence over time. Bone remodeling is governed by mechanotransduction, whereby mechanical forces are converted into cellular responses [20,45]. Osteocytes, embedded within the bone matrix, detect strain induced by mechanical loading and transmit signals to osteoblasts and osteoclasts to either form or resorb bone tissue, depending on the loading patterns. The mechanical competence of bone is determined by multiple factors, including BMD and microarchitecture (the internal organization of trabecular structures and cortical thickness), both of which influence bone's fracture resistance. Key material properties, such as the stiffness, strength, and toughness of the bone matrix, also play a critical role. Bone density is a crucial factor in its mechanical properties, as higher density generally correlates with greater stiffness and strength. However, bone quality, which encompasses both microarchitecture and material properties, also significantly impacts bone strength. In conditions such as osteoporosis, where bone density diminishes, the loss of trabecular connectivity and cortical thinning are major contributors to the increased risk of fractures [31,35].

Bone is categorized into two main structural types:

- Cortical bone (compact bone): This dense outer layer primarily forms the outer shell of bones, especially in long bones such as the femur, and provides much of the bone's strength and stiffness. Cortical bone is considerably denser than trabecular bone and exhibits high stiffness and strength, particularly along the longitudinal axis, with osteons aligned parallel to this axis, contributing to its anisotropic properties. Cortical bone resists compressive, tensile, and torsional forces, making it essential for the load-bearing capacity of long bones [99].

- Trabecular bone (spongy or cancellous bone): Found primarily at the

ends of long bones and within vertebrae, trabecular bone consists of a porous network of trabeculae that provides lightweight structural support and aids in mechanical load distribution. Its lattice-like structure, composed of interconnected trabeculae, aligns along principal stress trajectories, resulting in high anisotropy. The mechanical properties of trabecular bone are largely dependent on its bone volume fraction (the ratio of bone volume to total volume), along with trabecular thickness, number, and spacing [73, 99].

These two types of bone, with their distinct structural properties, contribute to bone's overall mechanical resilience and its ability to adapt to various loading conditions.

6.3 Material Models for Bones

Bone material models are crucial for accurately simulating the complex mechanical behavior of bone tissue under various loading conditions. Unlike conventional materials, bone exhibits unique structural characteristics, such as anisotropy and heterogeneity, that vary across different regions of the skeleton. These properties imply that bone's mechanical response is highly dependent on the direction and type of load applied, particularly in load-bearing regions like the femoral shaft. To capture these complexities, various models are employed, including isotropic, anisotropic, transversely isotropic, and orthotropic models, each offering differing levels of precision and applicability based on the specific characteristics of the bone region under investigation. Material models used in biomechanics typically follow the principles of linear elasticity, which assumes that the material deforms proportionally to the applied stress. In these models, the relationship between stress and strain is represented by a linear function, with the elastic modulus being a key parameter. This assumption is valid for bone under physiological loading conditions, where deformations are small and reversible. However, in cases of extreme loading, non-linear effects such as plastic deformation or fracture may become significant, requiring non-linear material models.

6.3.1 Isotropic Material Model

In an isotropic material model, mechanical properties such as stiffness and strength are assumed to be uniform in all directions. This assumption greatly

simplifies computational simulations, making isotropic models a practical choice for initial approximations, particularly when analyzing trabecular bone in regions where trabeculae are densely interconnected and relatively uniform [35]. Isotropic models offer the advantage of computational efficiency by reducing simulation complexity and removing directional variability. However, this simplification also introduces limitations, as isotropic models tend to oversimplify bone structure and underestimate its complexity. Specifically, isotropic models fail to capture the directional dependencies inherent in real bone, particularly in load-bearing areas like the femoral shaft, where bone tissue exhibits anisotropy, with mechanical properties that vary according to the direction of applied loads. This directional strength is essential for bones that support body weight and respond to dynamic forces. Therefore, while isotropic models are valuable for basic simulations and as a foundation for preliminary studies, they lack the precision required for in-depth biomechanical assessments [31, 35].

6.3.2   Anisotropic Material Model

Anisotropic materials exhibit varying mechanical properties depending on the direction of the applied force. This characteristic aligns with bone's internal structure, particularly the alignment of osteons in cortical bone and trabeculae in cancellous bone, which adapts based on the stresses imposed on it. Anisotropic models provide a more accurate representation of bone's mechanical behavior, especially in long bones such as the femur, which must withstand significant loading along their longitudinal axis. For example, the anisotropic nature of cortical bone results in greater stiffness and strength along the longitudinal axis compared to the transverse axis [169]. The specific characteristics of anisotropy in bone are as follows:

- **Longitudinal Axis**: Bone exhibits its highest stiffness and strength along this axis, aligning with the primary direction of mechanical loading during activities such as walking or running.

- **Transverse Axis**: Due to the orientation of osteons, bone is relatively weaker along this axis, rendering it more susceptible to shear forces.

In trabecular bone, the alignment of trabeculae along principal stress trajectories also leads to anisotropic behavior. Trabecular bone is optimized to resist compressive forces, particularly in regions like the spine and the

ends of long bones [134]. As mentioned earlier, the mechanical properties of trabecular bone are strongly influenced by factors such as bone volume fraction, trabecular thickness, and trabecular orientation [31, 134].

6.3.3 Transversely Isotropic Material Model

A transversely isotropic material has identical properties in all directions within a plane perpendicular to a single axis but exhibits different properties along that axis [159]. This model is frequently used to simulate the mechanical behavior of long bones, where the longitudinal axis shows distinct mechanical properties compared to the transverse plane. Long bones, such as the femur and tibia, are often modeled as transversely isotropic due to their different mechanical responses along the longitudinal axis versus the transverse plane. For instance, while the mechanical properties around the circumference of the femur (in the transverse plane) are relatively uniform, the bone along the longitudinal axis is specifically adapted to withstand compressive and tensile forces. Key characteristics of transversely isotropic materials in bone include:

- **Isotropic in One Plane**: In the transverse plane (circumferential direction), bone behaves isotropically.

- **Distinct Along One Axis**: Along the longitudinal axis, bone demonstrates increased stiffness and strength, largely due to the alignment of osteons and collagen fibers [159].

6.3.4 Orthotropic Material Model

An orthotropic material has distinct mechanical properties along three mutually perpendicular axes, making it the most detailed material model for bone, capturing variations along the longitudinal, radial, and tangential directions [31, 175]. In cortical bone, an orthotropic model is particularly appropriate due to the unique mechanical properties observed along different orientations:

- **Longitudinal Axis**: Along the length of the bone, this axis displays the highest stiffness and strength.

- **Radial Axis**: Extending outward from the bone's center, mechanical properties vary, reflecting changes in bone density.

- **Tangential Axis**: Along the circumference, properties are influenced by the circumferential organization of osteons.

The orthotropic properties in bone are distributed as follows [175]:

- **Longitudinal Direction**: This is the stiffest and strongest direction, reflecting bone's primary function in weight-bearing.

- **Radial Direction**: Properties vary with density and structure as the distance from the bone's center increases.

- **Tangential Direction**: Influenced by the arrangement of collagen fibers and osteons, this direction provides strength against bending and torsional forces.

This model offers a nuanced understanding of bone's mechanical complexity, particularly useful for accurately simulating bone behavior in biomechanical studies.

6.4   Tests

In biomechanics, bending tests are essential for evaluating the mechanical properties of bones, such as stiffness, flexural strength, and fracture behavior. Two common methods-three-point and four-point bending tests-are widely used, each with its advantages and limitations depending on the material type, specimen geometry, and research objectives. In this study, we evaluated both the three-point and four-point bending tests to determine which method is best suited for assessing the mechanical properties of bone. The specimens used for the tests were fabricated from Polylactic Acid (PLA) based on bone structures segmented from CT images of feline specimens, using a 3D printer. These PLA samples were selected for their practical use in preclinical testing, with the main focus being on selecting the appropriate bending test rather than analyzing the material response itself. By conducting preliminary tests on PLA, we could observe the performance of both bending test setups and choose the most effective method for our research objectives. The setups for the three-point and four-point bending tests are illustrated in Figure 6.1 [103]. Although both methods are suitable for evaluating mechanical properties, we found that the four-point bending test produced unexpected, asymmetric results, making it unsuitable for our study's specific objectives.

Below, we describe the mechanics of both three-point and four-point bending tests [74, 151].
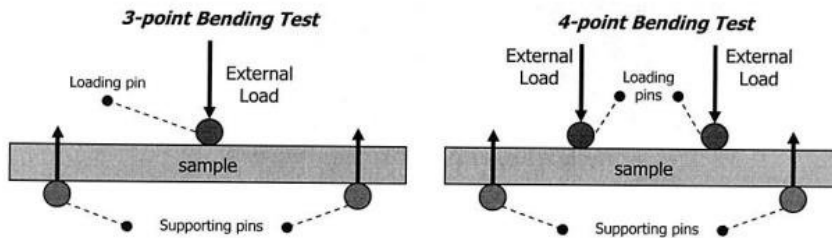
Figure 6.1: Schematic illustration of three-point and four-point bending tests [adapted from [103]].

6.4.1   Three-Point Bending Test

The three-point bending test is commonly used to assess the flexural strength, stiffness, and fracture behavior of bones, especially under bending forces similar to those encountered during walking, running, or lifting. This test is essential for understanding the bone's structural integrity, fracture resistance, and overall mechanical competence [151].

Test Setup

In a three-point bending test, a bone sample is supported at two points, with a third point applying a downward force at the midpoint. This configuration creates a bending moment that allows for the analysis of the deformation and fracture behavior of the bone sample. Key components of the three-point bending setup include:

- **Two Supports**: The bone sample is placed on two cylindrical supports, set a fixed distance apart.

- **Loading Point**: A vertical force is applied at the midpoint between the supports, producing a bending moment.

- **Loading Rate**: The force is applied at a controlled rate, enabling the observation of bone deformation and fracture behavior under load.

Mechanics of the Three-Point Bending Test

The bone experiences two types of stress under the applied load:

- **Compression**: The upper surface of the bone experiences compressive stress due to the applied load.

- **Tension**: The lower surface of the bone experiences tensile stress, stretching under the bending force.

The maximum stress occurs at the bone's midpoint, directly beneath the applied load. Failure typically happens when tensile stress exceeds the bone's strength, leading to a fracture on the tension side.

Mechanical Parameters Measured

During a three-point bending test, the following mechanical parameters are measured:

- **Flexural Strength**: This is the maximum stress the bone can withstand before failure, calculated using the formula:

$$\sigma = \frac{3FL}{2bd^2}$$

  Where:

    - F = maximum applied force
    - L = distance between supports
    - b = bone sample width
    - d = bone sample depth (thickness)

- **Stiffness (Flexural Modulus)**: Reflects the bone's resistance to deformation under load, derived from the slope of the force-displacement curve. The formula is:

$$E = \frac{L^3 F}{4bd^3\delta}$$

  Where:

    - L = support span length (distance between supports)

- F = applied load at the midpoint
- b = specimen width
- d = specimen thickness (depth)
- δ = midpoint deflection

- **Fracture Toughness**: Describes the bone's resistance to crack propagation, quantified by the critical stress intensity factor K_{IC}.

- **Ultimate Load and Displacement**: Represent the maximum load the bone can withstand before fracture and the degree of deformation under this load, respectively.

Influence of Bone Microstructure on Bending Behavior

Bone's hierarchical structure significantly influences its response to bending tests. Cortical bone provides the main bending resistance in long bones, particularly in load-bearing regions like the femoral shaft. On the other hand, trabecular bone, while less stiff, plays a key role in regions requiring flexibility and energy absorption, such as the ends of long bones.

Factors Affecting Three-Point Bending Results

Several factors can influence the results of a three-point bending test on bone samples:

- **Bone Geometry**: The size and shape of the bone sample substantially affect bending results. For instance, longer bones with a greater cross-sectional area show increased resistance to bending forces. Accurate measurement of bone geometry is essential when calculating mechanical parameters.

- **Bone Density and Quality**: BMD is a key factor in bone strength, with denser bones typically exhibiting greater stiffness and strength. However, bone quality, including trabecular microarchitecture and bone matrix properties, is also crucial for understanding the bone's response to bending.

- **Loading Rate**: The rate at which force is applied influences fracture behavior. Higher loading rates often result in more brittle fractures, with less deformation prior to failure, whereas lower loading rates allow for greater plastic deformation.

The three-point bending test has both clinical and research applications, particularly in the study of bone health and diseases like osteoporosis.

- **Osteoporosis Research**: In osteoporotic bones, reduced density and compromised microarchitecture increase fracture susceptibility. The three-point bending test quantifies these mechanical deficits, offering a direct measurement of the impact of osteoporosis on fracture risk.

- **Bone Implant and Prosthetic Design**: Mechanical data from three-point bending tests inform the design of orthopedic implants and prostheses. By understanding bone responses to bending forces, engineers can create implants that more accurately mimic natural bone properties, thereby improving stability and longevity.

The three-point bending test is a valuable method for assessing bone mechanical properties, particularly flexural strength, stiffness, and fracture behavior. It provides insights into bone health, the effects of aging and disease, and the performance of orthopedic implants. As conditions like osteoporosis become more prevalent, this test remains an essential tool in both clinical assessments and biomechanical research. By simulating how bones react to mechanical loads, the three-point bending test enhances our understanding of bone strength and fracture risk, advancing orthopedic and biomechanical research and practice [35, 124].

6.4.2   Four-Point Bending Test

The four-point bending test is a structural testing method that applies two forces, equally spaced between two supports, resulting in a constant bending moment in the region between the load points. Unlike the three-point bending test, which concentrates load at a single point, the four-point test distributes the load over a broader area.

6.4.3   Test Setup

The setup for the four-point bending test includes:

- **Two Inner Loads**: Applied at equal distances from the center, creating a constant bending moment between the inner load points.

- **Outer Supports**: These provide support to the sample while the forces are applied at the inner load points.

6.4.4 Mechanics of the Four-Point Bending Test

: The four-point bending test creates a constant moment region between the two inner load points, ensuring uniform bending stress across this section. The stress distribution is similar to the three-point test but is extended over a larger section of the bone sample. Key characteristics of the four-point bending test include:

- **Constant Moment Region**: The bending moment is constant in the region between the two inner load points, resulting in uniform stress.

- **Stress Distribution**: Similar to the three-point test, bone experiences compressive stress on the upper surface and tensile stress on the lower surface. However, this uniform stress distribution extends over a longer section of the sample, providing a more accurate assessment of pure bending behavior.

A significant advantage of the four-point bending test is the elimination of shear forces in the constant moment region, making it particularly useful for long bones like the femur, where shear forces can complicate bending analysis [70].

6.5 Comparison Between Three-Point and Four-Point Bending Tests

The three-point and four-point bending tests are both commonly used to evaluate the mechanical properties of bone, particularly flexural strength, stiffness, and fracture behavior. While they share similarities in their basic principles, the key difference lies in the way the load is applied and distributed across the bone sample. In the three-point bending test, a single force is applied at the midpoint of the bone sample, with two support points at either end. This creates a bending moment at the center, with maximum stress occurring directly under the applied load. The bending moment and stress are concentrated in a small region, leading to higher localized stress, which can cause fracture initiation at this point. This setup is particularly useful for studying fracture behavior at a specific site of maximum stress. In contrast, the four-point bending test applies two equal forces at a fixed distance apart, with two support points on either side. This results in a constant bending moment region between the two inner load points, leading

to a more uniform distribution of stress over a larger section of the bone. This setup eliminates shear forces within the constant moment region and allows for a more precise assessment of pure bending behavior. The four-point bending test is useful when uniform stress distribution is required, and it is particularly valuable in long bones, where shear forces complicate bending analysis.

6.5.1   Key Differences

:

- **Load Distribution**: In the three-point test, the load is applied at a single point, resulting in a concentrated stress region. In the four-point test, the load is distributed across two points, leading to a more uniform stress distribution over a larger region.

- **Bending Moment**: The three-point test creates a bending moment at the midpoint, whereas the four-point test creates a constant bending moment between the two inner load points, which helps eliminate shear forces.

- **Stress Distribution**: The three-point bending test is more likely to induce higher localized stress, leading to fracture initiation at the load application point. The four-point test, with its constant moment region, helps achieve more uniform bending, making it suitable for assessing pure bending behavior without shear complications.

Although both methods have their advantages, the choice of test depends on the specific objectives of the study and the bone structure being analyzed. For example, the three-point bending test is ideal for evaluating fracture toughness and local failure characteristics, while the four-point test is better suited for studying uniform bending behavior over a longer section of the bone.

6.6   Preclinical Tests

In biomechanics, bending tests are indispensable for evaluating the mechanical properties of bones and bone-like materials. The three-point and four-point bending tests are among the most commonly employed methods, providing insights into the stiffness, strength, and fracture behavior of these

materials. This study compared the two bending tests to determine which method best supports accurate mechanical characterization of bones. Ultimately, this work aims to validate a patient-specific Finite Element Model (FEM) for potential human applications, enhancing our understanding of bone mechanics and improving clinical assessments. The primary objective of this study was to develop and evaluate an experimental protocol using 3D-printed PLA models to validate the feasibility of mechanical tests, and ultimately contribute to the design of a patient-specific human model for fracture prediction in patients with osteoporosis. Starting from the femurs and humeri, segmented from CT scans of three feline specimens, 3D-printed replicas were produced using PLA, designed to be destroyed during the tests. The process of 3D printing is reported in Fig. 6.2. Both three-point and four-point bending tests were conducted using an Ametek LS5 test machine with a 1kN load cell in displacement control mode. Three samples were printed for each bone type (humerus and femur). The dimensions and geometry of the samples matched those of the real bones used in the actual experimental tests as they were derived directly from CT images. This was essential to make the test results meaningful. The curved shapes of the femurs and humeri, replicated from the actual bones, led to discrepancies in load application and stress distribution between the three-point and four-point bending methods.

In the three-point bending test: the sample was placed between two supports as shown in Fig. 6.3. A single point load was applied at the midpoint between the supports. Stress and strain were calculated based on the deformation observed at the midpoint.

In the four-point bending test: two loading points were placed equidistant from the supports, creating a constant bending moment between them. Stress was distributed more uniformly along the sample, particularly in the central region between the two loading points.

The results of the tests highlighted significant differences between the two methods.

The three-point bending test provided consistent and predictable results for all samples:

the stress distribution was symmetrical, with clear fracture points observed. Measurements of flexural strength and stiffness were straightforward and aligned with expectations. The four-point bending test, however, yielded less reliable results:

- Asymmetric stress distribution: several samples exhibited asymmetric

deformation, where the load distribution was uneven. This issue was likely caused by the non-homogeneous properties of the PLA material and the curved geometry of the samples, particularly in the femurs and humerus

- Load application issues: the curved shape of the bones led to incorrect load application, making the test unreliable for determining mechanical properties in our samples. The constant moment region failed to behave as expected, and the asymmetric deformation ultimately turned the four-point test into a variant of a three-point test

The stiffness was calculated as the force-displacement ratio in the elastic region of the bending tests. For the three-point test, this ratio was clear and consistent across the PLA samples. However, in the four-point test, load misapplication led to erroneous stiffness values that did not reflect the true mechanical properties of the bones. In the three point bending tests, the stiffness results were highly consistent, with the femur showing a 25% higher stiffness compared to the humerus, corroborating findings from literature (153.85 ± 33.25 $\frac{N}{mm}$ for femurs and 116.38 ± 23.36 $\frac{N}{mm}$ for humeri). In the four-point bending test due to the non-uniform load distribution, the stiffness results were unreliable, reinforcing the decision to discard the four-point bending test for further analysis. The asymmetric behavior observed in the four-point bending test suggests that this method was not suitable for our samples. The curved geometry of the bones led to uneven load distribution, which in turn resulted in inaccurate measurements of stiffness and flexural strength. These issues made it clear that the four-point bending test was unsuitable for bones with complex geometries like the femurs and humeri. The three-point bending test, on the other hand, proved to be a reliable method for characterizing the mechanical properties of both 3D-printed PLA samples and potentially real bone tissue. The simplicity of the setup and predictability of the fracture points made this test the preferred method for further mechanical characterization By confirming the reliability of the three-point bending test, we have established a clear protocol for evaluating the mechanical properties of bones.

6.6.1 Preclinical Tests Conclusions

This study compared the three-point and four-point bending tests using 3D-printed PLA samples of feline bones. The three-point bending test emerged

as the more reliable method, offering consistent and accurate data for stiffness and flexural strength. In contrast, the four-point bending test exhibited significant limitations due to asymmetric load distribution and geometric complexities of the samples. The results of this study lay the foundation for guiding future research into the development of patient-specific FEMs and the use of 3D-printed models in preclinical studies, ultimately contributing to improved fracture prediction and prevention in osteoporosis patients. Additionally, these findings support the creation of a standardized protocol to be followed during experimental testing.

6.7   Experimental Tests

Once the three-point bending test was determined to be the most suitable method, we proceeded with the experimental phase. We meticulously extracted four limbs from each feline specimen, specifically two humeri and two femurs, through a precise surgical procedure as shown in Fig. 6.4. These real bone specimens were subsequently subjected to the three-point bending test, adhering strictly to the established protocols outlined in prior preclinical testing. Each bending test was conducted under controlled conditions, and the entire process was recorded with a high-resolution camera, ensuring meticulous documentation of the mechanical response of each bone.

The testing apparatus used for these trials featured the same specifications as those employed in previous preclinical studies, ensuring consistency in the force-displacement analysis. Specifically, the machine operated with a 1kN load cell, set in displacement control mode, as in previous trials. This setup, as shown in Fig. 6.5, ensured accurate force application and measurement, particularly suited for assessing the stiffness and flexural strength of the bones.

Throughout the testing process, the NEXYGENPlus 3.0 software platform was used to continuously monitor and record force, time, and displacement values at each step of the experiment. This allowed for the real-time generation of force-displacement curves shown in Fig. 6.6, in Fig. 6.7 and in Fig. 6.8, which are critical for determining mechanical properties such as stiffness and failure points. The software generated output in the form of Excel files, which provided raw data from the experiments.

6.7.1 Specimen Number and Statistics

For the experimental tests, four real feline limbs were used: two humeri and two femurs. This allowed for a direct evaluation of the mechanical properties of real bone tissue under controlled conditions. The test setup involved three specimens per bone type, ensuring statistical reliability. The number of specimens was sufficient for the initial mechanical characterization of the femur and humerus bones, providing a clear picture of the differences between the two bone types. To further ensure robust and statistically reliable data, power analysis was conducted to assess the adequacy of the sample size. This analysis confirmed that the number of specimens used was sufficient to detect meaningful differences in mechanical properties such as stiffness and flexural strength. The reliability of the measurements was ensured by consistent calibration of the testing equipment, including the 1kN load cell, and by using the NEXYGENPlus 3.0 software platform to monitor force and displacement with high precision. The mechanical parameters, including stiffness, flexural strength, and failure points, were accurately recorded, and the data were used to generate force-displacement curves. These measurements were vital for determining the bone's response to applied loads, allowing for a comprehensive assessment of their mechanical properties.

6.8 Conclusion

In this chapter, we focused on determining the optimal testing setup by comparing three-point and four-point bending tests on 3D-printed PLA models, which were replicas of the actual feline bones. Using PLA models allowed us to evaluate and refine our protocol without risking damage to the actual bone samples, ensuring that the final protocol was both effective and efficient for subsequent clinical testing. The experimental framework included the extraction of humeri and femurs, the application of bending tests, and the subsequent detailed analysis of force-displacement curves. Through these trials, we demonstrated the robustness of the three-point bending test as a reliable method for assessing key mechanical properties such as stiffness and flexural strength, particularly when dealing with non-homogeneous and geometrically complex samples like bones. The symmetrical stress distribution and predictable fracture behavior observed in the three-point test highlighted its effectiveness for bone analysis in both preclinical and biomechanical studies. In contrast, the four-point bending test presented significant limitations due

to asymmetric load distribution and the complexity introduced by the curved geometry of the bones. Although theoretically advantageous for pure bending analysis, this method proved unsuitable for the objectives of this study, often leading to distorted mechanical results that lacked consistent interpretability. The protocol thus established with the three-point bending test was subsequently applied to the actual bone samples, yielding experimental curves from which the mechanical parameters of interest were extracted.
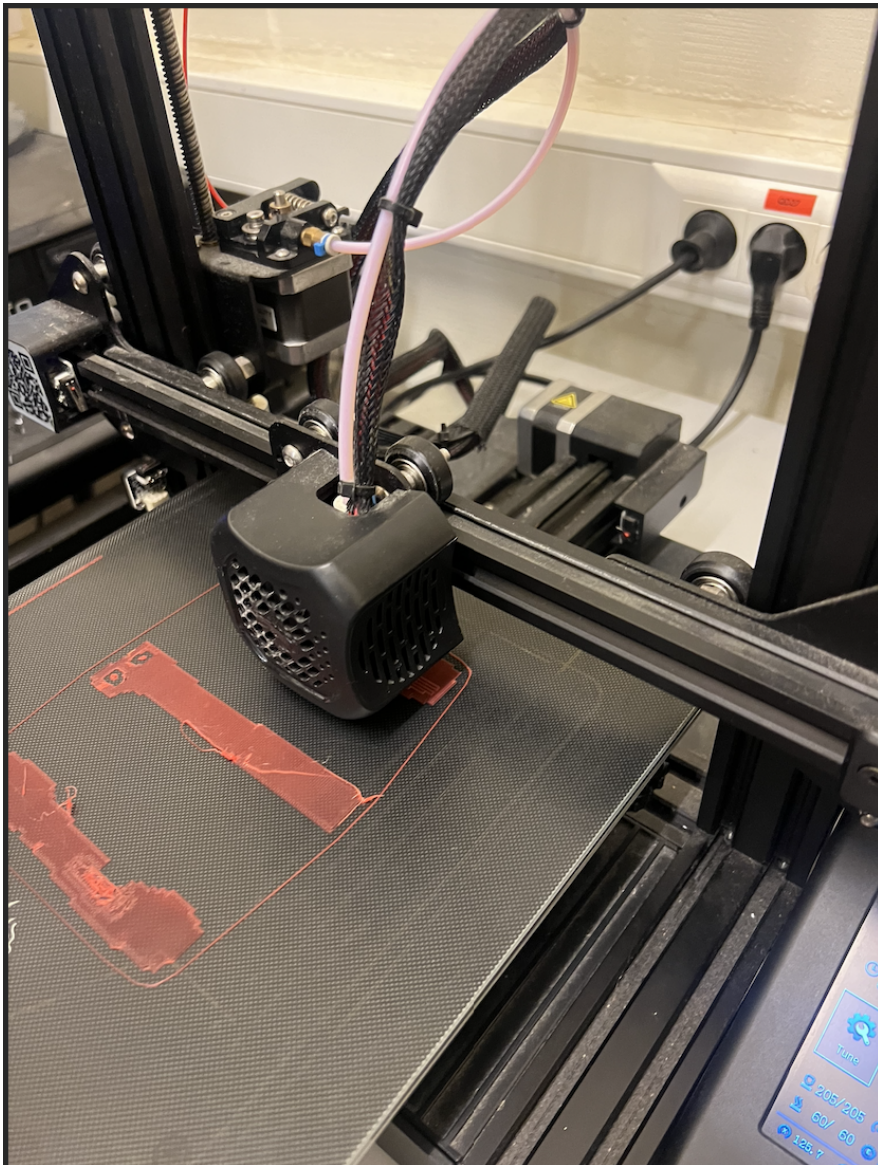
Figure 6.2: 3D printing of PLA samples.
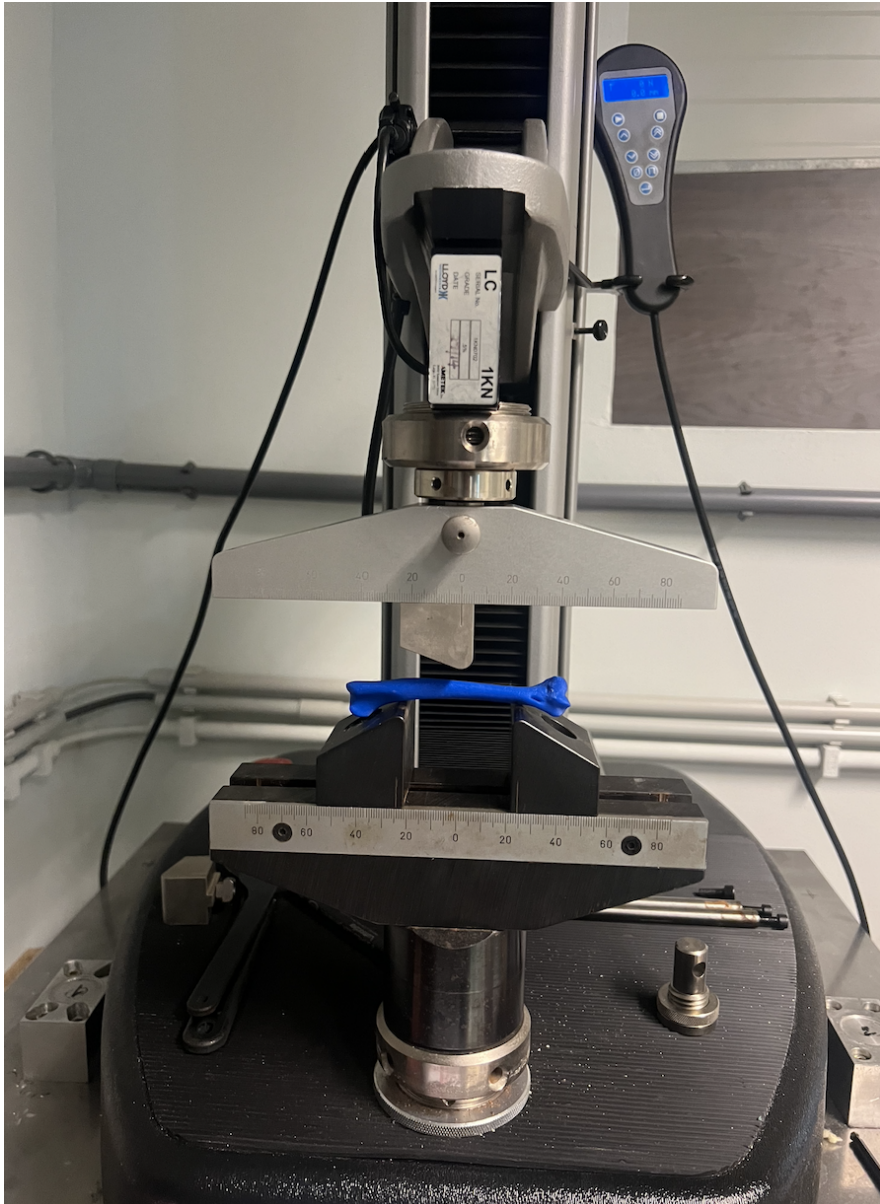
Figure 6.3: Preclinical three-point bending test on PLA samples

Figure 6.4: Surgical extraction of the specimen's limbs for experimental analysis.

Figure 6.5: Clinical test setup illustrating the equipment and configuration used for experimental analysis.

Figure 6.6: Images from the custom-built feature extractor.

Figure 6.7: Images from the custom-built feature extractor.
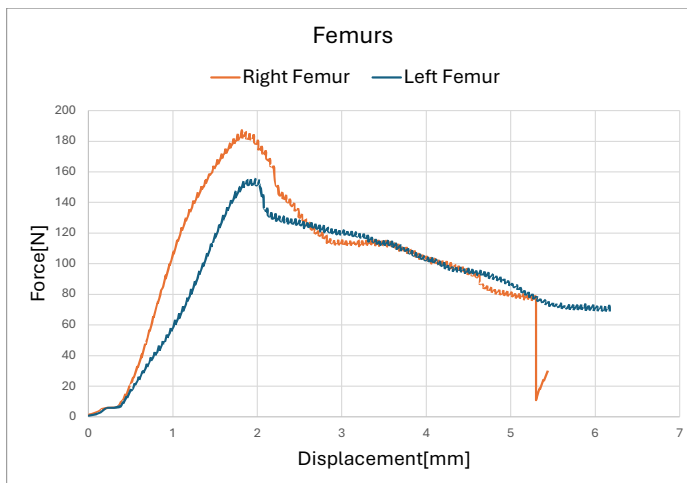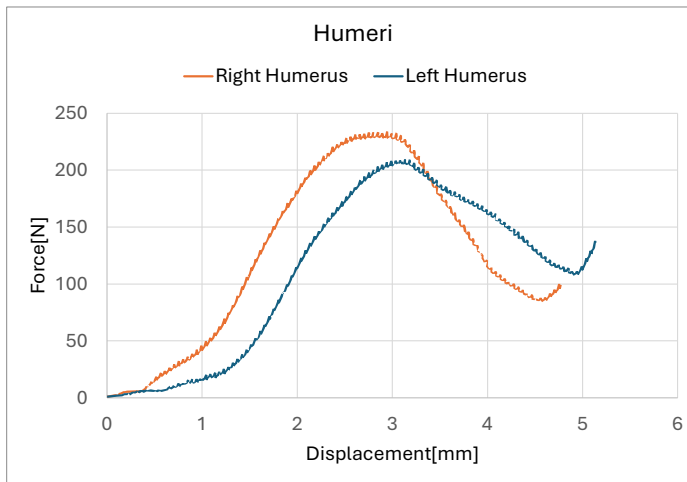
Figure 6.8: Images from the custom-built feature extractor.

Chapter 7

Finite Element Analysis

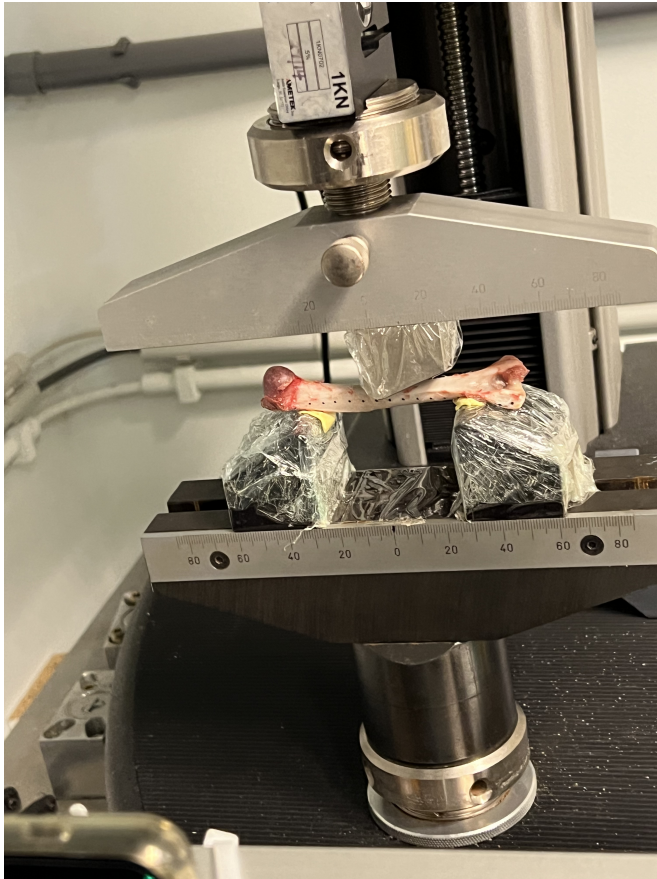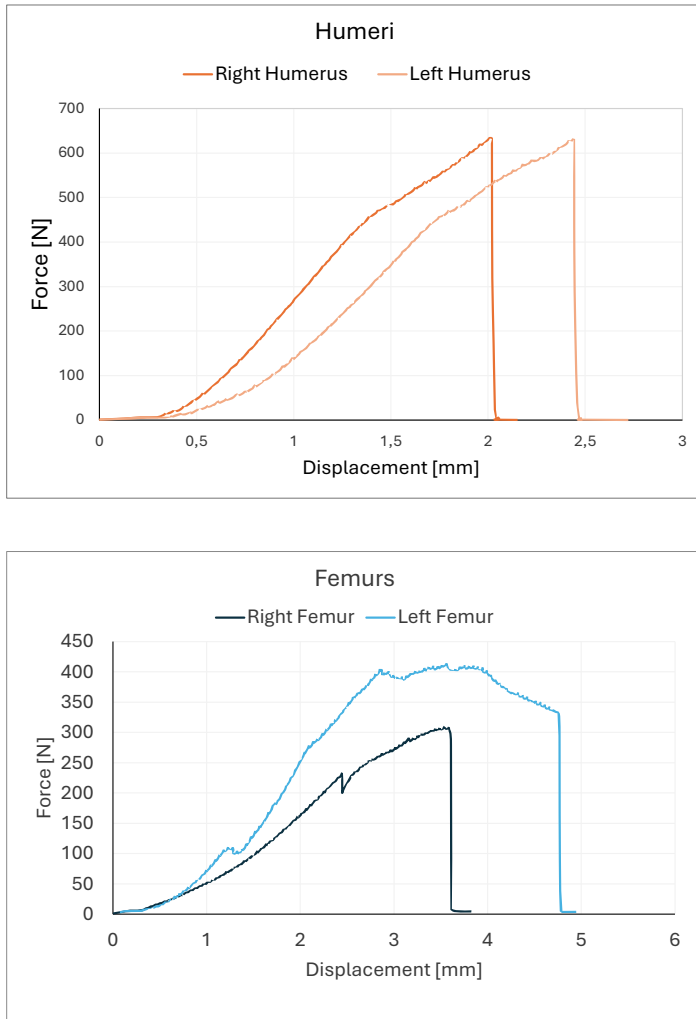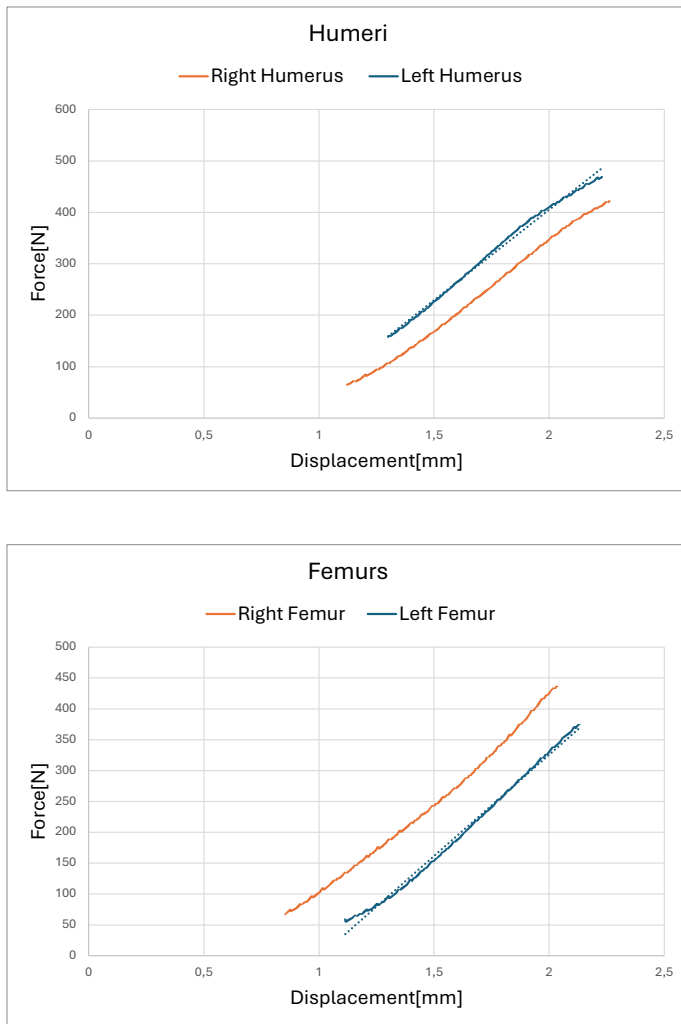*This chapter details the Finite Element Analysis (FEA) conducted to study the mechanical behavior of feline bones. Five different configurations were analyzed, including the one implemented using Bonemat. Each configuration aimed to replicate the experimental conditions and provide a comprehensive understanding of stress distribution and bone response under mechanical loads. The study highlights the differences in setting material properties across the configurations, offering insights into their impact on simulation accuracy and the representation of bone mechanics.*

7.1 Introduction

Finite Element Analysis (FEA) is a critical computational technique extensively utilized in engineering and biomechanics to assess the behavior of structures, materials, and biological tissues under various mechanical conditions. In biomechanics, FEA provides a powerful means to simulate the mechanical response of bones, implants, and prostheses under applied loads, offering insights that would be difficult to capture through physical experiments alone. This method is indispensable for optimizing the design and functionality of orthopedic devices, predicting fracture risks, and understanding complex biomechanical interactions. FEA works by dividing a complex physical structure, such as bone or a prosthetic, into smaller, simpler components called finite elements. Each of these elements is mod-

eled individually, and their behavior under applied forces is analyzed. The collective behavior of all elements is then used to approximate the overall response of the system. This decomposition allows engineers and biomechanists to study structures in fine detail, making it possible to investigate stress concentrations, strain distribution, and displacement patterns that are otherwise hidden within the larger structure. A key aspect of FEA is the meshing process, which involves subdividing the geometry of the structure into a network of elements. This step is essential for solving the system of equations governing the physical behavior of the structure. The mesh's resolution, such as the number of elements, greatly influences the accuracy of the analysis. A finer mesh, with more elements, captures more detailed information about the structure's behavior, but it also requires more computational resources, such as memory and processing time. Therefore, there is a trade-off between precision and computational efficiency that must be carefully managed in biomechanical studies.

7.1.1   Element Types

FEA employs different types of elements to model the structure. The choice of element type affects both the accuracy and computational cost of the analysis:

- **Linear Elements**: These elements are simpler and faster to compute, making them computationally efficient. However, they may struggle to accurately model stress concentrations, particularly around sharp geometries, and are less effective in capturing the complex material behavior in biological tissues, which can exhibit nonlinear characteristics.

- **Quadratic Elements**: These elements provide greater accuracy in modeling stress distribution, especially in regions with curvature or high stress gradients. Quadratic elements are more computationally intensive but yield more precise results, particularly in biomechanical applications where capturing small variations in stress and strain is critical for accurate predictions.

7.1.2   Mathematical Representation and Solution Process

FEA relies on partial differential equations (PDEs) to represent physical processes such as linear elasticity, governed by Hooke's Law. These equations describe the relationships between stress, strain, and displacement within each finite element. By solving these equations, FEA calculates the displacement of each node in the mesh, which is then used to determine other mechanical properties such as stress and strain. The accuracy of the results depends heavily on the quality of the mesh and the type of elements used, as well as the material properties inputted into the model.

The process of solving FEA problems typically follows these steps:

1. **Mesh Generation**: The structure is divided into finite elements, and nodes are defined at key points where the structure is interconnected.

2. **Boundary Conditions**: External forces, displacements, and constraints are applied to the model to simulate real-world loading conditions.

3. **Solution of the System of Equations**: FEA solves for unknowns, such as displacements at each node, by assembling and solving the system of equations that represent each element's behavior.

4. **Post-Processing**: Once the displacements are calculated, they can be used to derive other quantities such as stress, strain, and reaction forces, providing a detailed view of the structure's performance.

7.1.3   Applications in Biomechanics

FEA has proven invaluable in biomechanics, particularly for analyzing the mechanical properties of bones under load, designing prostheses that mimic bone behavior, and assessing fracture risks. It allows for virtual testing of devices and structures in ways that physical experiments alone could not provide. For example, FEA can simulate how different bone models, implants, or prostheses will perform under various loading conditions, enabling engineers and clinicians to make informed decisions about treatment options and implant designs before clinical trials or surgery. Moreover, FEA is essential in the design of orthopedic implants. By simulating how bones and

implants interact under load, engineers can optimize the material choice, geometry, and fit of the implants, improving patient outcomes and reducing the risk of failure. The integration of FEA into preclinical and clinical studies has become a key factor in advancing personalized medicine, particularly for conditions like osteoporosis, where bone strength varies significantly across individuals. By integrating FEA into fracture prediction models, clinicians can better assess fracture risk and tailor treatments to the specific needs of the patient. In conclusion, FEA is a powerful tool that allows for the accurate simulation of mechanical properties and behaviors, making it an indispensable technique in biomechanics, particularly for the analysis of bones, implants, and prostheses. It provides detailed insights into the mechanical response of biological tissues and plays a crucial role in advancing the understanding of bone mechanics, optimizing the design of orthopedic devices, and improving patient care [24, 173].

7.1.4 Application of FEA in Biomechanics

As previously emphasized, bones are inherently complex and anisotropic, with mechanical properties that vary depending on the direction of applied forces. This directional variability means that their behavior changes according to the orientation and nature of the load, necessitating precise modeling to understand their responses under various loading conditions [35, 124]. FEA is highly effective for modeling bones due to its capacity to incorporate their heterogeneous and anisotropic characteristics, enabling realistic predictions of bone behavior under physiological loads, such as walking, running, or jumping. FEA can also be used to evaluate stress distribution within the femur under load or to assess the effects of conditions like osteoporosis, where changes in bone density and microarchitecture alter its mechanical properties and increase fracture risk [129, 162]. Given the various levels of detail required, bones can be studied and modeled through different approaches [33, 152]:

- Isotropic Models: Suitable for initial approximations or when analyzing relatively uniform trabecular bone.

- Anisotropic Models: Provide more realistic simulations for cortical bone, especially in load-bearing situations.

- Transversely Isotropic Models: Capture the directional dependence of

long bones, offering a compromise between model complexity and ac-
curacy.

- Orthotropic Models: Account for variations in all three principal di-
  rections, providing a very high level of detail and accuracy.

Orthotropic models provide the highest level of detail in simulating bone
mechanics by capturing variations across all principal directions. However,
they are also computationally demanding. In this study, we opted for dif-
ferent models, which strike a balance between accuracy and computational
efficiency. These choices allows us to effectively represent the behavior of
long bones without the added complexity of an orthotropic model, which
is more appropriate for highly detailed analyses beyond the scope of this
project.

7.1.5   Steps Involved in FEA of Biological Systems

The first stage in any FEA simulation is creating a digital model of the
structure under investigation. For bone studies, this usually begins with
acquiring high-resolution CT or MRI scans to capture the detailed geom-
etry of the bone [5, 58]. These scans provide a 3D representation, which
is then segmented to isolate regions of interest, such as the cortical bone
(the dense outer layer) and trabecular bone (the porous inner structure).
Accurate segmentation is critical to ensure that each bone region's unique
mechanical properties are properly represented. Once segmented, the model
is converted into a mesh of finite elements, forming the foundation for further
analysis [11, 161]. Following meshing, material properties such as Young's
modulus, Poisson's ratio, and density are assigned to each element. These pa-
rameters are essential as they define each part's response to stress and strain.
In bone modeling, material properties can vary significantly between cortical
and trabecular bone, as well as depending on the direction of force appli-
cation. This variation is managed through material models, from isotropic
(assuming uniform properties in all directions) to anisotropic and orthotropic
models, which better capture bone's directional dependencies. Choosing the
correct model is key to realistic simulation, especially for complex bones
with varying properties across different axes [32, 44, 93, 125]. Next, boundary
conditions are set to simulate natural constraints. These conditions might
represent fixed supports or restraints that mimic how bones are attached to
surrounding structures. For example, in a femur model, the hip joint might

be treated as a fixed support to emulate its connection to the pelvis. Loading conditions are then applied to represent external forces or displacements the bone encounters, such as body weight on the femur during walking, impact forces from jumping, or controlled forces from bending tests in a lab. With geometry, material properties, boundary conditions, and loads established, the FEA solver calculates the solution by solving complex equations for each element in the mesh to determine the structure's response. This process yields a displacement field, showing how each point within the bone moves under applied forces. From this data, essential insights such as stress and strain distributions are derived. The final step is analyzing these results to interpret the structure's behavior. Visualization of stress distributions, strain energy density, and deformation patterns identifies potential fracture-prone areas or regions where implant reinforcements might be needed. This analysis is instrumental not only in understanding bone mechanics but also in applications like surgical planning, implant design, and optimizing treatments for osteoporosis. Through FEA, researchers and clinicians can model complex scenarios, enhancing predictions of biomechanical performance and ultimately advancing orthopedic care and research [79].

7.1.6 FEA in Prosthetics and Orthopedic Implants

FEA is extensively applied in the design and optimization of prosthetic and orthopedic implants. By simulating the behavior of an implant under a range of physiological loads, engineers can refine its structure to ensure it withstands daily activities, or lifting (without transferring undue stress onto the adjacent bone tissue). This design process not only reinforces the durability of the implant itself but also preserves the structural integrity of the patient's bone [121, 148]. Recent advancements in medical imaging technologies, integrated with FEA, have enabled the development of patient-specific models derived from high-resolution CT or MRI scans of the individual's anatomy. These personalized models allow for highly accurate simulations of implant performance post-surgery. This approach is especially valuable in designing hip and knee replacements, where achieving a precise fit between the implant and the patient's unique bone structure is critical to long-term success. Proper alignment of the implant reduces wear over time, subsequently enhancing the patient's mobility and comfort [5, 84, 91, 129]. One of the primary challenges in implant design is addressing the issue of stress shielding. Stress shielding occurs when an implant absorbs a disproportion-

ate amount of the load, which would normally stimulate the surrounding bone. This reduced mechanical stimulation can lead to bone resorption, gradually weakening the bone-implant interface and potentially resulting in implant loosening or failure. FEA is instrumental in countering this problem by enabling engineers to optimize implant designs for a more balanced stress distribution. By adjusting parameters such as geometry, material properties, and implant stiffness, engineers can develop implants that distribute the load more evenly between the implant and the surrounding bone, ensuring adequate stimulation to preserve bone health. This balance not only helps maintain bone density but also extends the implant's lifespan, thereby improving patient outcomes and decreasing the likelihood of revision surgeries [61, 104]. Through the synergy of FEA and patient-specific modeling, significant advancements have been made in the field of prosthetics and orthopedic implants toward developing more effective, personalized solutions. These tools enhance the ability to predict implant performance, resulting in designs that are both structurally resilient and more harmoniously integrated with the patient's biomechanics [114, 160].

7.1.7 Advantages and Limitations of FEA in Biomechanics

FEA presents numerous advantages, particularly in the study of bone mechanics and implant design, due to its non-invasive nature. One of the primary benefits of FEA is that it enables researchers to investigate the mechanical properties of biological tissues and implants without the need for physical experimentation, which can be both time-intensive and costly. This non-destructive approach is especially valuable when handling delicate or rare specimens that may not withstand experimental testing. Another significant advantage of FEA lies in its adaptability. Models can be customized to reflect the specific geometries and conditions of individual patients, facilitating the development of personalized treatments. This customization makes FEA an essential tool in designing implants that conform precisely to a patient's anatomy, thereby improving surgical outcomes, particularly in orthopedic procedures such as hip and knee replacements. Additionally, FEA is renowned for its predictive capabilities. It can simulate how bones and implants will respond under various loading conditions, offering crucial insights into areas such as fracture risk and implant performance. This predictive power allows clinicians and engineers to anticipate potential

issues, such as regions of high stress or mechanical weakness, before any surgical intervention takes place. Despite these strengths, FEA has notable limitations. One of the main challenges is its computational demand. High-resolution models with fine meshes that capture intricate details require substantial computational power and time, making FEA both time-consuming and costly, especially for extensive or highly detailed analyses. Furthermore, FEA models often necessitate simplifications to manage complexity. Although FEA can simulate complex behaviors, these simulations frequently depend on assumptions or simplifications regarding material properties or boundary conditions, which can sometimes limit the accuracy of the results. Such approximations may not fully capture the nuanced behavior of biological tissues [71, 129]. Lastly, the accuracy of FEA simulations heavily relies on the precision of assigned material properties. Accurately determining values such as Young's modulus, Poisson's ratio, and density for biological tissues poses a challenge due to natural inter-individual variations and changes associated with age or disease. Any inaccuracies in these properties can significantly affect the reliability of simulation outcomes. In conclusion, while FEA is a powerful and versatile tool for analyzing bone mechanics and designing implants, its efficacy depends on careful model preparation, adequate computational resources, and precise material characterization. These factors must be managed thoughtfully to maximize the potential of FEA in biomedical applications [18, 105].

7.2 Abaqus

Abaqus is among the most widely utilized software packages for FEA, especially in biomechanics and engineering simulations. Developed by Dassault Systémes as part of the SIMULIA suite, Abaqus is highly regarded for its capability to simulate the complex mechanical and structural behavior of materials under various loading conditions. Its versatility, combined with the capacity to model a broad spectrum of materials, from metals to biological tissues, makes it an indispensable tool in both research and industry [138, 143]. In biomechanics, Abaqus is especially valued for its ability to handle non-linear materials and large deformations, making it ideal for modeling biological tissues such as bone, cartilage, and ligaments. It is frequently employed in orthopedic and biomedical engineering to simulate bone behavior under mechanical loading, evaluate the performance of im-

plants and prosthetics, and predict fracture risks under diverse physiological conditions [129, 148]. The software's extensive material model library includes isotropic, anisotropic, transversely isotropic, and orthotropic models, allowing for precise simulation of the distinct mechanical properties of biological tissues. This flexibility enables users to define material responses to stress, strain, and time-dependent phenomena like creep and viscoelasticity, crucial for understanding the long-term behavior of biological structures and implants. A key strength of Abaqus is its capacity for non-linear analysis, which is essential in replicating real-world conditions. Biological materials often exhibit non-linear stress-strain relationships, particularly under significant deformations [5, 162]. Abaqus effectively captures these non-linearities and supports the modeling of hyperelastic, viscoelastic, and poroelastic materials, making it well-suited for tissues such as skin, tendons, and cartilage. Additionally, Abaqus includes sophisticated contact modeling capabilities, allowing for the simulation of interactions between bones and implants or between soft tissues and prosthetics. The software's dynamic analysis capabilities enable the study of time-dependent mechanical responses to transient loads encountered during activities like walking, jumping, or impact events. With solvers that handle both implicit and explicit dynamic analyses, Abaqus adapts to a wide range of simulation needs [91, 145]. In recent years, patient-specific simulations have emerged as a focus in biomechanics research and clinical applications. Abaqus integrates seamlessly with medical imaging data, such as CT and MRI scans, to create accurate 3D models of patient anatomy. These models can be meshed and subjected to FEA to predict how bones or soft tissues will respond to different loads, thereby enhancing the precision of surgical planning and the customization of implants. The ability to import geometries from DICOM images or STL files, segment these models, and assign heterogeneous material properties to different anatomical regions makes Abaqus a powerful tool for personalized medicine. This feature allows clinicians and researchers to simulate various treatment scenarios, such as evaluating the performance of a hip or knee implant, before surgery takes place, thereby improving patient outcomes. Abaqus also offers a high degree of customization, with advanced modeling capabilities through Python scripting. This enables users to automate repetitive tasks, develop complex parametric models, and extend the software's functionality beyond standard features. Python scripts allow for the definition of custom loading conditions, automated mesh generation, and

detailed post-processing of results to extract specific data related to stress, strain, or displacement at any point in the model [6, 65]. Moreover, Abaqus supports the development of user-defined material models (UMAT), allowing researchers to implement specific constitutive laws or material behaviors not included in the standard material library. This is particularly valuable in biomechanics, where experimental materials like biocomposites or tissue-engineered constructs may possess unique properties. An essential aspect of using Abaqus in both biomechanics and engineering is the validation and verification of simulations. Abaqus facilitates rigorous validation techniques through comparisons with experimental data, ensuring that models accurately reflect real-world behavior. Verification is achieved by comparing the numerical results of a model against analytical solutions or simpler models to confirm the accuracy of the computational setup [114, 131]. This robust process of validation and verification ensures that FEA simulation results can be reliably applied in clinical and engineering contexts, establishing Abaqus as a trusted tool for predicting biomechanical system performance and assessing the structural integrity of engineered components.

7.3   Model Implementations

In this project, we set out to model the mechanical properties of feline bones using Abaqus software, developing four distinct models: two isotropic and two transversely isotropic. Among the isotropic models, one utilized values derived from the literature, while the other was specifically adjusted to better align with our experimental observations. Similarly, the transversely isotropic models included a literature-based version and a customized model, both designed to capture the directional dependencies inherent in bone behavior. Additionally, we incorporated a model using Bonemat, which will be detailed in subsequent sections. This Bonemat model aimed to enhance simulation accuracy by integrating spatially variable mechanical properties based on the internal structure of the bone. These models were applied to the limbs of three feline specimens, enabling us to compare their performance, evaluate their accuracy, and assess their capability to simulate real bone structures under mechanical stress.

Our ultimate goal was to derive mechanical insights from models that closely replicate the experimentally observed behavior of bones. This analysis is essential for obtaining detailed mechanical properties, which will subsequently

be correlated with radiomic features, providing a comprehensive understanding of the mechanical behavior and structural characteristics of feline bones.

7.3.1   Isotropic Model

The isotropic model assumes uniform mechanical properties in all directions, simplifying the simulation but failing to capture the true complexity of bone behavior. We based the isotropic model implemented in Abaqus on data from Gibson et al. ([49]), which reported a Young's modulus of 5004 MPa for feline femurs, derived from mid-diaphyseal compression tests on mature cat cadavers. This value provides a reliable estimate of bone stiffness under compressive forces. The Poisson's ratio was set to 0.3, a common choice for isotropic materials. This value is suitable because it represents the degree to which a material contracts in directions perpendicular to the applied force. For isotropic materials, Poisson's ratio must be below 0.5 to satisfy physical constraints, as higher values would violate the assumptions of isotropy. This choice reflects a balance between material compressibility and elasticity, making it appropriate for approximating cortical bone behavior [167].

To summarize, we set the following parameters:

- Young's Modulus (E): 5004 MPa

- Poisson's Ratio (ν): 0.3

- Density: For the density of feline cortical bone, we referenced literature sources, which suggest values around $1.91E^{-}09 \; \frac{kg}{m^3}$ [92].

While the isotropic model offers a simplified representation, it does not account for the directional dependency of bone's mechanical properties. The mechanical response of bone, especially in long bones like the femur, is highly dependent on the orientation of forces relative to the bone's structural axes. Therefore, although this model is computationally efficient, it is limited in accurately reflecting real-world bone mechanics under complex loading conditions.

7.3.2   Transversely Isotropic Model

The transversely isotropic model, a more sophisticated approach, acknowledges that bone exhibits different mechanical properties along its longitudinal axis (aligned with the osteons and collagen fibers) compared to the

transverse plane. This model is particularly relevant for long bones like the femur, where axial and tangential forces differ significantly. For the transversely isotropic model, we used values derived from human studies [39], scaled down to match the mechanical properties of feline bone. The reference values from human studies were as follows:

- Axial Young's Modulus (E1): 17000 MPa

- Tangential Young's Modulus (E2, E3): 11500 MPa

These values were adjusted using the ratio between the isotropic Young's modulus of human and feline bones to ensure an accurate representation of the mechanical behavior of the feline femur under various loading conditions. Given that the isotropic Young's modulus for human bone is 16600 MPa [28], compared to 5004 MPa for feline bone, this ratio was utilized to adjust and estimate the corresponding values for the transversely isotropic model of feline bones.

- Axial Young's Modulus (E1): $\frac{5004}{16600} = \frac{x}{17000} = 5127$ MPa

- Tangential Young's Modulus (E2, E3): $\frac{5004}{16600} = \frac{x}{11500} = 3470$ MPa

For the transversely isotropic model, we set different Poisson's ratios for the two directions:

- ν_{12}, ν_{13} (longitudinal to transverse): 0.3 (same as in the isotropic model)

- ν_{23} (within the transverse plane): 0.5

The shear moduli, which quantify a material's resistance to shear deformation, were calculated using the following formulas, based on the Young's modulus values and Poisson's ratios:

$$G_{12} = \frac{E_1}{2(1 + \nu_{12})} = 1972 MPa$$

$$G_{13} = \frac{E_1}{2(1 + \nu_{13})} = 1708 MPa$$

$$G_{23} = \frac{E_2}{2(1 + \nu_{23})} = 1156 MPa$$

To summarize, we set the following parameters:

- Axial Young's Modulus E1: 5127 MPa

- Tangential Young's Modulus E2, E3: 3470 MPa

- Poisson's Ratio: ν_{12}, ν_{13}: 0.3 and ν_{23} : 0.5

- Shear Moduli: G_{12}: 1972 MPa, G_{13}: 1708 MPa, G_{23} 1156 MPa

- Density: 1.91 E^{-09} $\frac{t}{mm^3}$

7.4   Tailored Models

In addition to the isotropic and transversely isotropic models discussed earlier, tailored models provide a more granular approach to understanding the mechanical behavior of bone. These tailored models-one isotropic and one transversely isotropic - were developed to account for the specific variations in bone properties across different regions of the bone. This more sophisticated modeling approach ensures that the inherent heterogeneity of bone is captured, allowing for more precise simulations and analyses of its mechanical properties.

7.4.1   Tailored Isotropic Model

The tailored isotropic model was designed to reflect regional variations in the density and stiffness of the bone, enhancing simulation accuracy by incorporating data from Schileo et al. (2008) [130]. Unlike the literature-based isotropic model, which assumes homogeneity across the bone, the tailored isotropic model considers local variations, offering a more detailed representation of the bone's mechanical characteristics.

Once segmented the specific ROIs, particularly focusing on the cortical bone, which plays a critical role in load-bearing and overall mechanical integrity, Hounsfield Units (HU) were calculated for each pixel within the segmented volume. The HU value is crucial in radiology for quantifying the density of tissues, and in this case, it was directly correlated with bone density. The HU value for each pixel was calculated using the standard formula:

HU =Pixel Value * Rescale Slope + Rescale Intercept

This calculation provided a voxel-by-voxel map of the bone's radioden-sity, offering insight into its material composition. Following the calculation of HU values, the next step was to derive the bone density. This calculation involved dividing the mass of each specific bone by its volume, derived from the segmented data in 3D Slicer. For samples one and two, the mass values ranged from 10.1 grams to 12.6 grams. In contrast, sample three consistently showed smaller mass values, between 3.1 grams and 3.9 grams, likely due to its smaller physical dimensions. The formula used was:

$$\rho = \frac{massofbone}{volumeofbone}$$

From this, the apparent density, which is required for the calculation of the elastic modulus, was determined using the following formula:

$$\rho_{app} = a + b + averagedHU$$

Where:

- a = 0.0210 (an empirical constant related to bone stiffness [130, 136]).

- b = 0.000786 (a constant from literature [130, 136]).

These coefficients describe the linear relationship between bone density (as inferred from HU values) and the Young's modulus, ensuring that the elastic properties of each element were tailored to its local material composition. With the density values in hand, the Young's modulus (E) for each voxel was calculated using a linear relationship between bone density and stiff-ness. The formula used to compute E was derived from empirical studies and is given by:

$$E_{app} = 10500 * \rho_{app}^{2.29} \; [130, 136]$$

This relationship allowed for the elastic modulus to be computed for each voxel in the segmented cortical bone, resulting in a spatially varying modulus that reflects the actual heterogeneity of bone tissue. The specific value of E for each region of the bone was then used in the finite element analysis to sim-ulate mechanical behavior under load. By employing the tailored isotropic

approach, significant variations in bone stiffness were observed across different regions of the bone. These findings indicate that the bone's mechanical behavior cannot be accurately captured by a homogeneous isotropic model, as it neglects the inherent material heterogeneity. The tailored isotropic model, therefore, provides a more realistic representation of bone mechanics, particularly for use in load-bearing simulations.

7.4.2 Tailored Transversely Isotropic Model

The tailored transversely isotropic model takes the concept of heterogeneity one step further by accounting not only for the spatial variation in mechanical properties but also for the anisotropy of bone. In long bones, the mechanical properties vary significantly along the longitudinal axis compared to the transverse plane. The tailored transversely isotropic model reflects these variations, providing a highly accurate representation of bone behavior. To accurately model the anisotropic nature of bone, the bone was divided into five distinct volumes along its longitudinal axis. This division allowed for the modeling of different mechanical properties in each volume, thereby capturing the varying stiffness and density along the bone. Each of these five volumes represented a specific section of the bone, with its own distinct material properties. The same process done for the isotropic model, was repeated for each of the five volumes, resulting in a longitudinally varying elastic modulus, with each region of the bone having a specific value of E based on its material properties. Formulas were taken from the same references as the isotropic model [130, 136]. For each voxel within these five volumes, the HU values were calculated using the same formula as before:

HU = Pixel Value * Rescale Slope + Rescale Intercept

These HU values were then converted into density values for each voxel, using the same process outlined for the isotropic model. For each of the five segmented volumes, also the Young's modulus (E) was calculated using the same relationship between density and stiffness: $\rho = \frac{mass\,of\,bone}{volume\,of\,bone}$

From this, the apparent density, which is required for the calculation of the elastic modulus, was determined using the following formula:

$\rho_{app} = a + b + averaged HU$

Where:

- a = 0.0210 (an empirical constant related to bone stiffness)

- b = 0.000786 (a constant from literature)

The formula used to compute E was derived from empirical studies and it is the same as the isotropic model given by:

$$E_{app} = 10500 * \rho_{app}^{2.29}$$

7.4.3   Summary of Tailored Model Results

The tailored isotropic and transversely isotropic models provided a much more detailed representation of bone mechanics than the homogeneous models. By accounting for local variations in density and stiffness, these models captured the heterogeneity and anisotropy of bone more accurately. The tailored transversely isotropic model, in particular, proved to be highly effective in simulating the varying mechanical properties along the bone's axis, making it the most realistic representation of bone behavior under loading conditions. The detailed analysis of each voxel's mechanical properties-whether isotropic or transversely isotropic-demonstrates the critical importance of accounting for bone's complex material structure in finite element simulations. These tailored models form the basis for more accurate predictions of bone behavior, aiding in the development of better biomedical applications such as implants and prostheses.

7.5   Bonemat

The final model implemented in this study employed the Bonemat software, which automates the process of assigning spatially varying mechanical properties to a bone's finite element model based on medical imaging data [131]. By using Bonemat, it was possible to define element-specific Young's modulus values throughout the bone, making the simulation highly detailed and region-specific. This approach is critical for improving the accuracy of biomechanical simulations, as it reflects the heterogeneous nature

of bone tissue. Bonemat is a specialized software tool designed to integrate mechanical properties of bone into finite element models based on computed tomography (CT) data. It is particularly useful for biomechanical simulations, as it allows for the calculation of Young's modulus for each element in a meshed model, based on the local HU values derived from CT scans. This voxel-based approach ensures that the mechanical properties of the bone are accurately represented across its entire structure, reflecting the heterogeneity of bone tissue. It works by mapping the HU obtained from DICOM images onto a finite element mesh and uses empirical relationships between HU values and material properties to assign a specific Young's modulus to each element. This allows for spatially varying elastic moduli within the same bone, providing a more realistic simulation compared to models that assume homogeneous material properties [131, 146].

To incorporate Bonemat into the workflow for your study, the following steps were taken:

Step 1: Preparing the Bone Models in Abaqus

The process began with the creation of finite element models of the bones (specifically the humeri and femurs). Using Abaqus, the bones were imported as 3D geometries and meshed to define their structural elements. Meshing divides the bone geometry into smaller, discrete elements, each of which can be assigned specific mechanical properties.

Step 2: Exporting the Mesh for Bonemat

Once the bones were meshed in Abaqus, the meshed version of the bones was exported from Abaqus in a format compatible with Bonemat. This exported mesh served as the foundation for applying spatially varying mechanical properties in Bonemat.

Step 3: Importing the DICOM Files and Meshed Bone into Bonemat

After importing the bone models meshed in Abaqus, the corresponding DICOM images of the bones were also imported into Bonemat. These DICOM files provided the CT scan data, containing the HU values, which are critical for mapping mechanical properties onto the finite element mesh. In Bonemat, the DICOM files were registered with the finite element mesh to ensure

proper alignment and scaling. This step ensured that the HU values from the CT images corresponded correctly to the specific regions of the bone mesh.

Step 4: Assigning Mechanical Properties Using Bonemat

With the mesh and DICOM data loaded, Bonemat was used to automatically assign Young's modulus to each element in the mesh, based on the local HU values of the corresponding region in the CT data. Bonemat uses the following general relationship to assign material properties we used in our tailor models:

$$\rho = \frac{mass of bone}{volume of bone}$$

From this, the apparent density, which is required for the calculation of the elastic modulus, was determined using the following formula:

$$\rho_{app} = a + b + averaged HU$$

where a and b were assigned the same values [131, 146] used in our tailored models:

- a = 0.0210

- b = 0.000786

were applied, as these had been previously validated in the tailored models used earlier.

Step 5: Generating the INP File

Once Bonemat had assigned the mechanical properties to each element, the software produced an INP file (a file format used by Abaqus for input data) that contained the element-wise material definitions. This file specified the Young's modulus for each element in the mesh, based on the HU-derived density values.

Step 6: Importing the Bonemat Results into Abaqus

The INP file generated by Bonemat was then imported back into Abaqus. This file provided Abaqus with the updated mechanical properties for each element, effectively "bonemating" the bones. At this stage, each element in the finite element model had a specific Young's modulus assigned, reflecting the actual spatial heterogeneity of the bone's material properties.

7.5.1 Finite Element Analysis in Abaqus with Bonemat Data

Once the bones were bonemated and reimported into Abaqus, the standard FEA procedures, shown in the next paragraphs, were applied. This included applying boundary conditions and external forces to simulate the mechanical behavior of the bones under various loading scenarios, such as three point bending.

By using Bonemat, the finite element model gained a new level of accuracy, particularly in simulating bone's complex, anisotropic behavior. This model was able to account for the localized variations in bone density and stiffness, providing a more realistic representation of how bones respond to mechanical forces in vivo.

Summary of Bonemat Results

The integration of Bonemat with Abaqus in this study allowed for the creation of a highly detailed, element-wise finite element model of the bones. By assigning Young's modulus values based on local HU data, the mechanical properties of each bone element were tailored to reflect the actual material composition of the bone. The resulting simulations provided a more accurate and realistic representation of the bones' mechanical behavior under load, contributing to a deeper understanding of their biomechanical properties.

7.6 Abaqus Model Parameters

The finite element simulations conducted in Abaqus were fundamental to understanding the mechanical behavior of the feline bones under bending loads. By implementing various material models and carefully replicating experimental conditions, the study aimed to compare the performance of

different configurations, including isotropic, transversely isotropic, and tailored models. Below, we outline the setup and methodology used in Abaqus, highlighting the parameters, boundary conditions, and loading mechanisms that were crucial for ensuring realistic simulations. To accurately capture the intricate geometry of the feline femurs and humeri, the bones were meshed using tetrahedral elements. They conform well to the organic and non-linear structure of the bone and are widely used in biomedical simulations due to their versatility in handling complex anatomical shapes. Given that bone surfaces are highly irregular and organic, they provided the flexibility needed for an accurate representation. A global mesh size of 2mm was chosen. This size represents a compromise between computational efficiency and the accuracy required to simulate local stress concentrations, particularly around the support and load points in bending tests. Meshing is a crucial step in FEA since it directly influences the accuracy of stress and strain calculations. The chosen mesh size allowed for an adequate resolution to model the mechanical response without excessive computational overhead. In regions expected to undergo significant stress concentration, such as the areas around the loading and support points in the three-point bending test, local mesh refinement was applied. This ensured that the model could capture stress peaks and deformations with higher precision in these critical areas.

Isotropic Material Model

In the isotropic model, the mechanical properties of the bone were assumed to be identical in all directions. While bones exhibit anisotropic behavior in reality, this simplification is often used when a more generalized mechanical response is acceptable. For completeness, the values assigned to the mechanical properties are provided here, even though their derivation was discussed in previous paragraphs.

- Young's Modulus (E): A value of 5004MPa was used for feline bones.

- Poisson's Ratio (ν): The Poisson's ratio was set to 0.3, a standard value for isotropic materials, which reflects the ratio of lateral strain to axial strain under uniaxial loading as already explained in the previous paragraphs.

As already mentioned, Poisson's ratio represents how much a material will expand or contract in the directions orthogonal to an applied load. A value of

0.3 is typical for cortical bone when modeled as isotropic, balancing the need to represent bone's compressibility while maintaining mechanical integrity under load.

Transversely Isotropic Material Model

The transversely isotropic material model was applied to account for the directional dependence of bone properties, particularly along the longitudinal axis (the direction in which bones bear weight). As explained previously, given that the isotropic Young's modulus for human bone is 16600 MPa [28], compared to 5004 MPa for feline bone, this ratio was utilized to adjust and estimate the corresponding values for the transversely isotropic model of feline bones. The reference values for humans were:

- Young's Modulus (E1): 17000 MPa was applied along the axial direction (longitudinal axis).

- Young's Modulus (E2 and E3): 11500 MPa for the transverse and tangential directions, reflecting the reduced stiffness of the bone when loaded perpendicular to the longitudinal axis.

In this model, the bone was considered to have different mechanical properties along its primary axis compared to its perpendicular directions, better reflecting the anisotropic nature of real bone, particularly in load-bearing scenarios. By rescaling the values derived from human data, we established the coefficients for the feline specimens. Below are the reported values of all the set coefficients, along with the final values for E (Young's modulus):

- Axial Young's Modulus E1: 5127 MPa

- Tangential Young's Modulus E2, E3: 3470 MPa

- Poisson's Ratio: ν_{12}, ν_{13}: 0.3 and ν_{23} : 0.5

- Shear Moduli: G_{12}: 1972 MPa, G_{13}: 1708 MPa, G_{23} 1156 MPa

- Density: 1.91 E^{-09} $\frac{t}{mm^3}$

Tailored Models (Isotropic and Transversely Isotropic)

For the tailored models, we extracted specific material properties by segmenting the bone and calculating HU values for each pixel. From these

values, we calculated the density and then the corresponding Young's modulus for each voxel, allowing for a more precise representation of the bone's mechanical properties. The bone density was calculated by measuring the bone's mass and dividing it by the volume, which was obtained using 3D Slicer. This process gave us a specific density for each of the segmented bones. In the transversely isotropic tailored model, the bone was divided into five distinct volumes along its length. For each volume, HU values were calculated, and the corresponding Young's modulus was assigned based on these local densities. This model allowed for a more detailed representation of how bone stiffness changes along its length, especially in regions that bear varying levels of mechanical load.

Bonemat Models

Specific steps were performed in Bonemat after meshing the bones in Abaqus, as explained in the previous paragraphs. After processing in Bonemat and reimporting into Abaqus, the model settings remained consistent with those of the other models.

7.6.1   Boundary Conditions and Load Application

In the three-point bending test simulation, shown in Fig. 7.1 the following conditions were applied to replicate the experimental setup:

- Support Pins: These were modeled using encastre boundary conditions, fully constraining all degrees of freedom (DOFs) to ensure they remained stationary throughout the test. This setup prevents any movement or rotation, simulating a fixed support condition.

- Displacement Constraints: The load pin was assigned a displacement boundary condition along the y-axis, with a displacement value CF2=−1, to simulate the applied force direction during the bending test. While the two support pins are fully fixed, the load pin is allowed to perform both translations and rotations as needed to mimic real-world conditions.

- Interactions: A general contact interaction with a friction coefficient of 0.3 was used to manage the contact between model components, particularly between the bone and the pins. This friction value simulated

the resistance during the test, impacting how the bone slid or adhered to the supports.

- Global Property Assignment: The friction coefficient of 0.3 was incorporated into the global property settings to ensure accurate simulation of surface interactions during the loading process.

- Force-Controlled Loading: A force was applied along the -y direction at the center of the bone to replicate the bending load in line with the experimental procedure.

- Rationale for Force-Controlled Load: Since the experimental setup applied force directly rather than displacement, using force-controlled loading in the simulation ensured consistency with the real test conditions, allowing for more accurate comparisons of mechanical properties such as stiffness and yield strength.

- Amplitude: The force amplitude in the simulation was derived from experimental force-displacement curves, ensuring that the applied load followed the same trend as observed in the tests. This alignment provided a realistic basis for comparing the mechanical response of the bone

The interaction properties were crucial for simulating how the bone slid or stuck to the supports during loading, affecting stress distribution at the contact points.

7.7   Conclusion

This chapter outlined the detailed setup of finite element simulations for bone biomechanics using Abaqus. By integrating isotropic, transversely isotropic, and tailored models, the simulations provided a comprehensive understanding of how bones respond to bending loads under different material assumptions. Through careful meshing, the use of force-controlled loading, and precise boundary conditions, the simulations closely mirrored the experimental three-point bending tests. Furthermore, the application of Bonemat allowed for the assignment of highly accurate material properties, reflecting the true heterogeneity of the bones. This approach not only enhanced the predictive power of the simulations but also provided valuable insights into the
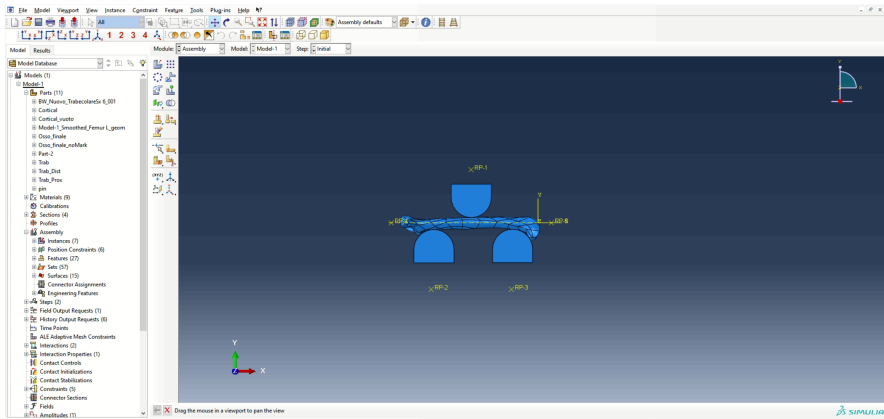
Figure 7.1: Abaqus Setting

mechanical behavior of bones, which can be applied to improve orthopedic treatments and implant designs.

Chapter 8

Mechanical Parameter Extrapolation

This chapter outlines the detailed methodology employed in analyzing the force-displacement data obtained from FEA models, with a specific focus on rigidity and elastic modulus. This step-by-step process allowed for the standardization of results, enabling a meaningful comparison between different model configurations.

8.1 Introduction

After completing the analysis, we obtained force-displacement curves for each model and each specimen, resulting in a total of 55 models. However, to effectively compare these models, it was necessary to recalibrate them and align their reference points, ensuring a consistent zero point for comparison. This step was crucial for normalizing the results and enabling a meaningful evaluation of the mechanical behavior across all models. The objective of this analysis is to identify a mechanical parameter that can be meaningfully associated with radiomic features. This would enable a deeper understanding of the relationship between mechanical properties and radiomic characteristics, offering new insights into bone behavior.

8.2   Methodology for Rigidity and Elastic Modulus Analysis

The importance of these steps lies in ensuring that the models accurately reflect the mechanical properties of the material under study. In the process of analyzing the mechanical behavior of feline bones through Finite Element Analysis (FEA), it was essential to establish a method for comparing different model configurations accurately. Given the inherent variability in the material properties and mechanical responses of biological tissues, a standardized approach was required to ensure that each model could be meaningfully compared. This led to the derivation and implementation of a specific elastic modulus, denoted as E^*, which played a crucial role in the calibration and subsequent comparison of the models

8.2.1   Extraction of Force-Displacement Data from FEA Models

The initial step involved extracting force displacement curves from the simulations of each model. These curves provide a fundamental insight into how each model responds to applied loads, capturing the relationship between the force exerted on the specimen and the resulting displacement. For each of the 55 models analyzed, a linear interpolation was applied to these curves to calculate the angular coefficient, known as rigidity (k), which represents the stiffness of the material. As an example, this chapter presents the curves obtained at each step for the left femur of the Black-and-White specimen. Fig. 8.1 presents the force-displacement curves and their corresponding linear interpolations for the left femur of the Black-and White specimen in all the four configurations, highlighting the differences in rigidity across various them. To have a complete overview of the different approaches, in Fig. 8.2 is shown the force-displacement curve obtained from the FEA model, incorporating mechanical properties assigned using Bonemat to the left femur of the black and white specimen. In practice, this process, along with those described below, was performed for all samples, ensuring a comprehensive analysis of each configuration. The interpolation executed for all the samples in all different configurations, allowed for a thorough comparison across specimens.
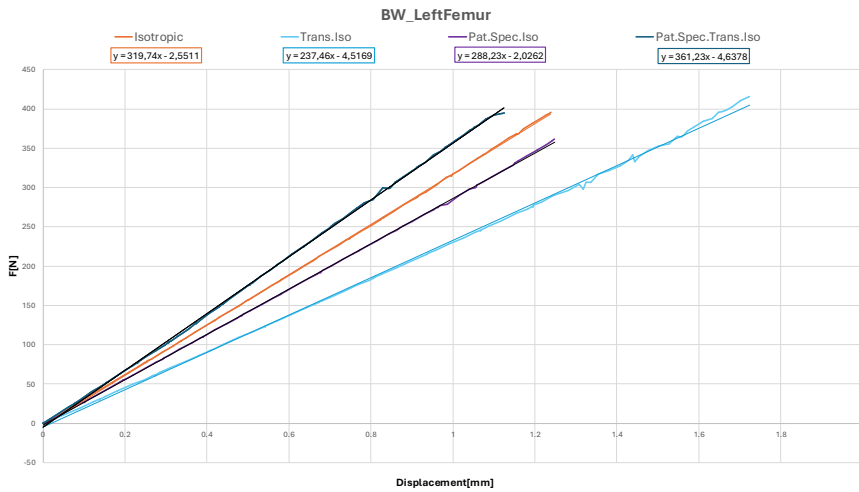
Figure 8.1: Linear interpolation for the four cases of the Black-and-White Left Femur

8.2.2 Standardization through Scaling

Linear interpolation provides a means of approximating the relationship between force and displacement using a straight line, which is particularly useful for determining the stiffness of the material as shown in Fig. **??** [25]. The general mathematical relationship governing these force-displacement curves is expressed as:

$F = k * d + b$ ([59])

Where:

- F is the applied force,

- d is the resulting displacement,

- k is the slope of the curve, which represents the rigidity of the material.

- b b is the intercept, indicating the force when displacement is zero.

These curves are foundational for understanding how the material resists deformation, with the slope (k) indicating the stiffness or rigidity of the model. Rigidity is a critical mechanical property and serves as the primary focus of the subsequent analysis.
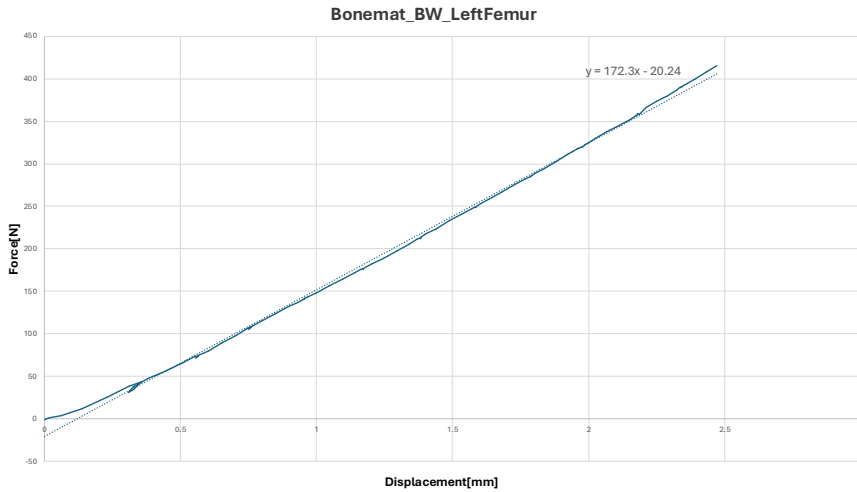
Figure 8.2: force-displacement curve obtained from the FEA model, incorporating mechanical properties assigned using Bonemat of the left femur of the black and white specimen.

8.2.3   Derivation and Application of E^*

The standardized rigidity (k) and the scaled elastic modulus (E) were then used to derive a new elastic modulus, E^* for each model. It represents a recalibrated measure of elasticity that accounts for both the mechanical response observed through the force-displacement curves and the initial material properties set in the FEA simulations. This derivation was performed through interpolation, creating a relationship between rigidity and elastic modulus that allowed for the adjustment of E to E^*. To ensure consistency in the comparison process, both the calculated rigidity (k) and the elastic modulus (E) were scaled by a factor of 0.9. This scaling step allowed for the standardization of the results, ensuring that any subsequent comparisons between models would be based on a uniform reference point. The scaling factor was applied uniformly across all models, providing a basis for recalibrating the results in a way that aligned their reference points to a common zero. Once $E^*$was determined, it was reintroduced into the FEA models, replacing the original elastic modulus values. The models were then re-run using these adjusted values of E^*, ensuring that each model was recalibrated

based on a consistent metric. Fig. 8.3 presents the resulting curves for all configurations of one of the three specimen applied on the left femur (Black-and-White Left Femur), demonstrating the impact of recalibration on the mechanical response. This process was repeated for all configurations across all samples, effectively aligning the simulations with a comparable baseline and facilitating a more accurate analysis of mechanical behavior across different model configurations.
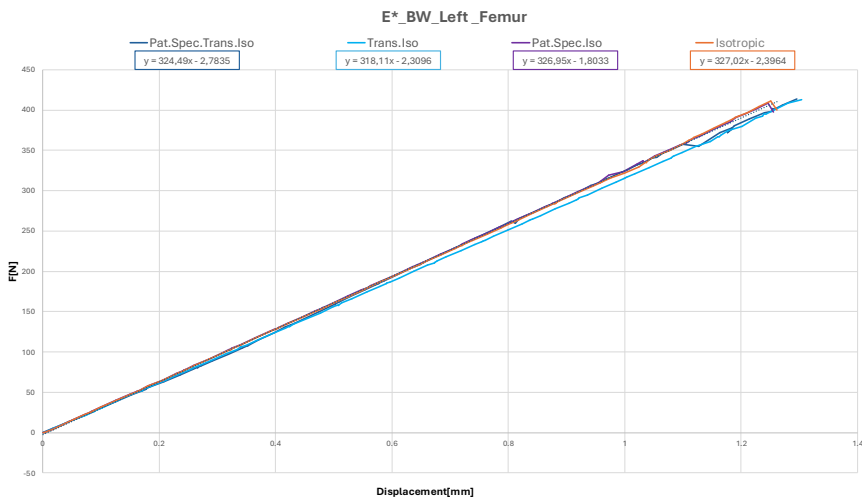

Figure 8.3: Linear interpolation for the four cases of the Black-and-White Left Femur recalibrated with E^*

8.3 The Importance of E^* in Model Comparison

The introduction of E^* served several critical purposes in this study:

- Standardization of models: by recalibrating each model with E^*, the variations between different configurations were normalized, allowing for a fair comparison. This process ensured that each model's mechanical response could be evaluated against a common reference, reducing the impact of initial variability in material properties.

- Enhanced accuracy: the use of E^* allowed the FEA simulations to better mirror the experimental data, as it incorporated both the calculated rigidity and the original elastic modulus. This led to a closer alignment between the simulated force-displacement curves and those observed experimentally, increasing the accuracy and reliability of the models.

- Linking mechanical and radiomic data: perhaps the most significant aspect of E^* is its role in bridging the gap between mechanical properties and radiomic features. As a recalibrated measure of elasticity that reflects the mechanical behavior of bone, E^* can be used to correlate physical properties with radiomic characteristics extracted from imaging data. This correlation provides deeper insights into how the microstructural features of bone, as captured through radiomics, translate into mechanical performance.

The derivation of E^* was pivotal in creating a robust framework for evaluating the various model configurations. Without such a parameter, direct comparisons between models would be hindered by discrepancies in their initial settings and inherent material variability. E^* provided a means of recalibrating these differences, effectively bringing all models into alignment with a shared point of reference. This approach is particularly valuable in the context of biological studies, where variability between specimens can obscure meaningful trends. By using E^* as a calibrated parameter, it was possible to reveal subtle differences in mechanical behavior across the models, offering a more nuanced understanding of the biomechanics of feline bones.

8.3.1   Presentation of the Obtained Force-Displacement Curves

After standardizing the models and deriving E*, the recalibrated force-displacement curves for each model were obtained. Figures8.4-8.13 depict these curves, highlighting the inter-model variations in rigidity and elastic modulus. These visualizations not only confirm the applicability of our calibration process but also serve as the foundational data for the subsequent comparative analysis across different model configurations. It is important to note that while these curves are critical for demonstrating the practical outcomes of our methodology, they are not without imperfections. The inherent variability in bone material properties and the challenges associated

with finite element modeling of biological tissues can introduce discrepancies. However, the primary value of these curves lies not in their perfection but in their capacity to facilitate a standardized approach to model comparison. This standardization is crucial for assessing the mechanical behavior of the samples under study consistently and meaningfully." Thus, despite the limitations, these curves are instrumental in advancing our understanding of the relationship between mechanical properties and radiomic features, offering new insights into bone behavior. This approach aligns with the overarching goal of our research-to develop a robust framework for predicting bone mechanical properties from radiomic data

8.4 Validation of Model Accuracy Using Dynamic Time Warping

After calculating and incorporating E^* into the finite element models, it was necessary to validate how well these models aligned with the experimental force-displacement curves. For this purpose, Dynamic Time Warping (DTW) was employed as the primary method for curve alignment and comparison. DTW is particularly well-suited for this task, as it allows for the non-linear alignment of datasets, accounting for shifts in the displacement axis that often arise due to experimental variability. To balance computational efficiency and accuracy, we utilized the FastDTW algorithm, an optimized approximation of traditional DTW. This method enabled the processing of large datasets while capturing detailed deviations between the model predictions and experimental results [127].

8.4.1 FastDTW for Curve Alignment

Each force-displacement curve derived from the finite element simulations was compared to its corresponding experimental curve using FastDTW. This algorithm computes the optimal warping path between curves, minimizing the cumulative distance between the datasets by allowing for non-linear realignments along the displacement axis. This approach was essential for addressing slight shifts in force application, often caused by experimental conditions like loading rate variations or machine compliance. By aligning key features-such as peaks in force and regions of plastic deformation-FastDTW provided a robust means of comparing the curves, ensuring that

minor temporal misalignment did not skew the analysis [127].

8.4.2   Assessing the Statistical Significance of DTW Distances

To evaluate the alignment between experimental and simulated force-displacement curves, FastDTW was employed. This algorithm allows for non-linear realignment, accommodating slight shifts in displacement that may arise due to experimental variability. Since force application, material properties, and boundary conditions can introduce inconsistencies between finite element model predictions and experimental data, DTW serves as an effective metric for curve comparison. To assess the statistical significance of the observed DTW distances, a randomization test was implemented. The process consisted of the following steps:

Generation of Random Series

- A total of 1,000 permutations were generated by either randomly shuffling the experimental data or creating entirely synthetic displacement curves.

- This step established a **baseline distribution** representing expected variability in non-correlated datasets.

Calculation of DTW for Randomized Curves

- FastDTW was applied to each randomized pair to construct a distribution of DTW distances under non-correlated conditions.

- This ensured a robust statistical framework for evaluating whether the observed DTW values were meaningful.

Establishment of the Statistical Threshold

- A 5th percentile threshold was determined from the randomized DTW distribution.

- This threshold was used as a reference for assessing whether the observed DTW distances were statistically significant.

Comparison of Observed DTW vs. Randomized Distribution

- The DTW values from finite element models (FEM) were compared against the threshold.

- If the observed DTW was below the threshold, the alignment between the experimental and simulated curve was considered statistically significant.

- A p-value was computed as the proportion of random DTW values smaller than the observed DTW:

$$p = \frac{\sum_{i=1}^{N} \mathbb{I}(DTW_i \leq DTW_{\text{obs}})}{N} \tag{8.1}$$

where $\mathbb{I}$ is an indicator function and $N = 1000$ represents the number of permutations.

Model Configurations and Specimen Variability

This analysis was repeated for different finite element model configurations, including:

- Isotropic

- Isotropic-PS

- Transversely Isotropic

- Transversely Isotropic-PS

- Bonemat

Additionally, DTW comparisons were performed across different specimens (humeri and femurs) to evaluate how bone type and structural complexity influenced alignment accuracy.

Data Aggregation for Comparative Analysis

To systematically compare the different model performances, DTW distances and p-values were summarized in three tables, each corresponding to different bone samples. These results provided insight into whether certain models consistently outperformed others.

8.5   Conclusion

In this chapter, we established a robust methodology for evaluating and refining finite element models of feline bones through the calculation of E^* and the application of Dynamic Time Warping (DTW). The derivation of E^* provided a recalibrated elastic modulus for each model, enabling consistent comparison across different configurations. This process ensured that the mechanical properties derived from the force-displacement curves were aligned with a common reference, allowing for a more accurate assessment of each model's behavior under load. Following this recalibration, the use of FastDTW allowed for a precise alignment of the force-displacement curves between the experimental data and the FEA simulations. The DTW analysis addressed temporal shifts and non-linear deviations that could arise from variations in testing conditions, offering a detailed comparison of the models' predictive accuracy. The subsequent randomization test added a statistical layer of validation, distinguishing meaningful alignments from those that could occur by chance. Together, the recalibration with E^* and the DTW-based evaluation formed a comprehensive approach for assessing the accuracy and reliability of the finite element models. This dual approach not only validated the FEA models against experimental data but also provided insights into the mechanical behavior of the bone that could be further explored through correlations with radiomic features. The chapter thus sets the foundation for a deeper understanding of how well the models replicate real-world behavior and their potential for predicting bone mechanics in future studies.
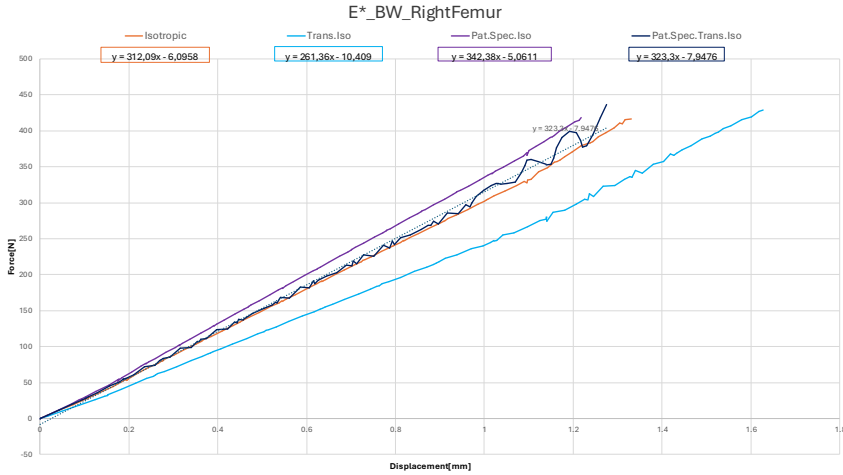
Figure 8.4: Linear interpolation for the four cases of the Black-and-White Right Femur recalibrated with E^*
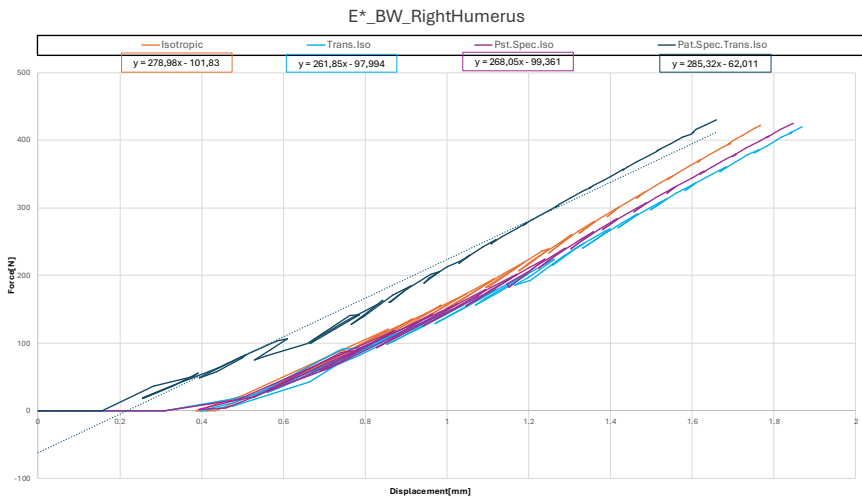

Figure 8.5: Linear interpolation for the four cases of the Black-and-White Right Humerus recalibrated with E^*

Figure 8.6: Linear interpolation for the four cases of the Black-and-White Left Humerus recalibrated with E^*

Figure 8.7: Linear interpolation for the four cases of the Gray Left Femur recalibrated with E^*

Figure 8.8: Linear interpolation for the four cases of the Gray Right Femur recalibrated with E^*

Figure 8.9: Linear interpolation for the four cases of the Gray Left Humerus recalibrated with E^*

Figure 8.10: Linear interpolation for the four cases of the Gray Left Humerus recalibrated with E^*

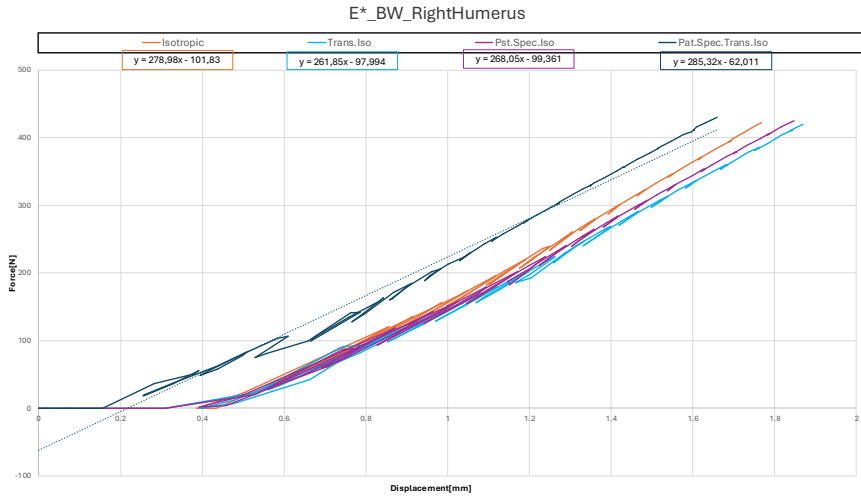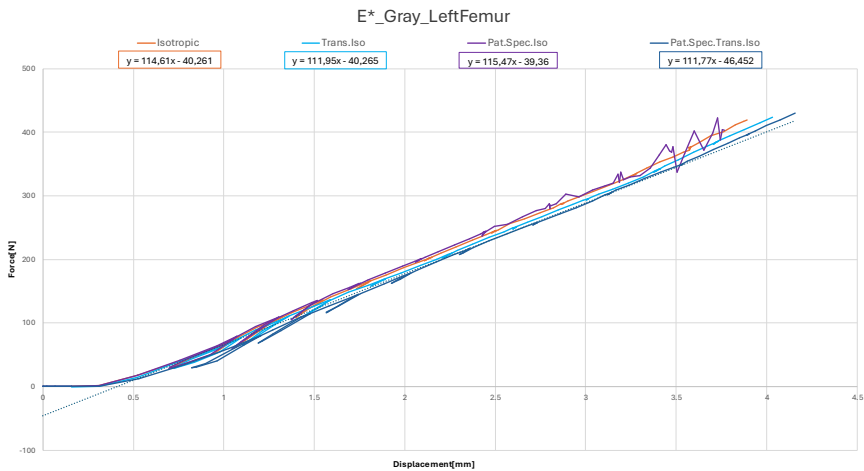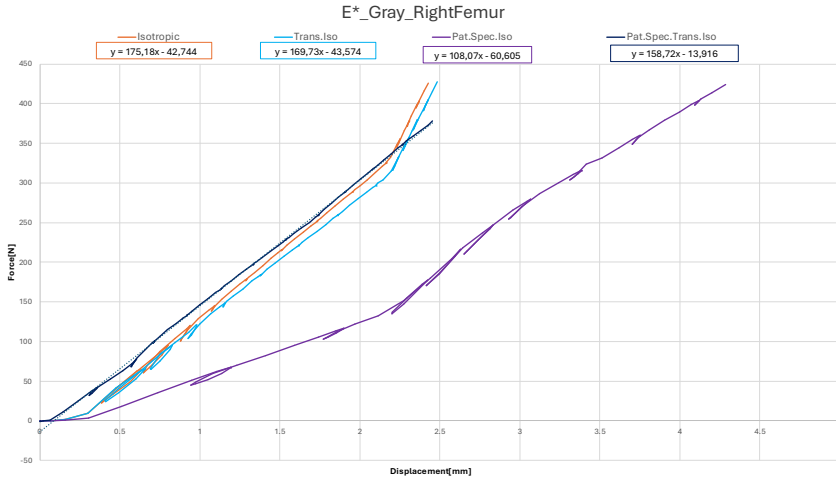Figure 8.11: Linear interpolation for the four cases of the Black Left Femur recalibrated with E^*
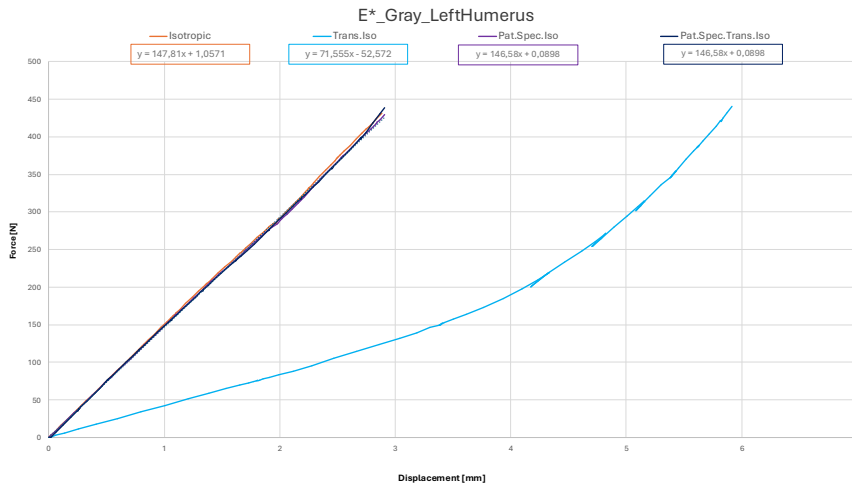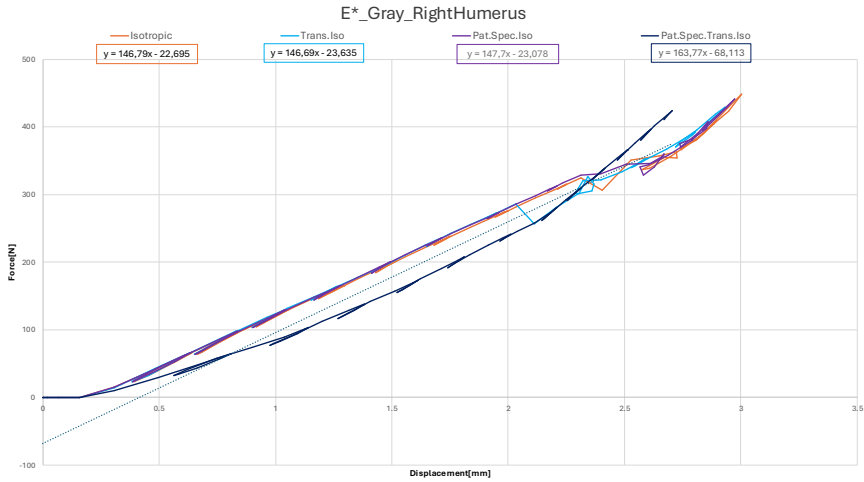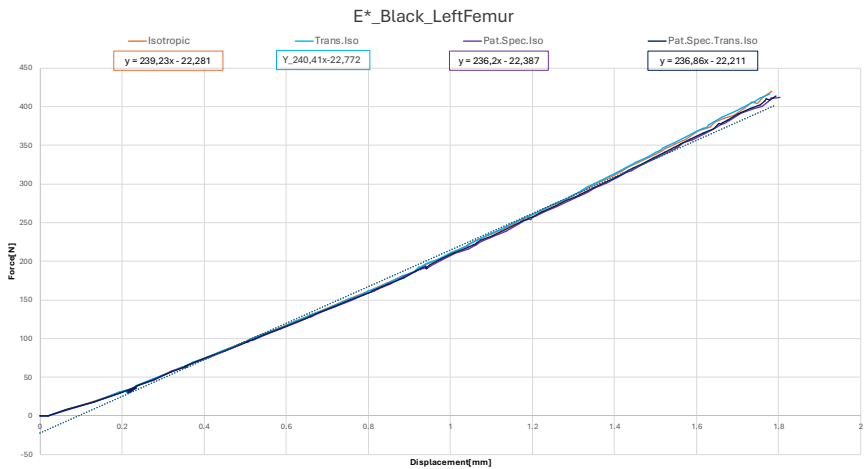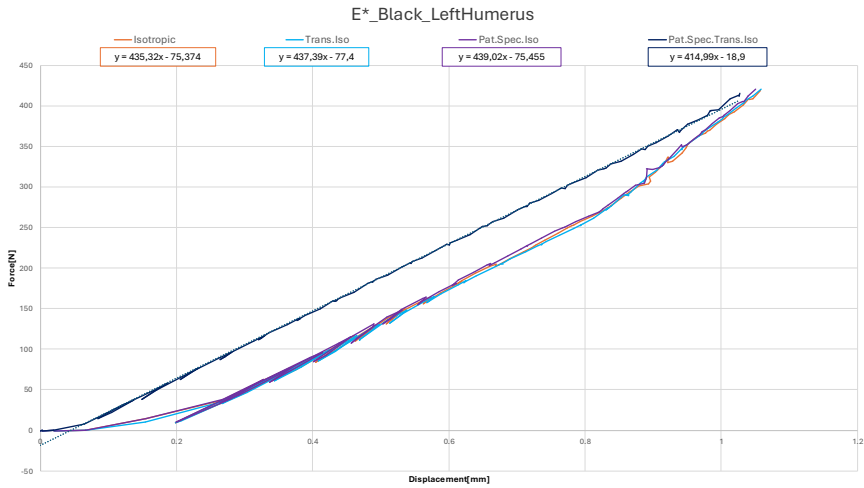
Figure 8.12: Linear interpolation for the four cases of the Black Left Humerus recalibrated with E^*
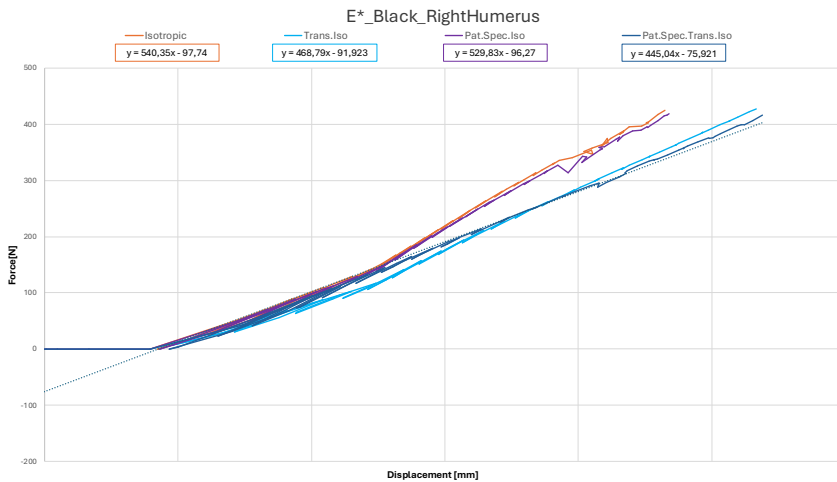
Figure 8.13: Linear interpolation for the four cases of the Black Right Humerus recalibrated with E^*

Chapter 9

Results Analysis

This chapter investigates the mechanical behavior of bone models by integrating radiomic features with finite element analysis. Principal Component Analysis (PCA) revealed a strong correlation between PC3 and the recalibrated elastic modulus, E^*, highlighting the influence of fine-scale structural variations. Additionally, an Interquartile Range (IQR) adjustment did not enhance correlations, suggesting that extreme values carry critical biomechanical information. To assess model accuracy, Dynamic Time Warping (DTW) and randomization tests were employed, confirming statistically significant yet acceptable deviations. These findings emphasize the trade-off between model precision and real-world variability in biomechanical simulations.

9.1 Linking Radiomic Features with Mechanical Properties

In this study, we aimed to establish a robust understanding of the mechanical properties encapsulated in E^*, derived from multiple finite element models. The analysis considered different biomechanical configurations: isotropic, isotropic patient-specific, transversely isotropic, transversely isotropic patient-specific, and Bonemat. A key methodological decision was the treatment of the Bonemat model, which assigns varying elastic moduli across elements rather than a single homogeneous value. One initial

consideration was to normalize E^* within Bonemat by computing a mean elastic modulus and correlating it with radiomic features. However, this approach was ultimately dismissed. The primary reason was that averaging the elastic modulus across all elements would obscure the intrinsic mechanical heterogeneity introduced by Bonemat, which is a fundamental aspect of its modeling approach. Instead, Bonemat was analyzed separately, focusing on its mechanical performance, while correlation analyses between radiomic features and E^* were conducted exclusively on the other models, where the elastic modulus was applied homogeneously across elements. To assess the reliability of these models in predicting mechanical behavior, we employed Principal Component Analysis (PCA)to reduce dimensionality and identify the most relevant radiomic features contributing to mechanical variability. Since radiomic datasets contain a high number of correlated features, PCA was crucial to extracting a subset of independent components that capture most of the variance. In particular, our analysis revealed that PC1 and PC2 captured broader structural variations, whereas PC3 was associated with finer microstructural details, which played a dominant role in mechanical correlations. Following this dimensionality reduction, a Pearson correlation analysis was performed to determine the strength of association between radiomic features and E^*. The analysis identified significant correlations primarily with PC3-derived features, emphasizing the importance of localized structural variations. Lastly, Dynamic Time Warping (DTW) with randomization tests was used to evaluate the ability of each finite element model to replicate experimental force-displacement behavior. This step ensured that observed deviations were statistically meaningful rather than artifacts of model assumptions. The following sections will detail the results of each of these analyses, highlighting the radiomic features most strongly linked to mechanical behavior and the modeling approaches that provided the most accurate predictions.

9.2 Principal Component Analysis (PCA) and Distribution of Variance

To gain a deeper understanding of the radiomic features extracted from bone images, we applied Principal Component Analysis (PCA). This dimensionality reduction technique enabled us to identify the most significant patterns within a high-dimensional dataset, simplifying the complexity without los-

ing critical information. Our analysis revealed that the first three principal components, PC1, PC2, and PC3, captured 91% of the total variance in the dataset. This high level of explained variance indicates that these three components encapsulate the majority of structural differences and variability present in the bone data. Specifically:

- PC1 is dominated by features related to gray-level non-uniformity and large-scale intensity distributions, including GrayLevelNonUniformityNormalized (GLRLM, GLSZM), Id, Idn, Kurtosis, LargeAreaHighGrayLevelEmphasis, LongRunEmphasis, and RunVariance.

- PC2 is primarily influenced by structural coherence measures, with Joint Energy as the most relevant feature.

- PC3 captures fine-scale textural variations and local intensity changes, and is strongly correlated with E^* in the isotropic and transversely isotropic models.

To ensure that these components could be meaningfully correlated with mechanical properties, we isolated the most significant features for each principal component. Since PCA assumes normally distributed data for optimal performance, we verified the distribution of selected features before proceeding with further statistical analysis. Given the prominence of PC3 in mechanical correlations, we then performed a Pearson correlation analysis to determine the strength of association between the recalibrated elastic modulus, E^*, and the extracted radiomic features. The following section presents these results in detail.

9.2.1 Correlation Analysis

The results of the Pearson correlation analysis highlighted a significant finding: the majority of features with strong correlations to E^* originated from PC3. This observation suggests that the fine-grained structural variations captured by PC3 play a crucial role in determining the mechanical properties of bones. Unlike PC1 and PC2, which capture more general structural attributes such as overall bone size or shape, PC3 delves into more detailed textural aspects and microstructural features. The strong correlations observed in PC3 reinforce the importance of localized variations in bone structure when evaluating mechanical behavior. These finer details include

localized regions of density, variations in gray-level intensity, and other subtle textural patterns that often have a direct influence on how bones behave under mechanical loads. For example, regions with higher local densities or specific textural emphases might contribute more significantly to the bone's overall stiffness or its ability to withstand stress. This makes PC3 particularly relevant when analyzing parameters like E^*, which is sensitive to variations in stiffness and load-bearing capacity. To further illustrate these relationships, we present scatter plots of selected features that exhibited strong correlations with E^*. In particular, Figure 9.1 shows the relationship between GrayLevelNonUniformityNormalized GLSZM and E^* in the Bonemat model, highlighting a strong positive correlation. Similarly, Figure 9.2 illustrates the correlation between Strength and E^* in the isotropic model, while Figure 9.3 presents the correlation of HighGrayLevelEmphasis with E^* in the transversely isotropic patient-specific model.
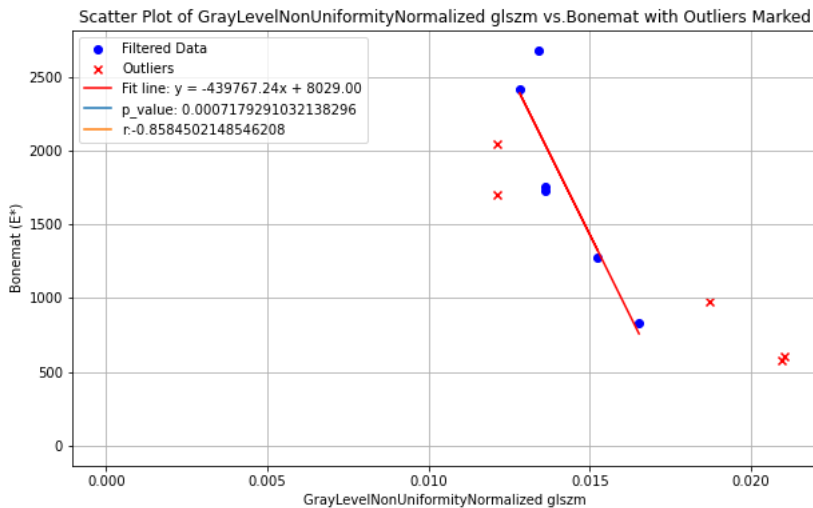
Figure 9.1: Scatter plot of GrayLevelNonUniformityNormalized GLSZM vs E^* in the Bonemat model.

The strong relationship between PC3 features and E^* underscores the importance of considering these localized variations when evaluating mechanical behavior. It suggests that the mechanical response of bone, partic-
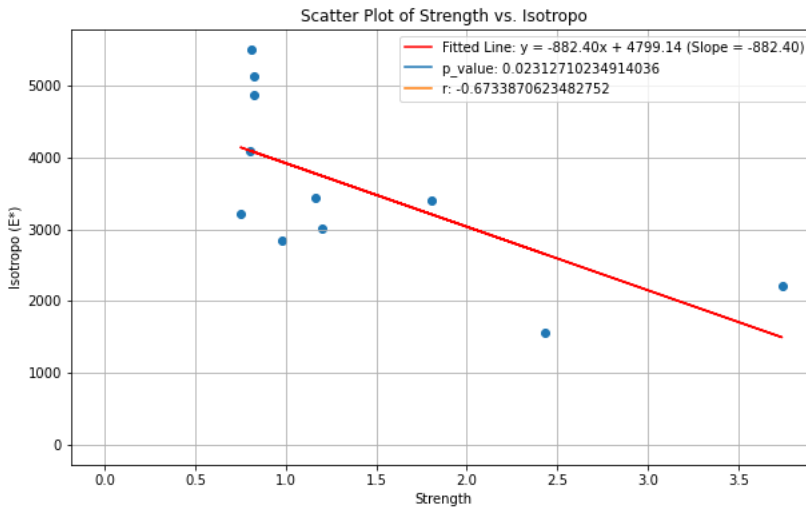
Figure 9.2: Scatter plot of Strength vs E^* in the isotropic model.

ularly in terms of stiffness and resilience, is not solely determined by general structural characteristics but is heavily influenced by the nuanced, fine-scale variations captured by PC3.

9.2.2   Analysis of PC Features: Femurs vs. Humeri

While PC3 features exhibited the strongest correlations with mechanical properties, we also examined the role of PC2 features, particularly in distinguishing different bone types such as the femur and the humerus. To assess whether PC2 features captured significant differences in mechanical behavior between these bones, we conducted a statistical significance test. The distribution of PC2 values across different specimens is shown in Fig. 9.4. The analysis yielded a p-value of 0.06, which is slightly above the conventional threshold for statistical significance ($p<0.05$). Although this does not meet the strict criterion for significance, the result suggests a potential trend indicating differences between the mechanical behavior of the femur and humerus. The near-significant result implies that subtle mechanical variations may exist between the two bone types, which could be more clearly
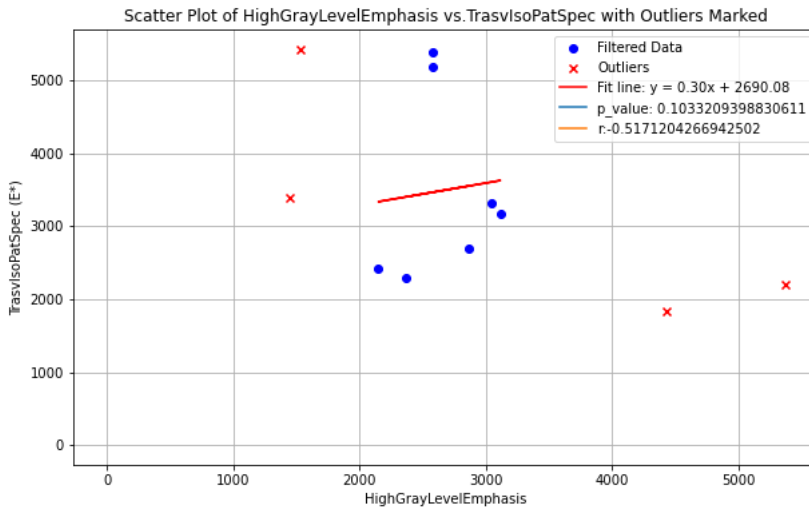
Figure 9.3: Scatter plot of HighGrayLevelEmphasis vs E^* in the transversely isotropic patient-specific model.

delineated with a larger sample size. This borderline significance may be attributed to the limited number of samples, which introduces variability and reduces statistical power, potentially masking true differences. Expanding the dataset in future studies could improve the reliability of this analysis, allowing for a more definitive distinction between the mechanical properties of different bone types when analyzed through PC2 features.

9.2.3   Interpretation of Results

The findings from this study provide valuable insights into the interplay between radiomic features and mechanical properties, particularly E^*. The strong correlations observed between PC3 features and E^* emphasize the importance of microstructural details in determining bone behavior. Radiomic features that capture localized variations, such as high gray-level zone emphasis and fine textural patterns, offer a more detailed understanding of how specific regions within the bone contribute to overall strength, stiffness, and resilience. These insights are crucial for improving biomechanical models
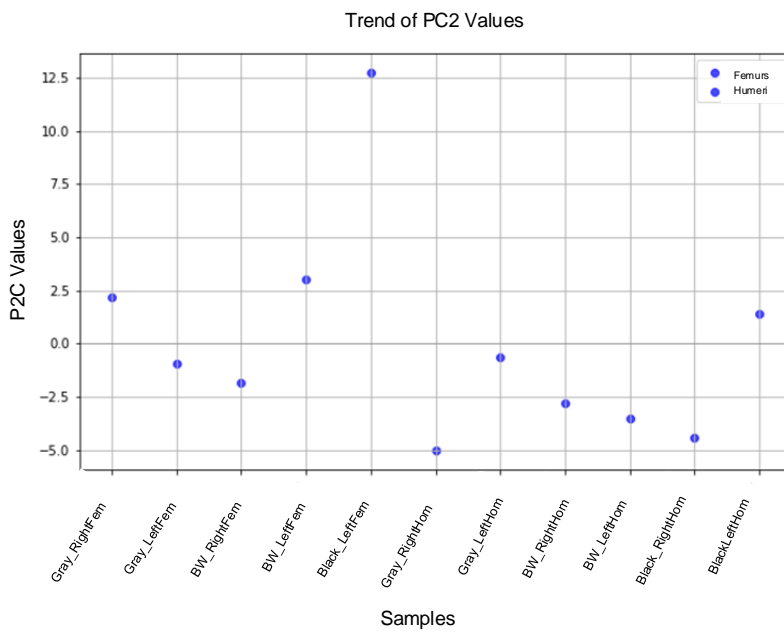
Figure 9.4: Trend of PC2 Values in Femurs and Humeri. The plot illustrates the distribution of PC2 values across different specimens, highlighting potential structural variations between bone types.

and enhancing the predictive power of radiomics in assessing bone health. Conversely, the near-significant findings related to PC2 features suggest that further investigation is required to differentiate the mechanical behavior of distinct bone types, such as the femur and humerus. Given that the p-value was slightly above the conventional significance threshold, future studies should focus on increasing the sample size to enhance statistical power. This would help validate whether PC2 truly captures structural differences that influence mechanical responses across bone types. Expanding the dataset would also allow for more sophisticated analyses, such as stratified testing or the implementation of non-parametric methods, to better characterize variability between different bone regions. This could provide further insights into how broader structural trends (captured by PC2) interact with localized microstructural variations (captured by PC3) to influence mechanical behavior.

9.3   IQR

To refine the correlation analysis between radiomic features and E^*, the parameter encapsulating mechanical behavior, we applied an Interquartile Range (IQR) adjustment. This step aimed to mitigate the influence of outliers by focusing on the middle 50% of the data, thereby providing a clearer understanding of the relationship between features and E^*. However, after applying the IQR adjustment, the correlation strength between radiomic features and E^* did not show any significant improvement [150]. This outcome can be explained by considering how the IQR adjustment affects the dataset and what the outliers may represent.

- **IQR Removes Variability Critical for Mechanical Properties:** Mechanical properties, such as E^*, often rely on extreme values or localized structural variations within the bone. These extreme values may correspond to high-density regions or areas of concentrated stress, which are crucial for describing mechanical behavior. By applying IQR, data points beyond a certain threshold (typically outside 1.5 times the IQR) are removed. If these outliers capture significant mechanical characteristics that contribute to E^*, their removal could diminish the correlation strength, as critical information is lost in the process.

- **IQR Focuses on Central Tendencies:** The IQR adjustment em-

phasizes the central range of the data, thereby removing extreme values
that might hold key insights into bone mechanics. E^* could be par-
ticularly influenced by variations at the extremities of the data, such
as regions of unusually high or low bone density, which are important
for understanding stiffness or load-bearing capacity. By focusing solely
on the central data range, IQR may exclude these relevant variations,
thus weakening the correlation between radiomic features and E^*.

- **Outliers as Informative Data:** In biomechanical studies, outliers
  do not always represent noise; they can indicate meaningful differences
  in mechanical properties. Some bones may be significantly stronger
  or weaker than average, reflecting unique structural features that are
  essential for understanding E^*. Removing these outliers through IQR
  could lead to a weaker overall correlation because the features that
  drive the relationship with mechanical properties are excluded.

- **Nonlinear Relationships:** The relationship between E^* and ra-
  diomic features may be nonlinear, with extreme values (outliers) play-
  ing a crucial role in capturing the complexity of this relationship. By
  applying IQR, these data points are removed, leaving only the more
  linear trends within the middle range of the data. As a result, the re-
  maining data might be less predictive of mechanical behavior, reducing
  the strength of the correlation.

- **Reduction in Data Variability:** The IQR adjustment reduces the
  spread of the dataset, which may inadvertently diminish the variability
  necessary to express meaningful correlations. For mechanical proper-
  ties like E^*, specific extremes or regions of high stress might drive the
  correlation. By narrowing the dataset to a smaller range, the overall
  correlation is weakened because the variation that contributes to the
  mechanical characterization is removed [172].

9.4 Significance of DTW Distance: Interpreting Acceptable Deviations from Experimental Curves

The use of Dynamic Time Warping (DTW) in analyzing force-displacement
curves enabled the identification of statistically significant DTW distances

between model predictions and experimental data [9]. Finite element models aim to closely replicate experimental behaviors; however, deviations are expected due to inherent variability in experimental conditions and modeling assumptions. The critical question is whether these deviations are meaningful or within an acceptable error range. To address this, we established a threshold DTW distance using a randomization test based on the distribution of 1000 random or permuted time series [51]. This statistical threshold allowed us to evaluate whether observed DTW distances were significant. A full DTW analysis was conducted for all specimens across different modeling configurations. Here, we report some example to illustrate the approach we used. These figures do not represent overall results but serve to highlight thre process we implemented. The complete results are systematically summarized in the tables presented in the next sections. Fig. 9.5 shows an example of a direct comparison between the experimental force-displacement curve and the simulated isotropic model for the Black-and-White Right Femur bone sample. While the simulated model follows the general trend of the experimental curve, discrepancies appear at higher displacement values.
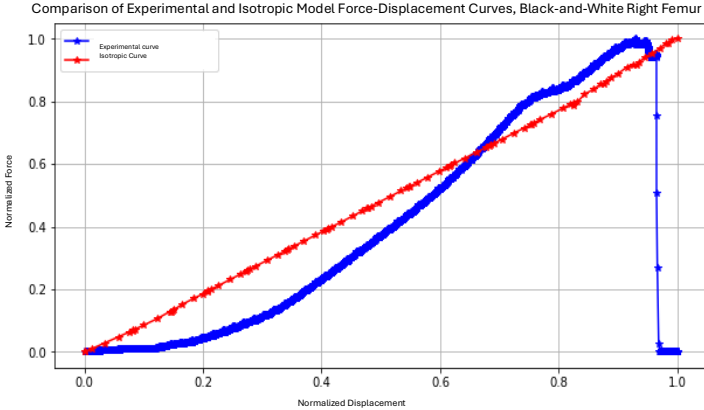
Figure 9.5: Example of comparison between experimental and simulated force-displacement curves for the isotropic model (Black-and-White Right Femur).

To further evaluate alignment accuracy we evaluated the DTW path for aligning the experimental and model curves. Fig. 9.6 presents an example of the DTW path for aligning the experimental and isotropic model curves.

The relatively smooth alignment suggests that the isotropic model captures
the experimental trend well, with minimal shifts required for alignment.
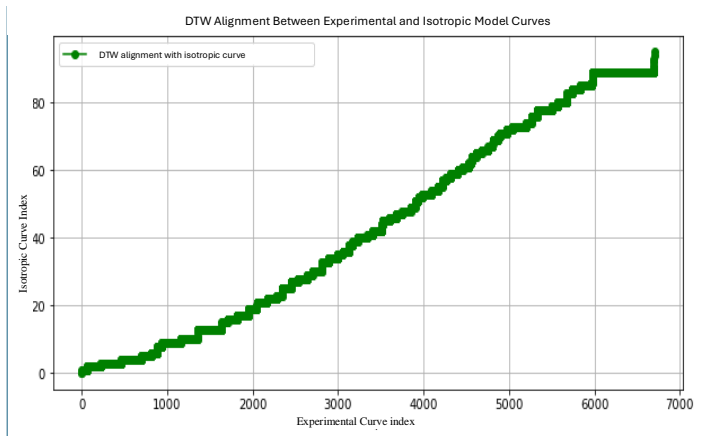
Figure 9.6: Example of DTW alignment between the experimental and
isotropic model curves (Black-and-White Right Femur).

For a statistical assessment of DTW distance significance, we generated
a bootstrap distribution of DTW distances. An example of distribution of
DTW values under random conditions is shown in Fig. 9.7, with the observed
DTW value (648.60) marked in red. The observed DTW falls within the
lower range of the bootstrap distribution, indicating that the isotropic model
aligns significantly with experimental data.

These figures serve only as illustrative examples of the observed behav-
ior in different cases. The full dataset of DTW distances for all specimens
is presented Tables 9.8, 9.9, and 9.10, where a systematic comparison of
all configurations is reported. The results indicate a fair alignment between
model predictions and experimental data, with discrepancies remaining small
enough not to compromise the model's validity. Variation in DTW distances
across different bone specimens highlighted how specimen type and struc-
tural complexity impact model accuracy [112].

9.4.1   Summary of DTW Results Across Specimens

To provide a more comprehensive overview, Tables 9.8, 9.9, and 9.10 sum-
marize the DTW distances for different specimens.
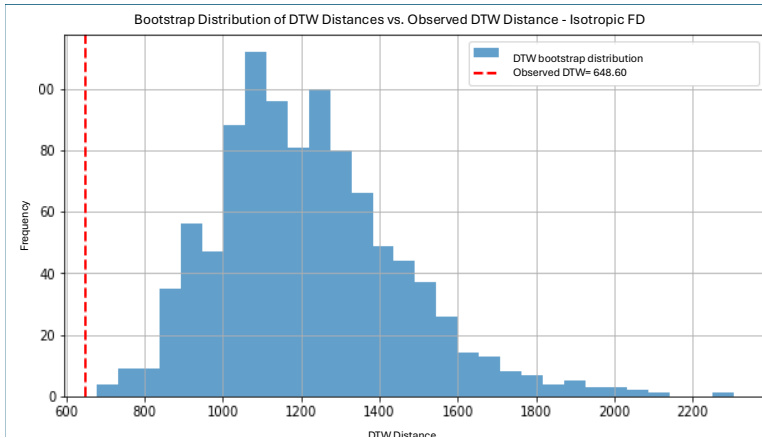
Figure 9.7: Example of bootstrap distribution of DTW distances vs. observed DTW value (648.60) for the isotropic model (Black-and-White Right Femur).

For the right humerus of the Black-and-White specimen, DTW distances achieved statistical significance, with the following p-values across configurations: isotropic (p=0.005), isotropic tailored (p=0.005), transversely isotropic (p=0.013), transversely isotropic tailored (p=0.007), and Bonemat (p=0.004). These values suggest satisfactory alignment between the model predictions and experimental data for this specimen. Conversely, for a smaller specimen (specimen 3), none of the models yielded statistically significant DTW distances, indicating limitations in replicating the experimental force-displacement behavior for this case.

9.4.2   Implications for Model Performance

These findings suggest that the structural characteristics and scale of bone specimens are key to the model's capacity to replicate experimental behavior accurately. Larger or structurally complex specimens may exhibit more distinct force-displacement patterns that the model captures more reliably, whereas simpler or smaller specimens might lack the structural variability needed for statistically significant DTW distances. The observed variability across specimens could also stem from the limited number of models analyzed and the effect of user-dependent variables in the modeling pro-

cess. Factors such as boundary conditions, material properties, and mesh configurations rely on user interpretation, introducing variability that can affect model outcomes. Additionally, the relatively small sample size may contribute to inconsistencies in DTW significance across specimens.

9.5 Conclusion

This study demonstrates the potential of radiomic features in predicting mechanical properties such as E^*, offering new insights into bone biomechanics. The strong correlations identified, particularly within PC3, emphasize the relevance of fine-scale structural variations in determining mechanical behavior. Additionally, the use of Dynamic Time Warping (DTW) for validating finite element model predictions provided a robust framework for assessing model reliability. However, to enhance the clinical applicability of these findings, further validation is required through expanded studies incorporating human samples. This step is crucial to ensure that the relationships observed in feline bones translate effectively into human bone biomechanics. Future research should also focus on increasing the dataset size and incorporating different imaging modalities to improve result reproducibility. Additionally, exploring advanced statistical techniques and machine learning approaches may further refine the predictive accuracy of radiomic-based biomechanical models. By integrating radiomics with finite element modeling, this study lays the foundation for a more comprehensive understanding of bone mechanics. The insights gained here could contribute to improved diagnostics and patient-specific treatments in orthopedic and musculoskeletal research.

SAMPLE	MODEL CONFIGURATION	DTW DISTANCE
GRAY RIGHT FEMUR	Experimental-Isotropic	1764.89
	Experimental-Patient Specific Isotropic	1776.06
	Experimental-Transversely Isotropic	1778.37
	Experimental-Patient Specific Transversely Isotropic	1654.5
	Experimental-Bonemat	1866.25
GRAY LEFT FEMUR	Experimental-Isotropic	1714.18
	Experimental-Patient Specific Isotropic	1730.74
	Experimental-Transversely Isotropic	1721.31
	Experimental-Patient Specific Transversely Isotropic	1732.1
	Experimental-Bonemat	1968.9
GRAY RIGHT HUMERUS	Experimental-Isotropic	1377.35
	Experimental-Patient Specific Isotropic	1376.95
	Experimental-Transversely Isotropic	1332.75
	Experimental-Patient Specific Transversely Isotropic	1584.47
	Experimental-Bonemat	1544.95
GRAY LEFT HUMERUS	Experimental-Isotropic	1046.99
	Experimental-Patient Specific Isotropic	1048.16
	Experimental-Transversely Isotropic	1268.3
	Experimental-Patient Specific Transversely Isotropic	1058.47
	Experimental-Bonemat	1203.59

Figure 9.8: Summary of DTW distances for gray cat specimens across different models.

SAMPLE	MODEL CONFIGURATION	DTW DISTANCE
BLACK AND WHITE RIGHT FEMUR	Experimental-Isotropic	649
	Experimental-Patient Specific Isotropic	652
	Experimental-Transversely Isotropic	622.87
	Experimental-Patient Specific Transversely Isotropic	615.66
	Experimental-Bonemat	277.14
BLACK AND WHITE LEFT FEMUR	Experimental-Isotropic	10.3
	Experimental-Patient Specific Isotropic	10.4
	Experimental-Transversely Isotropic	10.3
	Experimental-Patient Specific Transversely Isotropic	563.47
	Experimental-Bonemat	9.34
BLACK AND WHITE RIGHT HUMERUS	Experimental-Isotropic	17.94
	Experimental-Patient Specific Isotropic	18.03
	Experimental-Transversely Isotropic	852.38
	Experimental-Patient Specific Transversely Isotropic	18.81
	Experimental-Bonemat	19.38
BLACK AND WHITE LEFT HUMERUS	Experimental-Isotropic	48.52
	Experimental-Patient Specific Isotropic	48.53
	Experimental-Transversely Isotropic	48.45
	Experimental-Patient Specific Transversely Isotropic	48.57
	Experimental-Bonemat	41.94

Figure 9.9: Summary of DTW distances for black-and-white cat specimens across different models.

SAMPLE	MODEL CONFIGURATION	DTW DISTANCE
BLACK CAT LEFT FEMUR	Experimental-Isotropic	1214.21
	Experimental-Patient Specific Isotropic	1185.11
	Experimental-Transversely Isotropic	1202.036
	Experimental-Patient Specific Transversely Isotropic	1195.36
	Experimental-Bonemat	1317.14
BLACK CAT RIGHT HUMERUS	Experimental-Isotropic	700.93
	Experimental-Patient Specific Isotropic	705.65
	Experimental-Transversely Isotropic	709.75
	Experimental-Patient Specific Transversely Isotropic	642.45
	Experimental-Bonemat	641.3
BLACK CAT LEFT HUMERUS	Experimental-Isotropic	951.98
	Experimental-Patient Specific Isotropic	964.03
	Experimental-Transversely Isotropic	965.025
	Experimental-Patient Specific Transversely Isotropic	929.96
	Experimental-Bonemat	1156.5

Figure 9.10: Summary of DTW distances a for black specimens (3) across different models.

Chapter 10

Conclusion

This chapter summarizes the contribution of the thesis and discusses avenues for future research.

10.1 Summary of contribution

This thesis makes significant strides in integrating radiomic analysis, finite element analysis (FEA), and experimental validation to deepen our understanding of bone quality and its mechanical properties. The key contributions of this work are as follows:

- Development of a Radiomic Feature Extraction Pipeline: A detailed new workflow was designed to extract 107 radiomic features from CT images of bone structures, allowing for a comprehensive quantification of bone microarchitecture. This pipeline replicates the results achieved by 3D Slicer, considered the gold standard in the field, while offering greater flexibility. By enabling us to move beyond the limitations of existing software, this system allows for tailored adaptations that enhance our ability to capture relevant features, such as texture patterns, density variations, and structural heterogeneity, essential for in-depth characterization of bone quality.

- Integration of FEA with Radiomic Data to Derive E*: A novel aspect of this research was the derivation of an effective modulus (E^*), a parameter that represents the overall stiffness of bone models. This

was achieved by aligning FEA predictions with experimental force-displacement data through a recalibration process. (E^*) served as a standardized parameter, allowing for more consistent comparisons across different models and specimens. This approach addressed the challenge of variability in elastic modulus values within FEA simulations, particularly when dealing with models that vary in complexity, such as those using tailored elastic moduli for each element versus more uniform configurations. The use of (E^*) provided a more coherent basis for correlating mechanical properties with radiomic features, contributing to a deeper understanding of the structural underpinnings of bone behavior.

- Application of Principal Component Analysis (PCA) for Feature Reduction: To manage the high dimensionality of the radiomic data, PCA was applied, revealing that the first three principal components (PC1, PC2, and PC3) accounted for 91% of the total variance. This high percentage indicates that these components encapsulate the majority of structural variations present in the bone data. A key finding was that PC3, which captures finer, localized textural variations, showed the strongest correlation with mechanical properties such as the effective modulus (E^*). This suggests that microstructural details, like variations in gray-level intensity and localized density, play a crucial role in determining how bones respond to mechanical loads, beyond what can be inferred from broader structural characteristics.

- Validation of Model Accuracy Using Dynamic Time Warping (DTW) and Statistical Analysis: To assess the accuracy of FEA predictions, Dynamic Time Warping (DTW) was employed to compare model-predicted force-displacement curves with experimental data. The application of DTW allowed for the non-linear alignment of these curves, accounting for shifts in the displacement axis due to experimental variability. Additionally, a randomization test was performed, generating a distribution of DTW distances from randomly permuted time series to establish a threshold for statistical significance. This dual approach enabled the identification of deviations that, while present, were considered acceptable and statistically significant. By doing so, the study provided a rigorous framework for evaluating the predictive accuracy of FEA models and ensuring that the deviations from experimental results were within a justifiable range.

- Isolation and Analysis of Mechanical Variability Using a Bonemat Model: In addition to the primary FEA models, a Bonemat-based model was analyzed to isolate purely mechanical performance without the confounding effects of radiomic variability. This approach allowed for a detailed assessment of how mechanical properties change when individual elastic moduli are assigned to each mesh element. The analysis of the Bonemat model highlighted the complexity of bone's mechanical response and offered insights into the limitations and potential of using tailored mechanical parameters in predictive modeling.

These contributions collectively offer a new framework for studying bone quality through the lens of advanced radiomic analysis and mechanical modeling. The methodologies developed in this thesis not only advance the field of radiomics but also provide a foundation for future studies aimed at improving diagnostic accuracy in orthopedics.

10.1.1 Validation and Reproducibility

The robustness and clinical relevance of the radiomic models and mechanical analyses developed in this study require further validation through expanded studies. While this research focused on a preclinical model using feline bones, the application of these models to human samples is crucial for translating the findings into clinical practice. Expanding the sample size and including a diverse range of imaging modalities would enhance the reproducibility of the results, reducing the risk of bias and improving the generalization of the models. Additionally, replicating the analysis with different software platforms could ensure the consistency and robustness of the radiomic feature extraction and its correlation with biomechanical properties. Such steps are vital for establishing a reliable framework for clinical applications in assessing bone health and fracture risk.

10.2 Directions for Future Work

While this study has offered valuable insights into the relationship between radiomic features and bone mechanics, establishing a foundation for a novel investigative approach, several limitations and opportunities for future research have emerged. Addressing these areas can strengthen the robustness and broaden the applicability of our findings:

- Increase in Sample Size: One of the primary limitations of this study is the relatively small sample size, which may have influenced the variability observed in correlation results and DTW significance. A limited number of bone specimens can introduce statistical noise, reducing the ability to detect subtle yet important relationships between radiomic features and mechanical properties. Future studies should aim to expand the sample size, including a broader range of bone types and conditions. This would increase statistical power, improve the generalization of findings, and enable more robust comparisons between different bone regions, such as the femur and humerus.

- Refinement of Radiomic Models for Clinical Relevance: While this research has shown that radiomic features are promising predictors of mechanical properties, there is a need for further refinement to ensure their consistency across different imaging modalities and patient populations. Future work should focus on standardizing imaging protocols, feature extraction methods, and image preprocessing steps. This will help reduce variability and ensure that the radiomic models can be applied reliably in diverse clinical settings. Additionally, further validation against large clinical datasets will be essential to translate the radiomic findings into practical diagnostic tools for assessing bone health and fracture risk.

- Exploration of Nonlinear Models and Machine Learning Techniques: The correlation analysis in this study primarily relied on linear methods, such as Spearman correlation. However, the relationship between radiomic features and mechanical properties may be more complex than a linear model can capture. Future research could benefit from the application of nonlinear modeling approaches, including machine learning algorithms like neural networks or random forests, to better capture these complex relationships. These methods could enhance the predictive power of radiomic analysis by identifying patterns that are not evident through traditional statistical approaches, potentially improving the accuracy of predictions related to bone strength and behavior.

- Clinical Translation and Development of Decision Support Tools: Building on the promising results of this study, future work should focus on translating these findings into clinical practice. Developing software

tools that integrate radiomic analysis and FEA results could provide clinicians with a more comprehensive understanding of patient-specific bone health. These tools could be used for personalized risk assessment of fractures, planning orthopedic surgeries, and evaluating the effectiveness of treatments such as bone-strengthening therapies. User-friendly interfaces and automated data processing pipelines would facilitate the use of these tools in clinical settings, bridging the gap between advanced research techniques and everyday clinical decision-making.

- Addressing Variability from User-Dependent Inputs: A notable challenge in this study was the variability introduced by user-defined parameters, such as boundary conditions, material properties, and mesh resolution in FEA models. This user dependency can affect the consistency of results across different studies or users. Future research could focus on developing standardized guidelines or automated methods for setting these parameters, reducing user-related variability. For example, machine learning-based optimization could be employed to automatically adjust model parameters based on input data, ensuring a more standardized approach to FEA simulations.

Looking forward, the integration of artificial intelligence (AI) techniques, such as machine learning, presents a promising avenue for enhancing the predictive capabilities of radiomic models. By applying AI-driven methods to the radiomic features extracted from CT and CBCT images, it may be possible to develop more accurate models for predicting mechanical properties and fracture risk. These models could identify complex patterns in the data that traditional statistical methods might overlook, leading to a more personalized approach to bone health management. Furthermore, expanding this research to include other species and types of bones, such as human vertebrae or smaller mammalian bones, could broaden the applicability of the findings. Such studies would provide insights into the structural and mechanical properties of different bone types and help validate the models across various biological contexts. By leveraging these future research directions, the methodology developed in this study could be further refined, ultimately improving its utility in both preclinical research and clinical practice. By addressing these directions, future research can build upon the groundwork laid by this thesis, further advancing the integration of radiomics and biomechanics. This could ultimately lead to more accurate and personalized approaches for diagnosing and treating bone-related conditions, improving

patient outcomes in orthopedic care.

Appendix A

Publications

This research activity has led to several publications in international journals and conferences. These are summarized below.[1]

International Journals

1. **E. Barcali**, E. Iadanza, L. Manetti et al. "Augmented Reality in Surgery: A Scoping Review", *Applied Sciences*, 12(14):6890, 2022.

2. L. Calamandrei, L. Mariotti, E. Bicci, L. Calistri, **E, Barcali**; et al. "Morphological, Functional and Texture Analysis Magnetic Resonance Imaging Features in the Assessment of Radiotherapy-Induced Xerostomia in Oropharyngeal Cancer", *Applied sciences*, 15, 2023,008ef174-dbe3-4047-af04-1279e1b47ee5

3. A. Simoni and **E. Barcali**, C. Lorenzetto, E. Tiribilli et al. "Innovative Tool for Automatic Detection of Arterial Stenosis on Cone Beam Computed Tomography", *Applied Sciences*, 13, 2023, hdl: 2158/1319531

4. E. Bicci, C. Nardi, L. Calamandrei, **E. Barcali** et al., "Magnetic resonance imaging in naso-oropharyngeal carcinoma: role of texture analysis in the assessment of response to radiochemotherapy, a preliminary study", *Applied Sciences*, 14, 2023 hdl: 2158/1323632

5. S. Abudalfa, S.Lombardi, **E. Barcali**; et al. "Dual pipeline technique for detecting sepsis from photoplethysmography", *International Journal of Data mining and Bioinformatics*, 2024

---

[1]The author's bibliometric indices are the following: H-index = X, total number of citations = XX (source: Google Scholar on Month XX, 201x).

6. F. Giardini, **E. Barcali**, M. De Santis et al. "Optimization of a cardiac tissue segmentation pipeline in murine whole-heart reconstructions", *8th National Congress of Bioengineering, GNB*, 2023.

7. **E. Barcali**, L. Maggi, R. Panconesi et al. "Experimental Evaluation of a New Perfusion Machine using Normothermic Cycles on Explanted Livers", *IEEE Open Journal of Engineering in Medicine and Biology*, 2024

Submitted

1. **E.Barcali.**, L. Maggi, M. Falorni et al. "Monitoring and control system for a normothermic perfusion device", *Springer Nature*, Under press.

International Conferences and Workshops

1. **E. Barcali**, L. Maggi, M. Falorni et. al "The monitoring and control system for a normothermic perfusion device", in *Iupesm World Congress on Medical Physics and Biomedical Engineering (IUPESM WC2022*, Online, June 12th-17 2022.

2. **E. Barcali** "Exploring Patient-Specific Finite Element Analysis for Feline Femoral Biomechanics" in *XXIII ICMMB* , Bruxelles (Belgium), 2024. **Selected for submission as a full article to the special issue of the Journal of Mechanics in Medicine and Biology (JMMB)**

3. Joint EurAI Advanced Course on AI, TAILOR Summer School 2022; Universitat Politecnica de Catalunya (IDEAI-UPC), Barcelona (Spain), June 13th-17th 2022 **Best first year doctoral project**.

National Conferences

1. F. Giardini, **E. Barcali** , M. De Santis et al. "Optimization of a cardiac tissue segmentation pipeline in murine whole-heart reconstruction", in *GNB2023*, Padue (Padova) (Italy), 2023.

2. **E. Barcali** et al. "Preclinical study for bone characterization in humans with osteoporosis", in *21st National Day of Biomedical Engineering 2023 Annual Meeting of the IEEE-EMBS Benelux Chapter*, Bruxelles (Belgium), 2023.

3. Scuola di Biofotonica e Intelligenza Artificiale; Florence (Italy), September 5th-9th 2022, Florence

Technical Reports

1. **E. Barcali**, M. Orlandi, L. Calistri et al. "Artificial Intelligence and Radiomics at the University of Florence", *health managment.org*, 135–137, 2022, .

Appendix B

Special Acknowledgments

E ora i ringraziamenti piú preziosi, dedicati a chi mi ha sostenuta dall'esterno dell'ambiente accademico, a chi, pur non vedendomi all'opera in ambito lavorativo, ha sempre creduto nelle mie capacitá e nella mia voglia di fare. Mi sembrano passate milioni di vite da quel "ma sí proviamoci". Se mi guardo indietro, penso a quanta strada ho, anzi abbiamo fatto per arrivare a questa casetta in Belgio, a quante ne abbiamo passate, nel bene nel male, cercando di perseverare perché, alla fine, il traguardo non era poi cosí lontano. E ora ci siamo... finalmente. Ovviamente i primi a cui rivolgo il mio grazie sono miei genitori. Il mio meraviglioso punto di riferimento. Un dolce grazie per avermi sopportata durante tutti i miei sfoghi (e per avermi aiutata nei momenti di magra), sapevate che in un modo o nell'altro sarei arrivata in fondo. Non é stato facile, ma possiamo dire che mi ha portata ad essere dove sono oggi, e oggi sono felice. Molto del merito é anche vostro. Grazie Mamma. Grazie Papá. A mia sorella Beatrice, per essere stata una roccia quando ne avevo bisogno, per esserci sempre stata, per esserci sempre e per sempre, ma soprattutto per avermi insegnato, o meglio, dimostrato, che nulla é impossibile. E poi se non ha mollato lei, non potevo mollare io. Ai miei nonni e a mia zia, sempre al mio fianco, sempre fieri di me, pronti a darmi una parola di conforto e a tirarmi su quando sento che la sopraffazione mi tira giú. A Golia, sempre qui. Alle mie amiche, Totta, Ginni, Giulina, Livia e Madda per esserci nel mio quotidiano e per condividere gioie e dolori misti a prosecco e risate. Ai miei amici Bongins (come farei senza la tua saggezza?), Baccis, Matte e Tommi per strapparmi sempre quel sorriso in piú. Al tennis Carraia. Alle mie amiche del mare, alle mie amiche di sempre e alla mia

amica Meg che é entrata da poco nella mia vita, ma che, con il suo animo luminoso, riesce sempre a farmi sentire a casa. A Benni e a tutti gli amici di Bruxelles, italiani e non, senza i quali non sarei alla stessa. A tutti i miei amici, vecchi e nuovi, che negli anni mi hanno sostenuta che non nomino perché per fortuna siete tanti, grazie. Infine, al mio fidanzato Marco, che con le sue fossette e il suo sguardo dolce, la sua ambizione e il suo carattere determinato mi sprona a fare di piú e a non arrendermi mai ricordandomi che c'é sempre spazio per condividere le cose belle, e quelle meno, nel cuore di chi ti ama. Tu sei il mio posto al sole.

L'ultimo grazio va a me stessa. A me, perché non ho mollato. A me, perché ho mantenuto l'entusiasmo. A me, perché da oggi chiamatemi:

Ingegnere Eleonora Barcali, PhD.

Bibliography

[1] J. E. Adams, "Advances in bone imaging for osteoporosis," *Nature Reviews Endocrinology*, vol. 9, no. 1, pp. 28–42, 2013.

[2] R. Adams and L. Bischof, "Seeded region growing," *IEEE Transactions on Pattern Analysis and Machine Intelligence*, vol. 16, no. 6, pp. 641–647, 1994.

[3] H. J. W. L. Aerts, E. R. Velazquez, R. T. H. Leijenaar, C. Parmar, P. Grossmann, S. Carvalho, J. Bussink, R. Monshouwer, B. Haibe-Kains, D. Rietveld, F. J. P. Hoebers, M. M. Rietbergen, C. R. Leemans, A. Dekker, J. Quackenbush, R. J. Gillies, and P. Lambin, "Decoding tumour phenotype by noninvasive imaging using a quantitative radiomics approach," *Nature Communications*, vol. 5, p. 4006, 2014.

[4] M. A. Alzubaidi and M. Otoom, "A comprehensive study on feature types for osteoporosis classification in dental panoramic radiographs," *Computer Methods and Programs in Biomedicine*, vol. 188, p. 105301, May 2020, epub 2019 Dec 25. [Online]. Available: https://doi.org/10.1016/j.cmpb.2019.105301

[5] A. Anderson, B. Ellis, and J. Weiss, "Verification, validation and sensitivity studies in computational biomechanics," *Computer Methods in Biomechanics and Biomedical Engineering*, vol. 10, no. 3, pp. 171–184, 2010.

[6] B. Asgharzadeh, M. Kohan, and A. Ganji, "Python scripting in abaqus for custom parametric analysis in biomechanics," *Journal of Engineering Science and Technology*, vol. 14, pp. 328–335, 2019.

[7] J. P. v. d. Bergh, P. Szulc, A. M. Cheung, M. Bouxsein, K. Engelke, and R. Chapurlat, "The clinical application of high-resolution peripheral computed tomography (hr-pqct) in adults: State of the art and future directions," *Osteoporosis International*, vol. 32, no. 8, pp. 1465–1485, 2021.

[8] G. C. Bernardi, F. Picchetta, and P. L. Nai Fovino, "Studio biomeccanico della anatomia funzionale della articolazione coxo-femorale," *Clinica Ortopedica "G. Gaslini" dellâUniversitÃ di Genova, Acta*, no. 9, 1963, articolo 23.

[9] D. J. Berndt and J. Clifford, "Using dynamic time warping to find patterns in time series," *KDD Workshop*, pp. 359–370, 1994.

[10] S. Beucher, "Watershed, hierarchical segmentation and waterfall algorithm," *Mathematical Morphology and Its Applications to Image Processing*, vol. 2, pp. 69–76, 1994.

[11] B. Borah, T. Dufresne, and P. Chmielewski, "Evaluation of imaging techniques for the assessment of bone quality," *Journal of Bone and Mineral Research*, vol. 16, no. 10, pp. 1955–1962, 2001.

[12] C. Bosco, N. Rufai, V. Rochira, and L. Gennari, "Technological advancements in bone densitometry and their clinical implications in the management of osteoporosis," *Journal of Endocrinological Investigation*, vol. 43, pp. 605–614, 2020.

[13] M. Boudissa, J. Koueik, S. Ruatti, and F. H. Dujardin, "Application of 3d modeling and printing in preoperative planning for complex fractures: A review of the literature," *Orthopaedics and Traumatology: Surgery and Research*, vol. 106, no. 5, pp. 833–841, 2020.

[14] S. Boutroy, M. L. Bouxsein, F. Munoz, and P. D. Delmas, "In vivo assessment of trabecular bone microarchitecture by high-resolution peripheral quantitative computed tomography," *Journal of Clinical Endocrinology Metabolism*, vol. 90, no. 11, pp. 4998–5005, 2005.

[15] M. L. Bouxsein, "Bone quality: where do we go from here?" *Osteoporosis International*, vol. 14, no. Suppl 5, pp. S19–S24, 2003.

[16] M. L. Brandi, "Microarchitecture, the key to bone quality," *Rheumatology*, vol. 48, no. Suppl 4, pp. iv3–iv8, October 2009.

[17] A. D. Brett and J. K. Brown, "Quantitative computed tomography and opportunistic bone density screening by dual use of computed tomography scans," *Journal of Orthopaedic Translation*, vol. 3, no. 4, pp. 178–184, 2015.

[18] M. Brown, A. DiGioia, and N. Piuzzi, "Optimizing patient-specific finite element modeling of bones: Ct and mri registration," *Clinical Orthopaedics and Related Research*, vol. 472, pp. 2483–2491, 2014.

[19] T. Bulow, A. Schlafer, C. Spies, and U. Schumacher, "Semi-automatic 3d segmentation of bone ct data using region growing algorithms," *Journal of Digital Imaging*, vol. 23, no. 5, pp. 575–585, 2010.

[20] T. A. Burgers, B. O. Williams, A. G. Schwartz, and S. A. Goldstein, "Genetic regulation of bone morphology and remodeling in response to mechanical loading," *Bone*, vol. 48, no. 5, pp. 1005–1015, 2011.

[21] M. V. Caruso *et al.*, "Radiomic texture analysis of trabecular bone structure in osteoporotic patients," *Clinical Oral Implants Research*, vol. 32, no. 12, pp. 1336–1345, 2021.

[22] C.-C. Chang and C.-J. Lin, *LIBSVM: a library for support vector machines*, 2001, software available at: http://www.csie.ntu.edu.tw/ cjlin/libsvm.

[23] G. Chang, S. Boone, D. Martel, C. S. Rajapakse, R. S. Hallyburton, M. Valko, S. Honig, and R. R. Regatte, "Mri assessment of bone structure and microarchitecture," *Journal of Magnetic Resonance Imaging*, vol. 46, no. 2, pp. 323–337, 2017.

[24] D. Chapelle and K.-J. Bathe, "The finite element analysis of shells - fundamentals," *Springer*, 2003.

[25] S. C. Chapra and R. P. Canale, *Numerical Methods for Engineers*, 6th ed. McGraw-Hill Education, 2010.

[26] Y.-C. Chen *et al.*, "Deep learning for medical image analysis: Challenges and the future," *Journal of Medical Imaging*, vol. 4, no. 1, p. 031013, 2017.

[27] P. L. Choyke and B. J. Wood, "Artificial intelligence in medical imaging: From promise to practice," *American Journal of Roentgenology*, vol. 212, no. 4, pp. 741–743, 2019.

[28] A. Completo, J. A. Simões, and F. Fonseca, "Can medio-lateral baseplate position and load sharing induce asymptomatic local bone resorption of the proximal tibia? a finite element study," *Journal of Biomechanics*, vol. 40, pp. 2826–2832, 2007.

[29] J. Compston, "Bone quality: What is it and how is it measured?" *Arquivos Brasileiros de Endocrinologia E Metabologia*, vol. 50, no. 4, pp. 579–585, 2006.

[30] B. Cortet and E. e. a. Dennison, "Radiofrequency echographic multi spectrometry (rems) for the diagnosis of osteoporosis in a european multicenter clinical context," *Bone*, no. 143, p. 115786, February 2021.

[31] S. C. Cowin, "Bone mechanics handbook," *CRC Press*, vol. 2, 2001, second Edition.

[32] S. Cowin and S. Doty, *Tissue Mechanics*. New York, NY: Springer, 2001.

[33] S. C. Cowin, "Bone mechanics," *CRC Press*, 1989.

[34] S. R. Cummings and L. J. Melton, "Epidemiology and outcomes of osteoporotic fractures," *The Lancet*, vol. 359, no. 9319, pp. 1761–1767, 2002.

[35] J. Currey, *The mechanical adaptations of bones*. Princeton University Press, 1999.

[36] P. D. Delmas, "Assessment of bone turnover," *Osteoporosis International*, vol. 19, no. 2, pp. 1453–1456, 2008.

[37] D. W. Dempster *et al.*, "Standardized nomenclature, symbols, and units for bone histomorphometry: a 2012 update of the report of the asbmr histomorphometry nomenclature committee," *Journal of Bone and Mineral Research*, vol. 28, no. 1, pp. 2–17, 2013.

[38] I. Despotovic, B. Goossens, and W. Philips, "Mri segmentation of the human brain: Challenges, methods, and applications," *IEEE Reviews in Biomedical Engineering*, vol. 8, pp. 44–60, 2015.

[39] X. N. Dong and X. E. Guo, "The dependence of transversely isotropic elasticity of human femoral cortical bone on porosity and ash content," *Journal of Biomechanics*, vol. 37, no. 8, pp. 1281–1287, 2004.

[40] R. Fernandes, D. C. Moura, and A. Cunha, "Medical image segmentation using machine learning methods: A bibliographic review," *Journal of Digital Imaging*, vol. 31, no. 3, pp. 307–314, 2018.

[41] D. R. Fisher and F. H. Fahey, "Appropriate use of effective dose in radiation protection and risk assessment," *Health Physics*, vol. 113, no. 2, pp. 102–109, 2017.

[42] H. Fonseca, D. Moreira-Gonçalves, H.-J. Appell Coriolano, and J. A. Duarte, "Bone quality: The determinants of bone strength and fragility," *Sports Medicine*, vol. 44, no. 1, pp. 37–53, 2014.

[43] L. Frazer, N. Louis, W. Zbijewski, J. Vaishnav, K. Clark, and D. Nicolella, "Super-resolution of clinical ct: Revealing microarchitecture in whole bone clinical ct image data," *Bone*, vol. 185, p. 117115, August 2024, epub 2024 May 11.

[44] J. Fritton, K. McLeod, and C. Rubin, "Mechanobiology of bone remodeling and adaptation," *Current Opinion in Orthopaedics*, vol. 11, pp. 378–383, 2000.

[45] H. M. Frost, "A 2003 update of bone physiology and wolff's law for clinicians," *The Angle Orthodontist*, vol. 74, no. 1, pp. 3–15, 2004.

[46] M. M. Galloway, "Texture analysis using gray level run lengths," *Computer Graphics and Image Processing*, vol. 4, pp. 172–179, 1975.

[47] D. García-Lorenzo, G. Francesca, J. Juan-Albarracín, L. Luque, M. Zuluaga, and A. Alberich-Bayarri, "Review: Image segmentation for medical applications," *Journal of Biomedical Imaging*, pp. 198–205, 2013.

[48] A. Giannoula, S. Dalyot, and A. H. Karantanas, "Enhanced bone segmentation techniques in ct: Comparison of region-growing and advanced edge-detection methods," *Computerized Medical Imaging and Graphics*, vol. 69, pp. 41–49, 2018.

[49] L. Gibson *et al.*, "Biomechanical properties of feline cortical bone in the diaphysis of the femur," *Journal of Biomechanics*, vol. 41, no. 5, pp. 1234–1241, 2008.

[50] R. J. Gillies, P. E. Kinahan, and H. Hricak, "Radiomics: Images are more than pictures, they are data," *Radiology*, vol. 278, no. 2, pp. 563–577, 2016.

[51] P. I. Good, "Permutation, parametric and bootstrap tests of hypotheses," *Springer Series in Statistics*, 2005.

[52] L. Grady, "Random walks for image segmentation," *IEEE Transactions on Pattern Analysis and Machine Intelligence*, vol. 28, no. 11, pp. 1768–1783, 2006.

[53] I. Grosse, M. Binkowski, and W. Meindl, "Application of t-tests in bone morphology studies for evaluating significance in geometric and density differences," *Bone*, vol. 104, pp. 237–245, 2017.

[54] N. S. Haeri, S. Perera, I. Ferreiro, D. Hans, and S. L. Greenspan, "Trabecular bone score in the hip: A new method to examine hip bone microarchitecture–a feasibility study," *Archives of Osteoporosis*, vol. 17, no. 1, p. 126, 2022.

[55] M. Hanna, G. Chang, and M. Kim, "Advanced ct imaging techniques and segmentation of cortical bone: A review," *European Journal of Radiology*, vol. 131, p. 109265, 2020.

[56] R. M. Haralick, K. Shanmugam, and I. Dinstein, "Textural features for image classification," *IEEE Transactions on Systems, Man, and Cybernetics*, vol. SMC-3, no. 6, pp. 610–621, 1973.

[57] T. Heimann and H.-P. Meinzer, "Statistical shape models for 3d medical image segmentation: A review," *IEEE Transactions on Medical Imaging*, vol. 28, no. 9, pp. 1449–1465, 2009.

[58] N. Helen and H. Isaksson, "Ct-based finite element models for prediction of bone strength: Current status and future directions," *Bone*, vol. 102, pp. 67–82, 2017.

[59] R. C. Hibbeler, *Mechanics of Materials*, 9th ed. Pearson, 2012.

[60] A. J. Huang, A. L. Boskey, and E. Donnelly, "The contribution of bone quality to osteoporotic fracture risk," *Current Osteoporosis Reports*, vol. 17, pp. 304–319, 2019.

[61] R. Huiskes and E. Chao, "A survey of finite element analysis in orthopedic biomechanics: the first decade," *Journal of Biomechanics*, vol. 16, pp. 385–409, 1983.

[62] H. B. Hunt and E. Donnelly, "Bone quality assessment techniques: Geometric, compositional, and mechanical characterization from macroscale to nanoscale," *Clinical Reviews in Bone and Mineral Metabolism*, vol. 14, no. 3, pp. 133–149, 2016.

[63] J. D. Hunter, "Matplotlib: A 2d graphics environment," *Computing in Science Engineering*, vol. 9, no. 3, pp. 90–95, 2007.

[64] Y.-W. Jiang, X.-J. Xu, R. Wang, and C.-M. Chen, "Radiomics analysis based on lumbar spine ct to detect osteoporosis," *European Radiology*, vol. 32, no. 11, pp. 8019–8026, November 2022, epub 2022 Apr 30. [Online]. Available: https://doi.org/10.1007/s00330-022-08805-4

[65] Z. Jin, R. Wilcox, and B. Roberts, "Automation in finite element analysis of biomechanics using abaqus scripting," *Biomechanics and Modeling in Mechanobiology*, vol. 15, pp. 1715–1724, 2016.

[66] O. Johnell and J. A. Kanis, "An estimate of the worldwide prevalence and disability associated with osteoporotic fractures," *Osteoporosis International*, vol. 17, no. 12, pp. 1726–1733, 2005.

[67] A. Just, P. Martirosian, A. Naumann, G. Steidle, F. Schick, C. D. Claussen, H.-P. Meinzer, and I. Wolf, "Texture analysis of trabecular bone in the proximal femur: Association with biomechanical strength parameters based on multidetector ct images," *Journal of Computer Assisted Tomography*, vol. 37, no. 6, pp. 1017–1023, 2013.

[68] J. A. Kanis *et al.*, "European guidance for the diagnosis and management of osteoporosis in postmenopausal women," *Osteoporosis International*, vol. 30, no. 1, pp. 3–44, 2019.

[69] J. A. Kanis, A. OdÃ©n, E. V. McCloskey, H. Johansson, D. A. Wahl, and C. Cooper, "A systematic review of hip fracture incidence and probability of fracture worldwide," *Osteoporosis International*, vol. 23, no. 9, pp. 2239–2256, 2013.

[70] T. M. Keaveny, E. F. Morgan, G. L. Niebur, and O. C. Yeh, "Biomechanics of trabecular bone," *Annual Review of Biomedical Engineering*, vol. 3, pp. 307–333, 2001.

[71] J. Keyak, S. Rossi, and K. Jones, "Prediction of femoral fracture load using finite element models: an examination of stress and strain-based failure theories," *Journal of Biomechanics*, vol. 28, no. 4, pp. 491–499, 1995.

[72] M.-G. Kim, J.-S. Suh, and J.-M. Lee, "Bone segmentation algorithm using thresholding based on 3d ct images," *Journal of Digital Imaging*, vol. 22, no. 1, pp. 105–117, 2009.

[73] M. Kleerekoper, "Biomechanics of bone strength in osteoporosis," *Journal of Bone and Mineral Research*, vol. 9, no. 11, pp. 1515–1518, 1994.

[74] D. L. Kopperdahl and T. M. Keaveny, "Yield strain behavior of trabecular bone," *Journal of Biomechanics*, vol. 31, pp. 601–608, 1998.

[75] E. F. Kranioti, A. Bonicelli, and J. G. GarcÃa-Donas, "Bone-mineral density: Clinical significance, methods of quantification and forensic applications," *Research and Reports in Forensic Medical Science*, vol. 9, pp. 9–21, 2019.

[76] A. Krauss *et al.*, "Quantitative assessment of bone quality in osteoporosis: Comparison between dxa and ct-based methodologies," *Journal of Bone and Mineral Research*, vol. 29, no. 3, pp. 582–590, 2014.

[77] R. Krug, A. J. Burghardt, S. Majumdar, and T. M. Link, "High-resolution imaging techniques for the assessment of osteoporosis," *Radiologic Clinics of North America*, vol. 48, no. 3, pp. 601–621, 2010.

[78] V. Kumar, Y. Gu, S. Basu, A. Berglund, S. A. Eschrich, M. B. Schabath, K. J. Forster, H. J. W. L. Aerts, A. Dekker, D. Fenstermacher, R. J. Gillies, R. A. Gatenby, D. Mason, and T. A. Sellers, "Radiomics: the process and the challenges," *Magnetic Resonance Imaging*, vol. 30, no. 9, pp. 1234–1248, 2012.

[79] D. Kurniawan, F. M. Nor, H. Y. Lee, and J. Y. Lim, "Finite element analysis of bone-implant biomechanics: refinement through featuring various osseointegration conditions," *International Journal of Oral and Maxillofacial Surgery*, vol. 41, no. 9, pp. 1090–1096, Sep. 2012, epub 2012 Jan 18.

[80] P. Lambin, E. Rios-Velazquez, R. Leijenaar, S. Carvalho, R. G. P. M. van Stiphout, P. Granton, C. M. L. Zegers, R. Gillies, R. Boellard, A. Dekker, and H. J. W. L. Aerts, "Radiomics: Extracting more information from medical images using advanced feature analysis," *European Journal of Cancer*, vol. 48, no. 4, pp. 441–446, 2012.

[81] S. Lee, C. K. Chung, S. H. Oh, and S. B. Park, "Correlating hounsfield units with bone mineral density in ct: Does it predict osteoporotic vertebrae fractures?" *Clinical Orthopaedics and Related Research*, vol. 471, no. 8, pp. 2948–2955, 2013.

[82] W. Li, H. Zhu, J. Liu, H. Tian, J. Li, and L. Wang, "Characteristics of mri-based vertebral bone quality scores in elderly patients with vertebral fragility fractures," *European Spine Journal*, 2023.

[83] Y. Li, Y. Xu, and J. Wang, "A semi-automatic segmentation method combining level set and region growing for medical image segmentation," *Medical Physics*, vol. 41, no. 5, pp. 5189–5200, 2014.

[84] P. Liacouras, J. Garnes, N. Roman, A. Petrich, and G. Grant, "Design and manufacturing of an implant for complex cranial reconstruction using a novel selective laser melting technique," *Medical Engineering Physics*, vol. 33, pp. 1043–1052, 2011.

[85] Y. M. Lim, K. W. Tho, N. Naik, and S.-m. Ong, "Automatic bone segmentation techniques in ct imaging for orthopaedic applications: A review," *Biocybernetics and Biomedical Engineering*, vol. 35, pp. 1–12, 2015.

[86] G. Litjens, T. Kooi, B. E. Bejnordi, A. A. A. Setio, F. Ciompi, M. Ghafoorian, J. A. van der Laak, B. van Ginneken, and C. I. Sánchez, "A survey on deep learning in medical image analysis," *Medical Image Analysis*, vol. 42, pp. 60–88, 2017.

[87] J. Long, E. Shelhamer, and T. Darrell, "Fully convolutional networks for semantic segmentation," in *Proceedings of the IEEE Conference on Computer Vision and Pattern Recognition*, 2015, pp. 3431–3440.

[88] B. C. Lowekamp, D. T. Chen, L. Ibanez, and D. Blezek, "The design of simpleitk," *Frontiers in Neuroinformatics*, vol. 7, p. 45, 2013.

[89] J. Ma, F. Liu, H. Guo, and X. Ma, "Semi-automatic and automatic segmentation for medical imaging in bone and joint diseases: Overview and future directions," *Bone Research*, vol. 9, p. 12, 2021.

[90] S. Majumdar, D. C. Newitt, A. Mathur, S. Osman, A. Gies, E. Chiu, T. M. Link, and N. E. Lane, "Magnetic resonance imaging of trabecular bone structure in the distal radius: Relationship with x-ray tomographic microscopy and biomechanics," *Bone*, vol. 22, no. 4, pp. 527–536, 1998.

[91] S. Martelli, P. Pivonka, and P. Ebeling, "Femoral head size alters hip contact force and work of fracture in finite element modelling of hip arthroplasty," *Clinical Biomechanics*, vol. 67, pp. 106–113, 2019.

[92] R. B. Martin and D. B. Burr, "A hypothetical mechanism for the stimulation of osteonal remodeling by fatigue damage," *Journal of Biomechanics*, vol. 17, no. 9, pp. 613–620, 1984.

[93] R. Martin, D. Burr, and N. Sharkey, "Skeletal tissue mechanics," *Springer-Verlag*, 1998.

[94] A. McFarlane and T. C. Rohlfing, "Segmentation of medical images with artificial intelligence techniques," *Medical Physics*, vol. 24, pp. 91–104, 1990.

[95] A. Mehnert and P. T. Jackway, "An improved seeded region growing algorithm for 3d image segmentation," *Pattern Recognition Letters*, vol. 30, no. 2, pp. 123–128, 2009.

[96] A. Mehnert and P. Jackway, "A review of semi-automated segmentation techniques in medical imaging," *Journal of Digital Imaging*, vol. 23, no. 5, pp. 650–667, 2010.

[97] C. Messina, D. Albano, S. Gitto, L. Tofanelli, A. Bazzocchi, F. M. Ulivieri, G. Guglielmi, and L. M. Sconfienza, "Body composition with dual energy x-ray absorptiometry: From basics to new tools," *Quantitative Imaging in Medicine and Surgery*, vol. 10, no. 8, pp. 1687–1698, 2020.

[98] F. A. J. Mettler, W. Huda, T. T. Yoshizumi, and M. Mahesh, "Effective doses in radiology and diagnostic nuclear medicine: A catalog," *Radiology*, vol. 248, no. 1, pp. 254–263, 2008.

[99] C. Milgrom, A. Simkin, A. Eldad, M. Nyska, and A. Finestone, "Using boneâs structural properties to assess fracture risk: Comparison between cortical and trabecular bone," *Journal of Bone and Joint Surgery*, vol. 85, pp. 1135–1144, 2003.

[100] F. Milletari, N. Navab, and S.-A. Ahmadi, "V-net: Fully convolutional neural networks for volumetric medical image segmentation," in *Proceedings of the IEEE Conference on 3D Vision (3DV)*, 2016, pp. 565–571.

[101] M. J. Mirzaali, J. Schwiedrzik, U. Wolfram, W. R. Taylor, M. O. Heller, R. Weinkamer, G. N. Duda, and B. M. Willie, "In situ assessment of bone tissue mineral density distribution reveals intrinsic microstructural heterogeneity in trabecular bone," *Bone*, vol. 93, pp. 203–210, 2016.

[102] D. C. Montgomery, E. A. Peck, and G. G. Vining, *Introduction to Linear Regression Analysis*, 5th ed. Wiley, 2012, explanation of linear regression and correlation.

[103] J. Nagler, "Failure mechanics of multi materials laminated systems review analysis-based project," 02 2019, figure adapted from Nagler, 2019.

[104] H. Nie, R. Freund, J. Rauch, and H. Kirchner, "Influence of femoral stem design parameters on mechanical stress shielding: a parametric fea," *Journal of Biomechanical Engineering*, vol. 120, pp. 1–7, 1998.

[105] G. Niebur, M. Feldstein, and H. Yuen, "High-resolution finite element models with tissue strength asymmetry accurately predict failure of trabecular bone," *Journal of Biomechanics*, vol. 33, no. 12, pp. 1575–1583, 2000.

[106] A. O. Okaro, O. Farouk, and A. M. Olugbenga, "The role of patient-specific implants in orthopaedic surgery: A review," *Journal of Orthopaedic Surgery and Research*, vol. 16, p. 461, 2021.

[107] A. M. Parfitt, "Targeted and nontargeted bone remodeling: relationship to basic multicellular unit origination and progression," *Bone*, vol. 30, no. 1, pp. 5–7, 2002.

[108] C. Parmar, P. Grossmann, D. Rietveld, M. M. Rietbergen, P. Lambin, and H. J. W. L. Aerts, "Radiomic machine-learning classifiers for prognostic biomarkers of head and neck cancer," *Frontiers in Oncology*, vol. 5, p. 272, 2015.

[109] J. M. Patsch, A. J. Burghardt, G. Kazakia, and S. Majumdar, "Noninvasive imaging of bone microarchitecture," *Annals of the New York Academy of Sciences*, vol. 1240, pp. 77–87, 2011.

[110] R. Pauwels, R. Jacobs, S. R. Singer, and M. Mupparapu, "Cbct-based bone quality assessment: Are hounsfield units applicable?" *Dento Maxillo Facial Radiology*, vol. 44, p. 20140238, 2015.

[111] K. Pearson, "Note on regression and inheritance in the case of two parents," *Proceedings of the Royal Society of London*, vol. 58, pp. 240–242, 1895.

[112] F. Petitjean and P. Gançarski, "Summarizing a set of time series by averaging: from steiner sequence to compact multiple alignment," *Theoretical Computer Science*, vol. 414, pp. 37–51, 2012.

[113] D. L. Pham, C. Xu, and J. L. Prince, "Current methods in medical image segmentation," *Annual Review of Biomedical Engineering*, vol. 2, pp. 315–337, 2000.

[114] A. Phillips, P. Pankaj, and C. Howie, "Finite element modelling of the pelvis: inclusion of muscular and ligamentous boundary conditions," *Medical Engineering Physics*, vol. 28, pp. 1521–1529, 2016.

[115] W. M. Phillips, J. Millar, X. Wu, and B. P. Halloran, "Semi-automated segmentation of bone from micro-ct images using adaptive thresholding and morphological operations," *Computerized Medical Imaging and Graphics*, vol. 39, pp. 23–30, 2015.

[116] P. J. Pickhardt *et al.*, "Abdominal ct for identifying osteoporosis and fracture risk: The role of bone mineral density assessments using hounsfield units," *Radiology*, vol. 268, no. 2, pp. 457–465, 2013.

[117] P. Pisani, F. Conversano, M. Muratore, G. Adami, M. L. Brandi, C. Caffarelli, E. Casciaro *et al.*, "Fragility score: A rems-based indicator for the prediction of incident fragility fractures at 5 years," *Aging Clinical and Experimental Research*, vol. 35, no. 4, pp. 763–773, 2023.

[118] P. Pisani, M. D. Renna, F. Conversano, E. Casciaro, M. Di Paola, E. Quarta, M. Muratore, and S. Casciaro, "Major osteoporotic fragility fractures: Risk factor updates and societal impact," *World Journal of Orthopedics*, vol. 7, no. 3, pp. 171–181, 2016.

[119] P. Piscitelli, C. Neglia, and G. Guglielmi, "Strategies for early diagnosis and monitoring of bone fragility in osteoporosis: State of the art and perspectives," *Aging Clinical and Experimental Research*, vol. 31, pp. 327–335, 2019.

[120] N. A. Pocock and J. D. Wark, "Bone densitometry and bone quality," *Clinical Biochemist Reviews*, vol. 26, no. 2, pp. 41–51, 2005.

[121] P. Prendergast, "Finite element models in tissue mechanics and orthopaedic implant design," *Clinical Biomechanics*, vol. 12, pp. 343–366, 1997.

[122] M. F. Rachmadi, M. Nishio, and K. Togashi, "Radiomics with statistical image features in texture analysis," *Journal of Digital Imaging*, vol. 33, pp. 803–821, 2020.

[123] S. Rastegar, M. Vaziri, Y. Qasempour, M. R. Akhash, N. Abdalvand, I. Shiri, H. Abdollahi, and H. Zaidi, "Radiomics for classification of bone mineral loss: A machine learning study," *Diagnostic and Interventional Imaging*, vol. 101, no. 9, pp. 599–610, September 2020. [Online]. Available: https://doi.org/10.1016/j.diii.2020.01.008

[124] J. Y. Rho, L. Kuhn Spearing, and P. Zioupos, "Mechanical properties and the hierarchical structure of bone," *Medical Engineering & Physics*, vol. 20, pp. 92–102, 1998.

[125] J. Rho, M. Hobatho, and R. Ashman, "Young's modulus of trabecular and cortical bone material: Ultrasonic and microtensile measurements," *Journal of Biomechanics*, vol. 24, no. 2, pp. 1369–1373, 1997.

[126] O. Ronneberger, P. Fischer, and T. Brox, "U-net: Convolutional networks for biomedical image segmentation," *Medical Image Computing and Computer-Assisted Intervention*, vol. 9351, pp. 234–241, 2015.

[127] S. Salvador and P. Chan, "Fastdtw: Toward accurate dynamic time warping in linear time and space," *Intelligent Data Analysis*, vol. 11, no. 5, pp. 561–580, 2007.

[128] P. Sambrook and C. Cooper, "Osteoporosis," *Lancet*, vol. 367, no. 9527, pp. 2010–2018, 2006.

[129] E. Schileo, F. Taddei, A. Malandrino, L. Cristofolini, and M. Viceconti, "Subject-specific finite element models implementing a maximum stiffness criterion for the optimal selection of the hip implant stem," *Journal of Biomechanics*, vol. 41, pp. 2483–2491, 2008.

[130] E. Schileo, E. Dall'ara, F. Taddei, A. Malandrino, T. Schotkamp, M. Baleani, and M. Viceconti, "An accurate estimation of bone density improves the accuracy of subject-specific finite element models," *Journal of Biomechanics*, vol. 41, no. 11, pp. 2483–2491, Aug 2008, erratum in: J Biomech. 2008 Nov 14;41(15):3294. [Online]. Available: https://doi.org/10.1016/j.jbiomech.2008.05.017

[131] E. Schileo, F. Taddei, A. Malandrino, L. Cristofolini, and M. Viceconti, "Subject-specific finite element models can accurately predict strain levels in long bones," *Journal of Biomechanics*, vol. 41, no. 2, pp. 2483–2491, 2014.

[132] C. H. Scholz, S. C. Cowin, and Y. Yoon, "Comparative analysis of bone structural features using principal component analysis and statistical tests," *Journal of Biomechanics*, vol. 41, no. 6, pp. 1095–1102, 2008.

[133] J. J. Schreiber, P. A. Anderson, H. G. Rosas, A. L. Buchholz, and A. G. Au, "Hounsfield units for assessing bone mineral density and strength: A tool for osteoporosis management," *Journal of Bone and Joint Surgery*, vol. 93, no. 11, pp. 1057–1063, 2011.

[134] J. Schwiedrzik and P. K. Zysset, "Anisotropic tissue elasticity in cortical and trabecular bone: A novel microindentation approach," *Journal of the Mechanical Behavior of Biomedical Materials*, vol. 33, pp. 116–128, 2014.

[135] E. Seeman and P. D. Delmas, "Bone qualityâthe material and structural basis of bone strength and fragility," *New England Journal of Medicine*, vol. 354, no. 21, pp. 2250–2261, 2006.

[136] M. Sensale, T. Vendeuvre, C. Schilling, T. Grupp, M. Rochette, and E. Dall'Ara, "Patient-specific finite element models of posterior pedicle screw fixation: Effect of screw's size and geometry," *Frontiers in Bioengineering and Biotechnology*, vol. 9, p. 643154, Mar 2021. [Online]. Available: https://doi.org/10.3389/fbioe.2021.643154

[137] W. Shao, X. Liu, Z. Feng, L. Liu, S. Liu, and W. Li, "Review: Deep learning in medical image segmentation," *IEEE Access*, vol. 7, pp. 163 953–163 974, 2019.

[138] L. Smith and A. Oshri, "Simulation of complex material behaviors using abaqus: An introduction to the fundamentals," *Engineering Simulation*, vol. 34, pp. 45–52, 2009.

[139] R. Smith, L. Jones, and M. Hansen, "Manual segmentation techniques in radiology: Applications and limitations," *Radiology Research and Practice*, vol. 2019, pp. 1–9, 2019.

[140] E. Soldati, M. Pithioux, J. Vicente, and D. Bendahan, "Trabecular bone microarchitecture: A comparative analysis between high field, ultra high field mri and x-ray micro ct in human anatomical samples," *Bone Reports*, vol. 13, p. 100542, October 2020.

[141] E. Soldati, F. Rossi, J. Vicente, D. Guenoun, M. Pithioux, S. Iotti, E. Malucelli, and D. Bendahan, "Survey of mri usefulness for the clinical assessment of bone microstructure," *International Journal of Molecular Sciences*, vol. 22, no. 5, 2021.

[142] T. Sozen and L. e. a. Ozisik, "An overview and management of osteoporosis," *European Journal of Rheumatology*, vol. 4, no. 1, pp. 46–56, 2017.

[143] R. Sues and A. Cesarone, "Finite element analysis and biomechanics applications of abaqus in orthopedics," *International Journal of Mechanical Sciences*, vol. 53, pp. 1090–1096, 2011.

[144] P. M. SzczypiÅski, M. Strzelecki, and A. Materka, "A review of advanced methods for bone segmentation in ct imaging," *Computerized Medical Imaging and Graphics*, vol. 38, pp. 537–550, 2014.

[145] F. Taddei, S. Martelli, B. Reggiani, L. Cristofolini, and M. Viceconti, "Finite element modeling of bones from ct data: validation and application to osteoporosis," *Computer Methods in Biomechanics and Biomedical Engineering*, vol. 9, pp. 353–361, 2006.

[146] F. Taddei, A. Pancanti, and M. Viceconti, "An improved method for the automatic mapping of computed tomography numbers onto finite element models," *Medical Engineering Physics*, vol. 26, no. 3, pp. 251–261, 2004.

[147] ——, "An improved method for the automatic mapping of computed tomography numbers onto finite element models," *Medical Engineering & Physics*, vol. 26, no. 1, pp. 61–69, 2004.

[148] M. Taylor and P. Prendergast, "Four decades of finite element analysis of orthopaedic devices: where are we now and what are the opportunities?" *Journal of Biomechanics*, vol. 37, pp. 129–150, 2004.

[149] G. Thibault, J. Angulo, and F. Meyer, "Advanced statistical matrices for texture characterization: Application to cell classification," *Pattern Recognition Letters*, vol. 31, pp. 63–71, 2014.

[150] J. W. Tukey, *Exploratory Data Analysis*. Addison-Wesley, 1977.

[151] C. H. Turner and D. B. Burr, "Basic biomechanical measurements of bone: a tutorial," *Bone*, vol. 14, pp. 595–608, 2001.

[152] C. Turner and S. Cowin, "Microstructural considerations in the design of orthotropic materials for bone," *Journal of Biomechanics*, vol. 26, pp. 1–11, 1993.

[153] O. Tymofii *et al.*, "Radiomics in osteoporosis and other bone diseases: A literature review," *European Journal of Radiology*, vol. 140, p. 109750, 2021.

[154] F. M. Ulivieri and L. Rinaudo, "The bone strain index: An innovative dual x-ray absorptiometry bone strength index and its helpfulness in clinical medicine," *Journal of Clinical Medicine Research*, vol. 11, no. 9, 2022. [Online]. Available: https://doi.org/10.3390/jcm11092284

[155] J. J. M. van Griethuysen, A. Fedorov, C. Parmar, A. Hosny, N. Aucoin, V. Narayan, R. G. H. Beets-Tan, J.-C. Fillion-Robin, S. Pieper, and H. J. W. L. Aerts, "Computational radiomics system to decode the radiographic phenotype," *Cancer Research*, vol. 77, no. 21, pp. e104–e107, 2017.

[156] van Griethuysen et al., "Computational radiomics system to decode the radiographic phenotype," *Cancer Research*, vol. 77, no. 21, pp. e104–e107, 2017.

[157] B. Van Rietbergen and K. Ito, "A survey of micro-finite element analysis for clinical assessment of bone strength: The first decade," *Clinical Biomechanics*, vol. 26, no. 4, pp. 327–339, 2011.

[158] B. A. Varghese, S. Cen, and D. H. Hwang, "Statistical analysis of radiomic features and geometric shape factors in predicting mechanical properties of bones," *Journal of Medical Imaging*, vol. 2, no. 4, p. 041001, 2015.

[159] A. I. Veress, J. L. McCrory, and V. H. Frankel, "An orthotropic transversely isotropic model for long bones," *Journal of Biomechanics*, vol. 31, no. 7, pp. 563–568, 1998.

[160] M. Viceconti, L. Grassi, and F. Taddei, "Large scale finite element analysis for subject-specific musculoskeletal models," *Clinical Biomechanics*, vol. 16, no. 8, pp. 705–710, 2001.

[161] M. Viceconti and S. Olsen, "Three-dimensional finite element model of a human femur," *Journal of Biomechanics*, vol. 36, no. 4, pp. 527–536, 2003.

[162] M. Viceconti, S. Olsen, L. Nolte, and K. Burton, "Extracting clinically relevant data from finite element simulations," *Clinical Biomechanics*, vol. 20, no. 5, pp. 451–454, 2005.

[163] E. Villamor, C. Monserrat, L. Del RÃo, J. Romero-MartÃn, and M. RupÃ©rez, "Prediction of osteoporotic hip fracture in postmenopausal women through patient-specific fe analyses and machine learning," *Comput Methods Programs Biomed*, vol. 193, p. 105484, Sep 2020, epub 2020 Apr 3. [Online]. Available: https://doi.org/10.1016/j.cmpb.2020.105484

[164] L. Vincent and P. Soille, "Watersheds in digital spaces: An efficient algorithm based on immersion simulations," *IEEE Transactions on Pattern Analysis and Machine Intelligence*, vol. 13, no. 6, pp. 583–598, 1991.

[165] X. Wang *et al.*, "Radiomics and biomechanics: Exploring the synergy in medical imaging for bone analysis," *Biomedical Engineering Letters*, vol. 10, no. 2, pp. 267–275, 2020.

[166] K. M. Williams, A. Darukhanavala, R. Hicks, and A. Kelly, "An update on methods for assessing bone quality and health in cystic fibrosis," *Journal of Clinical & Translational Endocrinology*, no. 27, p. 100281, March 2022.

[167] D. C. Wirtz, N. Schiffers, T. Pandorf, K. Radermacher, D. Weichert, and R. Forst, "Critical evaluation of known bone material properties to realize anisotropic fe-simulation of the proximal femur," *Journal of Biomechanics*, vol. 33, no. 10, pp. 1325–1330, 2000.

[168] T.-J. Yoo, A. Amini, and Y. H. Jin, "Enhancing bone segmentation in ct scans using morphological operations and intensity thresholds," *Biomedical Engineering Letters*, vol. 4, pp. 217–225, 2012.

[169] Y. Yoon, S. C. Cowin, and L. Cardoso, "The bone structural model: A new method to estimate elastic anisotropy," *Biomechanics and Modeling in Mechanobiology*, vol. 7, no. 1, pp. 43–53, 2008.

[170] S. e. a. Zhang, "A review of semi-automatic image segmentation methods in medical applications," *Pattern Recognition Letters*, vol. 72, pp. 1–10, 2016.

[171] Y. Zhang, C. Li, J. Bao, T. Wang, and X. Zhou, "Semi-automatic segmentation for generating finite element models of bones: A comprehensive review," *Computer Methods in Biomechanics and Biomedical Engineering*, vol. 20, no. 10, pp. 1018–1033, 2017.

[172] B. Zhao, L. O. Hall, D. B. Goldgof, and W. A. Tome, "Improving radiomics feature reproducibility and prediction performance using feature robustness analysis and feature selection," *Computers in Biology and Medicine*, vol. 78, pp. 1–10, 2016.

[173] O. Zienkiewicz and R. L. Taylor, *The Finite Element Method for Solid and Structural Mechanics*, 6th ed.   Butterworth-Heinemann, 2005.

[174] A. Zwanenburg, M. Vallières, M. Abdalah, H. J. W. L. Aerts, V. Andrearczyk, A. Apte, S. Ashrafinia, S. Bakas, R. Beukinga, R. Boellaard, M. Bogowicz, L. Boldrini, I. Buvat, G. Cook, C. Davatzikos, A. Depeursinge, I. El Naqa, A. Fedorov, V. Goh, M. Gönen, F. Isensee, D. Jarnet, S. Kerns, K. Kiełczewski, J. Kim, A. Kotrotsou, R. Larue, R. T. H. Leijenaar, M. Liptrot, A.-K. Losnegard, P. Mahadevan, O. Morin, T. Nickson, J. OâConnor, J. Peerlings, S. F. Petit, G. Price, B. S. Rosenstein, J. Sands, D. Sarrut, M. Schöffel, M. Shafiq-ul Hassan, M. Sigovan, J. Socarras Fernandez, S. Tanadini-Lang, D. Thorwarth, E. G. C. Troost, T. Upadhaya, V. Valentini, J. D. P. van Dijk, J. J. M. van Griethuysen, J. E. Villanueva-Meyer, M. Völker, and H. Wang, "The image biomarker standardisation initiative: Standardised quantitative radiomics for high-throughput image-based phenotyping," *Radiology*, vol. 295, no. 2, pp. 328–338, 2020.

[175] P. K. Zysset and A. Curnier, "An orthotropic transversely isotropic model for the elasticity of cortical and trabecular bone," *Journal of Biomechanics*, vol. 27, no. 1, pp. 97–111, 1994.